

**DISEÑO Y CONSTRUCCIÓN DE  
POTABILIZADOR INTEGRAL SOLAR  
DE AGUA PARA COMUNIDADES  
RURALES**

**TESIS**

QUE PARA OBTENER EL GRADO  
ACADÉMICO DE

**DOCTOR EN CIENCIA Y TECNOLOGÍA  
EN LA ESPECIALIDAD DE  
MECATRÓNICA Y DISEÑO MECÁNICO**

PRESENTA:  
**M.C. PEDRO REYNALDO MARTÍNEZ MANUEL**

DIRECTOR:  
**DR. CARLOS ANTONIO PINEDA ARELLANO**

AGUASCALIENTES, AGS, A NOVIEMBRE, 2022.

## ABSTRACT

---

In Mexico and the entire world, there is still a high percentage of people who do not have access to drinking water, so the population, due to the lack of hydraulic networks, consumes water directly from immediate water resources, especially in rural communities. On the other hand, some of the conventional technologies used for the disinfection of non-potable water include ozonation, chlorination, etc. These technologies require sophisticated equipment and specialized operators. In this context, in recent decades water treatment with photocatalytic processes has been thriving in the scientific field, achieving to inhibit bacteria, pesticides, etc. with the feature of using renewable energy. In this project, the design and construction of an autonomous water potabilizer that only uses solar energy as an energy source were developed. Relying on engineering areas such as mechanics, mechatronics, and optics as the main areas for its development. In this context, the autonomy was performed through the assembly of an automated control stage for the whole system powered by photovoltaic modules and operating; reverse osmosis, photocatalytic reactor, sensing devices, and surface water pumps, among others.

In addition, during the reactor construction, a method for the CPC collectors manufacture is proposed, which includes the utilization of a 3D printed mold based on a structural styrofoam molding. This method improves the collector shape properties causing less damage on the aluminum sheet collector surface reducing thus the number of deformations produced by its machining processes.

Keywords: Arduino, Automated potabilizer, CPC manufacturing, 3D printed mold, Ray-tracing analysis, Photocatalytic reactor.

## ACKNOWLEDGMENTS

---

I would like to acknowledge to the Consejo Nacional de Ciencia y Tecnología (CONACYT) for the financial support to the project APN 2015-01-1651 “Diseño y construcción de potabilizador integral solar de agua para comunidades rurales” and for the scholarship granted to fulfill this doctoral project, grant number 299968. Also, thanks to CONACYT project No. 317264 called “Mantenimiento preventivo a equipamiento especializado del Laboratorio de Química Solar del Grupo de Investigación e Ingeniería en Energía Solar” and the Instituto para el Desarrollo de la Sociedad del Conocimiento para el Estado de Aguascalientes (IDSCEA) for the financing received through Project 012-FEIT-2022 of the Technological Innovation Fund 2022.

Besides, I am very grateful to my thesis advisor Dr. Carlos Pineda Arellano who did a great job as an advisor but also as a friend, giving me the chance and motivation to work hand by hand on this project, for relay on me and for helping me on my pathway. Moreover, I thank to my project committee: Dr. Fernando Martell Chavez, Dr. Iván Salgado Tránsito, and Dr. Manuel I. Peña Cruz, for advising me in every step and guiding me through this project with ideas and feeding back, it was helpful to my professional growth. Without them, this project would not be possible. Special thanks to Dr. Gonzalo Carrillo and Dr. Luis Coronado for helping me in every stage of the paper submitted in this project. Besides, I am thankful to Dr. Arturo Díaz for advising me and helping me on the last part of the project.

I would also like to express my gratitude to the CIO staff who support me more than enough to reach the tasks and goals of the project Lupita Ibarra, Gustavo Acevedo, Juan Sarabia, Eduardo Licurgo and Dr. Sergio, I appreciate their assistance and friendship.

Thanks to all my friends and colleagues as well, who were very constructive full of knowledge and wisdom making the process so enjoyable during my staying at CIO. I want to thank them because they gave me more than enough support to complete this project; Omar Claudio, Daniel Berrones, Daniel Sanchez, Filemón Arenas, Cristian and all my schoolmates and undergraduate students who support me whether a long or short time, was unique and priceless.

Furthermore, I want to express all my thankfulness and love to my family, they show me that no matter what happens they are on my side. To my parents Pedro Martínez and Elodia Manuel who encouraged me and gave me the strength to keep on going, they always give me extra support and trust me when I needed it. To my brothers, Leopoldo Martínez (I am so proud of you) and Rodolfo Martínez who are an important part of me they push me up and advise me when I was uncertain, you know I love you and always be very grateful to you. And I am so thankful to my wife Virginia Salazar and our girls: Brida Martínez, Valeria Martínez, Sofia Martínez, and Regina Martínez thanks a lot for being my whole world and motivation when I was down, for being my support and inspiration to go further every day of my life, all I have ever wanted is to be a good example for them.

# NOMENCLATURE

---

<b>ACRONYM</b>	
AOP	Advanced Oxidation Processes
BOD <sub>5</sub>	Biochemical Oxygen Demand at five days
CAD	Computer Assisted Design
COD	Chemical Oxygen Demand
CCP	Parabolic trough concentrator
CPC	Compound Parabolic Collector
CR	Concentration Ratio
DO	Dissolved Oxygen
FC	Fecal Coliforms
HMI	Human-Machine Interface
MAE	Mean Absolute Error
MED	Multiple-Effect Distillation
MF	Microfiltration
MPN	Most Probable Number
MSF	Multi-Stage Flash
NF	Nanofiltration
PMMA	Polymethylmethacrylate
PTSC	Parabolic Trough Solar Collector
PV	Photovoltaic
RMSE	Root Mean Square Standard Error
RO	Reverse Osmosis
ROSA	Reverse Osmosis System Analysis
TSS	Total Suspended Solids
UF	Ultrafiltration
UV	Ultraviolet
WHO	World Health Organization

---

<b>VARIABLE</b>	
A	Total system collector area, m <sup>2</sup>
$A_c$	Grid cell area, m <sup>2</sup>
$A_r$	Reactor area, m <sup>2</sup>
$B_c$	Battery capacity, Ah
$B_{cavg}$	Daily battery capacity average, Ah/day
$D_H$	Hydraulic diameter, m

---

---

$D_L$	Discharge limit
$E_T$	Total energy per day, kWh/day
$E_{UV,n}$	accumulated energy per reactor volume unit, kJ/L
$FRU_L$	Thermal loss coefficient
$F_e$	Efficiency factor
$F_s$	Safety factor
$G_I$	Incident solar irradiance normal to the collector plane, $Wm^{-2}$
$h$	Planck constant, $6.62607015 \times 10^{-34} m^2 kg / s$
$mP$	Module power, W
$N_{i,j}$	Number of photons intersecting the grid
$N_B$	Number of batteries
$N_m$	Number of modules
$P_{ph}$	Power carried by each photon, J/s
$Q_{UV}$	The energy required per unit volume of the solar reactor, kJ/L
$Re$	Number of Reynolds
$T_i$	The solar field inlet temperature of the working fluid, °C
$T_s$	Operation time, s
$T_\infty$	Dry bulb temperature, °C
$\overline{UV_{G,n}}$	average effective incident radiation, $W/m^2$
$V_o$	The output voltage, V
$V_t$	Annual volume, V
$\varphi$	Rim angle, °
$\lambda$	The wavelength of radiation, nm
$u$	Flux velocity, m/s
$\rho$	Water density, 997 $kg/m^3$
$\mu$	Viscosity, $10^{-3} Pa \cdot s$
$\kappa_{\tau\alpha}(\theta_b)$	Modifier at AM 1.5
$\theta_a$	Half acceptance angle, °
$\eta_{opt} \cdot FR\tau\alpha$	Optical Gain
$Q_u$	Solar field useful gain, kW
$\dot{Q}$	Total incident power on the surface $W/m^2$
$\Phi_{i,j}$	Radiative incident flux, $W/m^2$
$\bar{\Phi}$	Average radiative incident flux, $W/m^2$

---

# INDEX

---

Abstract .....	II
Acknowledgements .....	III
Nomenclature .....	V
Index .....	VII
List of Figures .....	IX
List of tables .....	XII
Annexes .....	XIII
1. CHAPTER I: Introduction .....	1
1.1. Background .....	1
1.2. Justification .....	4
1.3. General objective .....	4
1.3.1. Specific objectives .....	5
1.4. Hypothesis .....	5
2. CHAPTER II: Theoretical Framework .....	7
2.1. Water treatment .....	7
2.1.1. Reverse osmosis .....	7
2.1.2. Photovoltaic (PV) system.....	10
2.1.3. Effect of solar energy on water .....	12
2.1.4. Solar CPC photoreactor.....	15
2.1.5. CPC manufacture and evaluation .....	18
2.1.6. Water quality measurement.....	19
2.1.7. Reactor design.....	21
2.1.8. Solar water treatment reactors.....	21
2.1.9. Reactors in Market.....	25
3. CHAPTER 3: Methodology .....	27
3.1. Approach.....	27
3.2. Integral solar water potabilizer: design and estimation.....	29
3.2.1. Desalination stage .....	29
3.2.2. PV solar energy stage .....	32
3.2.3. Photoreactor design.....	33
3.2.3.1. Photoreactor sizing .....	33

3.2.3.2. Photoreactor pump.....	35
3.2.4. CPC design and manufacture.....	36
3.2.4.1. CPC fabrication process using a 3D-printed mold.....	37
3.2.4.2. Collectors efficiency assessment .....	40
3.2.5. Control system.....	42
3.2.6. Integral Potabilizer 3D Model design .....	48
3.2.7. Equipment and materials .....	49
4. Chapter IV: Results.....	51
4.1. Water Potabilizer Assembly .....	51
4.1.1. Desalination stage .....	51
4.1.2. Support structure .....	52
4.1.3. Stand-alone PV stage.....	53
4.1.4. Photoreactor .....	55
4.2. CPC collectors .....	55
4.2.1. Photogrammetric evaluation .....	57
4.2.2. Ray trace evaluation .....	59
4.3. Automation and control stage.....	61
4.3.1. Digital control circuit.....	61
4.3.2. Power circuit .....	62
4.3.3. Installation and assessment in an operational environment .....	63
4.4. Water cost prototype evaluation .....	66
Conclusions.....	68
recommendations.....	70
References.....	72



## LIST OF FIGURES

---

Figure 1.- Osmosis and Reverse osmosis operating scheme [10] .....	8
Figure 2.- Scheme showing water flowing through a RO membrane [12] .....	8
Figure 3.- Comparison of nominal Membranes according to their component separation [14].....	9
Figure 4.- Photovoltaic effect representation [16].....	11
Figure 5.- Typical array Stand-alone PV system (left) and PV electric grid (right) [18]..	12
Figure 6.- Water treatment processes comparison and its different target pollutants; UV, Ozone and AOP [21] .....	13
Figure 7.- Scheme of photocatalysis reaction process [25].....	14
Figure 8.- CPC collectors placed in a tubular solar reactor [28] .....	16
Figure 9.- Ideal 1-sun CPC design for a 32.2 mm glass tube diameter .....	18
Figure 10.- Shows photocatalytic reactor designs that are currently being investigated. Left Casalino-Blanco, 2016, center Yu, H, 2016 and right Neal. 2018. ....	23
Figure 11.- Block scheme of the steps followed for the integral water-treatment system fulfillment. ....	28
Figure 12.- Procedure followed to accomplish the water purifier .....	29
Figure 13.- Simulation in ROSA software .....	31
Figure 14.- Supported RO membranes on the aluminum profile structure .....	32
Figure 15.- Illustration for the different water treatment technologies, associating caudal with the COT to neutralize [78].....	36
Figure 16.- 3D Mold AutoCAD design used for the 3D printer.....	37
Figure 17.- 3D-Mold male piece (left) and assembled pieces forming the CPC 3D-Mold. ....	37
Figure 18.- 3D-Mold and aluminum sheet inside the container developed.....	38
Figure 19.- CPC manufacture technique. a) the mold is placed into the steel container, b) the aluminum sheet is situated over the mold, c) styrofoam is poured, d) instantaneously locked and e) the CPC is obtained. ....	39
Figure 20.- Final result of the CPC Collector built with the 3D mold.....	39
Figure 21.- Conventionally manufactured CPCs assembled in a special structure to maintain the collector shape.....	40

Figure 22.- Photogrammetry technique: a) vinyl placed on top of the b) CPC collector and c) a sequence of pictures are taken to process and d) a point cloud is generated. ....	41
Figure 23.- Flux chart of the procedure to treat in AutoCAD the dot pattern obtained and simulate the model generated in a ray-trace software. ....	42
Figure 24.- Control system graphical depiction .....	44
Figure 25.- P&ID traced to indicate the lines and components in the control stage.....	46
Figure 26.- Digital control circuit designed to run the programmed task according to the signals from main and reactor tank level (high and low), CE and DO sensors. ....	47
Figure 27.- Power circuit assembled to operate the high-power equipment controlled by the digital control circuit. ....	48
Figure 28.- Potabilizer 3D model CAD designed showing the altogether stages (front view). ....	49
Figure 29.- Potabilizer 3D model CAD designed (back view), RO stage is marked in the red dashed box. ....	49
Figure 30.- Main components and materials to develop the prototype .....	50
Figure 31.- Desalination system arrange to test its performance .....	51
Figure 32.- Structure base for the solar water potabilizer .....	53
Figure 33.- PV performance displaying the power dependence related to irradiance ....	54
Figure 34.- Stand-alone PV prototype structure to test its performance. Adapted from [74] .....	54
Figure 35.- Stand-alone PV installation on the water potabilizer structure .....	55
Figure 36.- Structure frames on the top of the structure (left side) utilized to mount the collectors .....	55
Figure 37.- CPC collectors mounted on the top of the photoreactor structure.....	56
Figure 38.- Ideal 1-sun collector (red dotted line) and its comparison with the 3D-mold technique (a) and the traditional procedure (b), below their mean error.....	58
Figure 39.- Ray trace simulation environment for all CPC configurations: ideal (right), 3D-molded (center), and manually manufactured (left) CPC. ....	59
Figure 40.- Shows the ideal 1-sun, 3D-Molded, and conventionally manufactured CPC performances for the 4-day seasons; March 21 (Vernal), June 21 (Summer), September 23 (Autumnal) and December 23 (Winter) corresponding to the equinoxes and solstices .....	60

Figure 41.- Programming and trial of the devices for the control system.....61

Figure 42.- Evaluating the Nextion display status in real-time (left) and virtually simulated (right).....62

Figure 43.- Control circuit Scheme for the testing and probes of every digital control device.....62

Figure 44.- Power circuit array for the outdoor cabinet enclosure. ....63

Figure 45.- Control circuit system outdoor cabinets arrangement. ....63

Figure 46.- Control panel installation during the last section assembled on the structure .....64

Figure 47.- Water potabilizer full operation as an evaluation for the whole process.....64

Figure 48.- Electrical conductivity sensor performance during the evaluation of the potabilizer system.....65

Figure 49.- DO, pH and Temperature sensors activity during the evaluation of the potabilizer system.....66

## LIST OF TABLES

---

Table 1.- Water quality parameters measured in México according to the indicators to evaluate.....	3
Table 2.- Comparison of produced water for each desalination process (calculations are based on a plant capacity of 31,822 m <sup>3</sup> /day and a TDS concentration of 37,000 mg/L) [12] .....	9
Table 3.- Most relevant articles and research analyzed during the project referring to Wastewater treatment solar reactor .....	24
Table 4.- Comparison of some photocatalytic reactors available as a purchase option in the market nowadays .....	25
Table 5.- Well water samples from different points in Aguascalientes city were provided by IMTA.....	30
Table 6.- Devices and their power consumption and energy per day demanded.....	32
Table 7.- Design parameters employed for the photoreactor sizing .....	35
Table 8.- Digital control and power circuit devices and materials list and its specifications .....	43
Table 9.- Most relevant quotes in device and materials for the integral water treatment plant construction (in USD).....	50
Table 10.- Inflow and Outflow desalination evaluation .....	52
Table 11.- Commercial bottled water and desalination system comparison. Adapted from [91] .....	52
Table 12.- Most significant structure pieces to build the water potabilizer .....	52
Table 13.- Relative optical gain in Hottel-Whillier-Bliss (equation 22) as a function of the CPC optical efficiency. ....	57
Table 14.- Parameters of the simulated solar water heating system .....	57
Table 15.- Cost evaluation using the methodology proposed by Banat, F. & Jwaied .....	67
Table 16.- Economic evaluation studies of membrane distillation (MD) and water costs for different water treatment factors (capacity, feedwater, source energy).....	67

**ANNEXES**

---

ANNEX A.....81  
ANNEX B.....84  
ANNEX C .....96

# **1. CHAPTER I: INTRODUCTION**

---

The current deficiency of drinking water is worldwide known. In addition to this, the availability of hydraulic systems, state resources, and still communities where access to it is limited, contribute even more to the reduction of opportunities.

All the aforementioned carry hygiene problems, since having no access, the populations use the water found in the vicinity, even untreated water, which leads to diseases produced by pathogens that cause, cholera, diarrhea among other stomach diseases. The most affected in the end are the rural communities located far from the service.

Nowadays there are several processes to treat water, such as chlorination, filtration, reduction, neutralization, osmosis, etc. These techniques help significantly in urbanized places where water is accessible to treatment plants. However, this type of treatment is limited to urbanized localities, while, on the other hand, its processes require trained or specialized personnel when working with the equipment.

In the last decades, the development and research of alternative methods for the decontamination of water have moved into constant growth, coupled with the use of energy sources caring for the environment. Such is the case of advanced oxidation processes (AOP), which use photosensitive semiconductor materials as an active medium for the degradation of bacteria and pollutants mainly in wastewater.

The purpose of this work is to implement a water purification prototype for rural communities that lack basic water purification services. The resource will be extracted directly from wells or dams near these places to be treated.

The water potabilizer will exploit the natural resource of solar energy to perform this process, through the use of solar panels for its electrical supply, in addition to solar radiation usage to eliminate pollutants in water through AOP processes. The equipment is considered autonomous in its operation, so specialized personnel and continuous monitoring are not necessary, since its control and instrumentation system performs the essential tasks to keep operational the water potabilizer during daylight.

## **1.1. BACKGROUND**

Today the global deficit of drinking water is remarkable and the warnings of the end of this resource in later years are increasingly frequent. In 2017, the WHO reported that, worldwide, the lack of access to safe sanitation is a large-scale problem that includes, 4.5 billion, meanwhile 2.1 billion people have no access to water at home. Of this number of people, even there are who do not have an elementary provision of water (844 million). Including 263 million who collect water traveling to fonts far from their homes [1].

Some countries have too slow progress toward basic sanitation, which means that their inhabitants will not reach universal coverage by 2030, which was stipulated within the WHO sustainable development goals [2], which are monitored within the following 2 objectives:

- Achieve universal and equitable access to safe drinking water and at the same time an affordable price.
- Reach services for everyone such as hygiene and sanitation looking for terminate open defecation and attending to people's necessities in vulnerable situations.

Furthermore, of this huge number of people, some (0,6 billion) share a latrine with others and some others (892 million) defecate in the open, most in rural regions. Related to this, open defecation has rapidly grown in sub-Saharan Africa and Oceania [3].

Besides, due to that environment, inadequate hygiene is related to infections such as hepatitis, diarrhea and cholera among others. The drinking water of people is dangerously polluted due to lacking administration of wastewater [4].

An illness related to unclean water is diarrhea, only in 2017, caused by parasitic worms found in unhygienic and infested water a great number of people ( $\approx$ 220 million) required medication.

Reutilization of water, to recover nutrients or energy is becoming the main policy. Options for water sources used for drinking water will continue evolving, increasing reliance on groundwater and alternative sources, including wastewater.

Additionally, in Mexico, water quality evaluation is carried out based on four indicators: Biochemical Oxygen Demand at five days (BOD<sub>5</sub>), Chemical Oxygen Demand (COD), Total Suspended Solids (TSS), and Fecal Coliforms (FC). The BOD<sub>5</sub> (dissolved oxygen)

and the COD are indicators of the amount of organic matter present in water bodies, coming mainly from wastewater discharges of both municipal and non-municipal origin. The BOD indicates the amount of biodegradable organic matter and the COD specifies the total amount from this one. The BOD5 growth affects the decrease of dissolved oxygen (DO) with the consequent impact on the water environment. On the other hand, COD greater values show bodies coming from wastewater discharges [5].

The TSS measures the number of sediment solids, solid and organic matter in suspension and/or colloidal. They have their origin in sewage and soil erosion. Increasing levels of TSS make a body of water lose the ability to sustain life. Hence, these factors allow us to recognize gradients that go from a natural condition to the water that exhibits traces or important contributions of unclean water discharges. Fecal coliforms are a specific class of bacteria that are present in the intestines of warm-blooded organisms (including humans) and are excreted in their feces.

This parameter is used internationally based on the premise that its absence in water is an indicator that other organisms pathogenic to man are also absent. The determination of fecal coliforms is carried out mainly by the Most Probable Number (MPN) method.

These parameters were measured according to scales from table 1, going from excellent, good, acceptable, contaminated and strongly contaminated.

**Table 1.- Water quality parameters measured in México according to the indicators to evaluate.**

Quality Indicator	Excellent	Good	Acceptable	Contaminated	Strongly contaminated
BOD <sub>5</sub> (mg/l)	≤3	>3 & ≤6	>6 & ≤30	>30 & ≤120	>120
COD (mg/l)	≤10	>10 & ≤20	>20 & ≤40	>40 & ≤200	>200
TSS (mg/l)	≤25	>25 & ≤75	>75 & ≤150	>150 & ≤400	>400
FC (MPN/100 ml)	≤100	100<&≤200	200<&≤1,000	1000<&≤10,000	>10 000

It is significant to mention that the water quality monitoring sites are located in areas with high anthropogenic influence.



Thus, in 2017, the Red Nacional de Monitoreo had 5,028 sites, distributed throughout the country where the evaluation shows alarming results, according to CONAGUA the reported water quality in a range from excellent to acceptable was: 89.5% Biochemical Oxygen Demand (BOD), 66.5% Chemical Oxygen Demand (COD), 94% Total Suspended Solids (TSS) and 44.6% Fecal Coliform (FC). This means that FC, for example, goes from contaminated to extremely contaminated in more than 50% of the monitored sites. This clearly means that referring to FC, the water treatment in México is very critical [5].

## **1.2. JUSTIFICATION**

In some rural sectors of the Aguascalientes state, water is consumed directly from immediate resources. Being the main ones: surface waters, receiving waters, rivers or shallow wells. Furthermore, the problems of hardness created by the high concentrations of salts and minerals cause that, a large part of the water contained in the tributaries represents an increase in the presence of toxic elements to become unsuitable for human consumption [6]. From these, their main risk factors are highlighted.

- ❖ Superficial
  - They are excessively exploited for agriculture, in addition to being used as containers for solid or liquid waste.
- ❖ Underground
  - The aquifers of Aguascalientes present a high deficit due to the excessive extraction that is carried out.
- ❖ Wells
  - The reduction of the aquifer requires digging to greater and greater depths, which makes water extraction more expensive.
- ❖ Fluorine
  - High fluorosis in the water generates the presence of other toxic elements, for example, arsenic. What's more, fluorosis in bones causes decalcification.

The last factor is being currently investigated in the water of the state of Aguascalientes by David Masuoka [7].

## **1.3. GENERAL OBJECTIVE**

The general objective of this project is to design, build, instrument and start up an autonomous water purification equipment, which only requires solar energy for its due operation, using engineering areas such as mechatronics, electronics, mechanics, chemistry and optics, as the main factors for the development of the system.

### **1.3.1. Specific objectives**

- Design, manufacture and start up the water purification autonomous prototype (which does not require supervision or inline energy supply) made up of a photocatalytic reactor and a stand-alone PV system.
- Improve the CPC collecting irradiance capability, assembled in the photocatalytic reactor of the system.
- Assemble and link up a control stage, running an Arduino-HMI-Power circuit communication capable of interconnecting the sensor system with pumps and valves activation for their adequate automation.

### **1.4. HYPOTHESIS**

The knowledge appliance from areas in technological growth such as mechatronics, mechanical design and clean energies and equipment leaning to sensing devices, control, and automated systems, allow developing a functional water potabilizer prototype powered with solar energy with minimum human oversight. This prototype will be feasible, in the decentralized alternative energies application context in Mexico, contributing in this way to the race against the problem of water resource scarcity in rural communities in the country.



## **2. CHAPTER II: Theoretical Framework**

---

### **2.1. WATER TREATMENT**

In recent decades, the progress in the scientific areas related to water treatment to develop technologies that contribute to providing this resource has been incessant. Conventional methods for water treatment are commonly behaved such as coagulation, flocculation, sedimentation, and filtration, among others (UV, ozonation, etc.), The addition and mixing of mineral salts are required in the coagulation process [8]. These procedures deliver precipitates that enable the agglomeration of floating particles, where sedimentation allows its removal.

UV-C and ozonation methods are associated with maintenance costs, besides installation and electrical equipment. Nonetheless, these technologies are successful inactivating viruses (depending on the type) and many protozoa, including Giardia and Cryptosporidium [9]. On the other hand, chlorination is very effective for many microorganisms, with only 0.08 mg/min/liter, however, chlorine is associated with organic substances forming highly refractory and carcinogenic organochlorine compounds [10].

#### **2.1.1. Reverse osmosis**

Desalination is a process reliable and feasible to obtain potable water. Furthermore, nowadays it has become the water supply main alternative for many developing countries. On the other hand, desalination can be made by evaporation or distillation techniques to mention a few. Reverse osmosis is actually, a widely used method and its configurations have expanded to enhance technologies that contribute to the water treatment realization.

Its physical explanation basis on the natural osmosis process which occurs when 2 solutions with different concentrations of minerals or salts are in contact i.e. by a semipermeable membrane. The latter, allows the solvent but not the solute to flow through it, that is, going from a lower to a higher concentration solution, this phenomenon is caused by a natural pressure (osmotic pressure) Figure 1 (left). Otherwise, by applying an external pressure higher than the osmotic pressure the process can be inverted, in this way it goes from the more to the less concentrated water Figure 1 (right). This method allows for obtaining appropriate quality water.

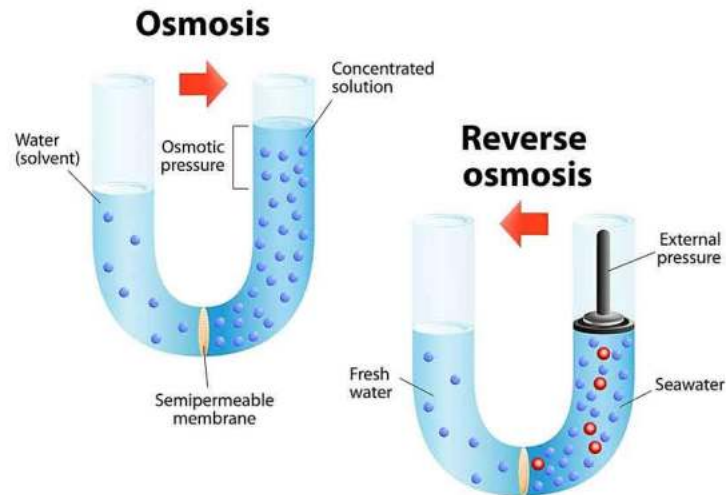


**Figure 1.- Osmosis and Reverse osmosis operating scheme [11]**

This system is a secondary/tertiary stage water treatment. This process consists in pumps that induce reverse osmosis in the semi-treated water flowing to the semipermeable membrane to retire the minerals salts overload. The contaminated water that is unable to pass through the membrane is called reject or concentrate water and this water goes to a drainpipe or can be fed back to the water supply to be recycled through the RO system to retreat the water. The water that passes through the RO membrane is called permeate or product water and generally subtracts ~95 – 99% of the dissolved minerals from it [12]. As shown below in Figure 2.

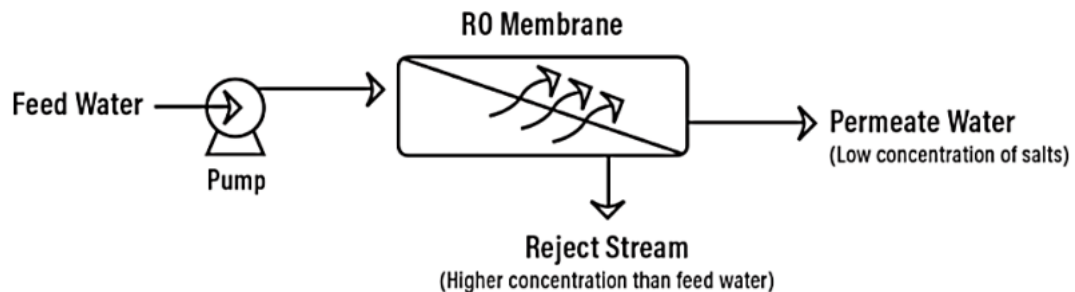


**Figure 2.- Scheme showing water flowing through a RO membrane [13]**

As regards water treatment processes membranes developed, are some types of membranes that include microfiltration (MF), ultrafiltration (UF), and nanofiltration (NF), besides the aforementioned RO membranes (Figure 3). MF has the largest pore size and rejects large particles and various microorganisms. On the other hand, UF membranes have smaller pores than MF and therefore, some bacteria and proteins can be also

eliminated. These membranes remove particles even when having low molar mass (salt ions, organics, etc). The NF membranes are porous ( $\sim 10 \text{ \AA}$  or less) and quite new. They exhibit performance between that RO and UF membranes [14].

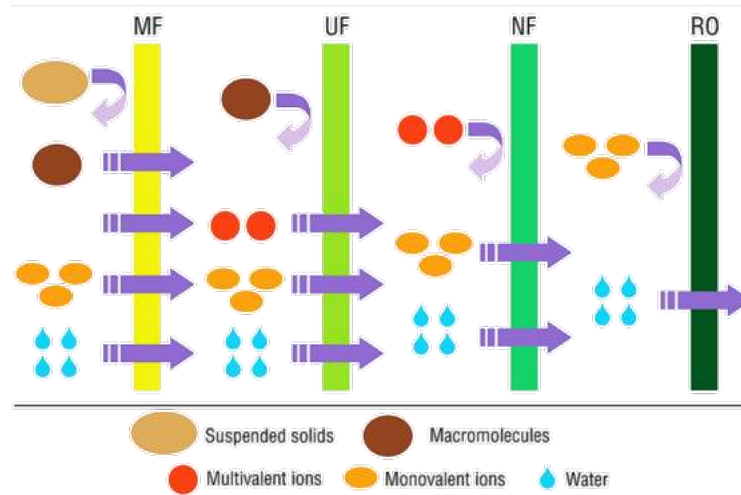


**Figure 3.- Comparison of nominal Membranes according to their component separation [15]**

These membranes are made of synthetic organic polymers. In the case of RO membranes, they are typically arranged in membrane modules and placed in spiral position.

There are some technologies currently used for desalination which can be compared to have a broader overview of this kind of system. In addition to the RO membranes, there are some others like multi-effect distillation or multiple-effect evaporation (MED) and multi-stage flash (MSF). Being MED the oldest technology and the MSF is an improved version of MED.

There are two main aspects to estimating the unit cost; the fixed charges such as rental and electrical power costs. A good criterion to compare these methods is the cost to purify a volume of water for the three technologies. This is shown in table 2, where RO is significantly less than the other two [14].

**Table 2.- Comparison of produced water for each desalination process (calculations are based on a plant capacity of 31,822 m<sup>3</sup>/day and a TDS concentration of 37,000 mg/L) [14]**

Desalination Process	Water Cost (\$/m <sup>3</sup> )
MSF	1.04
MED	0.95

### 2.1.2. Photovoltaic (PV) system

Furthermore, some studies such as Benavides et.al in 2017 [16], use a combination of reverse osmosis supplied with a stand-alone solar electric system consisting of photovoltaic panels. That is some regions (mostly devoid of fresh water) are found isolated from the electrical grid.

Nowadays, renewables energies usage is essential, indispensable, and worthy worldwide. In this sense, solar is an inexhaustible supply of renewable energy which can be transformed and exploited for human benefit. The fields of transformation for solar energy are extensive such as; photochemical, storage, thermal, heating, lighting, and electrical power, among others.

For electrical power, photovoltaic technologies are a revolutionary tool that offers the advantage to generate power supply for electrical needs in systems that demanded it without the needing to connect to the electrical grid (if it's the case). Applications include monitoring, power, pumping (e.g., water pumping), illumination, or storage (battery charging).

The PV devices can convert sunlight (photons) into electrical energy through the use of semiconductor materials (mainly silicon (Si), cadmium sulfide (CdS), gallium arsenide (GaAs), etc.), this process is called the photovoltaic effect and is shown in Figure 4. Since was first utilized in 1954 by the Bell Laboratories, different studies and generations (thin-film, monocrystalline, polycrystalline, etc.) of PV technologies were made. Today these competitive devices have become competitive either in the residential, commercial, or industrial markets in many regions in the world.

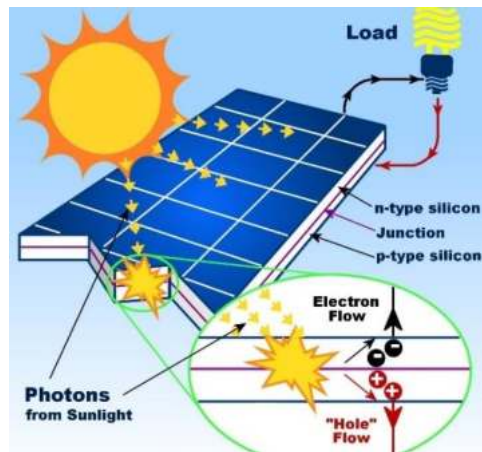


**Figure 4.- Photovoltaic effect representation [17]**

Modules are used in this type of device, these modules contain packed PV cells to produce a voltage/current when irradiated and can be connected in series or in parallel to produce depending on the user to produce a larger voltage/current. Photovoltaic modules are compounds of solar cells, these are commonly made of silicon since this material exists in great abundance on earth, has a low pollution rate, has high durability over time, and has outstanding physicochemical properties. Silicon cells can be classified into three types depending on their manufacturing process: amorphous, mono-crystalline, polycrystalline, and photovoltaic concentration solar cells (CPV). Besides, exist two types of connection for the modules either independently (standalone) or fixed to other electrical power sources (electric grid) as illustrated in Figure 5.

According to Kalogirou [18]; when there is no access to a near source of the electrical grid a useful medium for electrical power in these zones is the stand-alone system which is independent of the electricity grid, producing energy stored normally in a battery bank. This system involves a charge controller, batteries, PV modules and an inverter to transform the DC coming from the PV panels into AC form utilized by most electrical devices. In grid-connected applications, the PV system is connected to the local electricity network. Hence, the power produced by the PV system along the daylight can either be used instantaneously or sold to the electrical company distributor. In the evening, power can be bought back from the network.



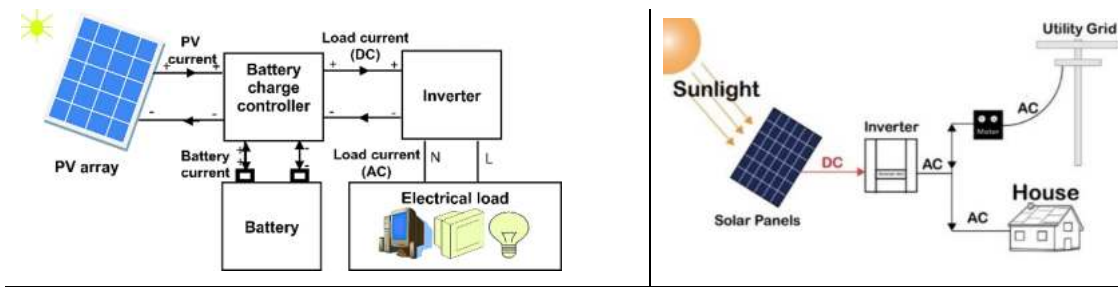
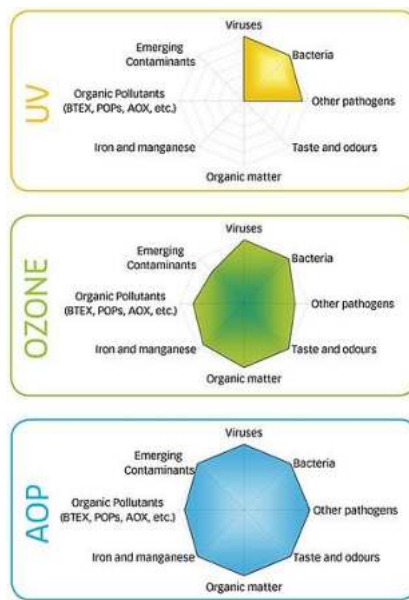


Figure 5.- Typical array Stand-alone PV system (left) and PV electric grid (right) [19]

### 2.1.3. Effect of solar energy on water

Another feasible and effective use of solar energy is by cleaning polluted water, likewise, this utilization is well documented and technologically advanced [20]. The solar radiance contains ultraviolet (UV) light which facilitates the destruction of microorganisms and recalcitrant material. Some of these processes are the so-called solar disinfection (SODIS) and the water treatment based on AOP. The latter is becoming an alternate and unconventional method for pollutant water treatment (Figure 6) due to the high reliance and stability against the complexity of the high chemical concentration levels in water (caused by wastewater textile, pharmaceutical, industrial, etc.). AOPs implicate hydroxyl radicals ( $\text{OH}^\ominus$ ) generation and successive reaction. Diverse oxidation processes, such as  $\text{TiO}_2/\text{UV}$ ,  $\text{H}_2\text{O}_2/\text{UV}$ , Photo-Fenton, ozone and photocatalysis are utilized for these AOPs [21].



**Figure 6.- Water treatment processes comparison and its different target pollutants; UV, Ozone and AOP [22]**

Among these AOP, the ones with the greatest perspective are photo-oxidation existing two variations: photolysis and photocatalysis. Being the latter who's causing an emergent significance in developing effective low-cost disinfection technology, and photocatalytic disinfection is such one [23]. Regarding this, the photocatalytic activity in some materials (photoactive) is the property induced by the irradiation of photons with energy equal to or greater than the energy of the band gap of the material on its surface, this causes the electrons ( $e^-$ ) of the valence band are excited towards the conduction band and consequently generates holes in the valence band. In this way,  $e^- h^+$  pairs are produced, which can later be used to carry out redox reactions [24]. Photocatalysis uses UV radiation as the activation operating principle for water treatment. This process causes the acceleration of a photochemical reaction through the presence of a catalyst ( $Al_2O_3$ ,  $ZnO$ ,  $Fe_2O_3$ ,  $TiO_2$  as the mainly applied), leading to the inactivation of organic matter and heavy metals dissolved in the wastewater. Moreover, there are two types of photocatalytic techniques: heterogeneous (determined by a semiconductor/catalyst), and homogeneous processes where the system is used in a single phase (bone, dissolved catalyst). Photocatalysis is applied when the pollutant itself is not capable of capturing photons, and therefore the use of a catalyst is required that absorbs radiant energy and accelerates oxidation.

Heterogeneous photocatalysis employs the catalyst material, and when exposed to a suitable light source (e.g. solar radiation) can generate reactive species ( $\text{OH}^\bullet$ ) that promote reduction/oxidation (redox) reactions. The titanium dioxide ( $\text{TiO}_2$ ) semiconductor widely used in photocatalysis, is a component chemically and biologically inert, stable to corrosion (chemical and photochemical) and inexpensive [25]. For this reason, it has been used in diverse applications, from sunscreens to intricate devices such as photovoltaic cells, photocatalytic degradation, and biosensors, among others. It is found in three crystalline forms: brookite, anatase, and rutile, the last two being the most effective in wastewater treatment.

The  $\text{TiO}_2$  band gap is  $\sim 3.2 \text{ eV}$  and  $3.0 \text{ eV}$  for the anatase and rutile forms, respectively. To overcome this energy gap and cause photoexcitation (generation of  $e^- - h^+$  pairs) the energy coming from the sun, specifically UV radiation ( $\sim 3 \text{ eV}$ ) has been used. This is the reason why it is required to irradiate with photons from the UV range ( $\lambda \leq 390 \text{ nm}$ ). Photoactivation creates reactive species such as holes in the valence band and electrons in the conduction band. These photogenerated holes conduct to photo-oxidation reaction, while the electrons lead to a photo-reduction reaction as illustrated in Figure 7.

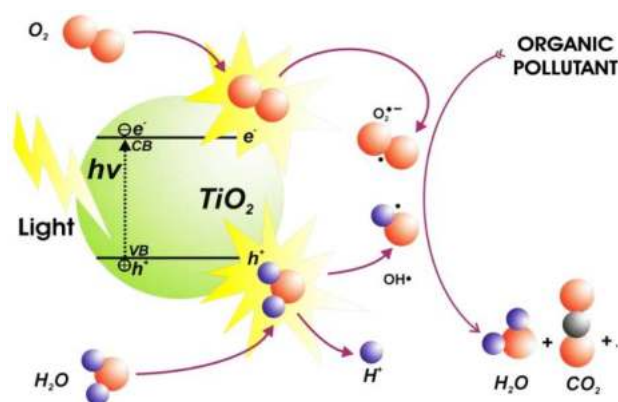


**Figure 7.- Scheme of photocatalysis reaction process [26]**

For the anatase form case, it can be noticed in the equation reaction 1, it is exposed to UV radiation, generating an excess of  $e^-$  in the conduction band and positive holes  $h^+$  in the valence band.



On the surface of the photoactive semiconductor, the holes react both with the absorbed water to be treated ( $H_2O$ ) in equation 2 and with  $OH^-$  groups (equation 3) to form hydroxyl radicals ( $OH^\circ$ ).



On the other hand, excess  $e^-$  in the conduction band react with molecular oxygen to form superoxide radicals (equation 4) and hydrogen peroxide (equation 5).



both superoxide radical and hydrogen peroxide generate more hydroxyl radicals, this is explained using the following reactions (6-8). Where, in the last equation the hydroxyl radical  $OH^\circ$  generated, causing the complete mineralization of many organic substances.



Solar radiation has been used for photocatalysis processes to inactivate microorganisms present in water, as well as the development of experimental systems made to optimize disinfection techniques. Photoreactors, photocatalysis materials and science impacts besides procedures for both gas and aqueous-phase purification and disinfection have increased since then [27].

#### **2.1.4. Solar CPC photoreactor**

Solar photocatalytic processes, unlike solar thermal processes, use high-energy radiation (short wavelength e.g.,  $\lambda \sim UV$ ) to stimulate photochemical reactions. However, the equipment required for solar photochemical applications has much in common with those used for thermal applications. Therefore, parabolic troughs and non-concentrating collectors, representative of conventional solar thermal collector designs, have been used in photochemical systems and reactors.

Water treatment reactors operate a series of studied, analyzed, and probed collectors and arrange which principally are: the flat plate collector, parabolic trough concentrator (CCP), and Compound Parabolic Collector (CPC). The CPC collectors shown in Figure 8, have the advantage over the other designs because they operate the two components of UV radiation (direct and diffuse) and therefore their efficiency can be very high, their production can be much cheaper than concentrating collectors, this fact is due to there's no need for tracking system at low concentrations. Possibly its only disadvantage is its mass transfer flow (turbulent flow is required) [28].



**Figure 8.- CPC collectors placed in a tubular solar reactor [29]**

CPC are non-image concentrators constituted of parabolic reflectors that conduct solar radiation from the aperture to the absorber. They are widely employed in many solar applications [30], among others [31–34], but a particular use is in water decontamination. Two essential design parameters for these collectors are half-angle acceptance ( $\theta_a$ ) and concentration ( $C$ ) both associated by:  $C = 1/\sin\theta_a$ . The concentration is the ratio of aperture to absorber area meanwhile half-angle acceptance is the angle between the edge of the collector parabola and the axis of symmetry. These collectors have the optical characteristic that incident rays on the aperture region within half-angle acceptance will reach the absorber, although the rays within an incidence angle greater than  $\theta_a$  will bounce off the reflecting collector.

A specific and very useful type of CPC performed with fluids is the two-dimensional concentrator with a cylindrical absorber. Widely held geometry is the specific case when  $\theta_a = 90^\circ$ , in this case, the CR = 1 sun [35]; considering an ideal surface, then all the solar

radiation that reaches the aperture is redirected toward the receiver tube. Moreover, these low-concentration collectors are used mainly in water treatment.

Some technological characteristics need to be considered when solar photocatalysis is related to CPC reactors [36].

- ❖ Catalyzer deposition. - catalyzer can be deposited in two ways; diluted in the water or supported (e.g., on the tubes). The advantage of using a supported catalyzer is preventing the separation after the treatment, farther, the reuse of material is viable due to the supported composition.
- ❖ Reactor illumination. - either UV lamps or sunlight the ideal photochemical water treatment configuration for this type of reactor is the tubular (due to the flow control). In this case, the diameter is the most important parameter; applied values are  $\sim 25 - 50 \text{ mm}$ . Higher values suppose non-illuminated volume and lower suppose load loss (pressure drop).
- ❖ Reflecting surface. - The CPC collector is typically fabricated with silver metallic foil-polymer or high-specular reflectivity aluminum sheets [37]. On the other hand, the absorber is produced of transparent glass or copper tubes depending on the application. This element has the role to reflect and redirect all the useful light to the tubes, so, is desirable a material highly reflective, especially in the UV range. Among the most employed metal-coated sheet are: silver (96% reflectance), aluminum (94-96% reflectance), rhodium (78% reflectance) and platinum (68% reflectance), among others. Despite silver has higher reflectance than others, aluminum is almost as high, but with the benefit that is cheaper compared to silver.

The conventional CPC design operates equations 9 and 10 for the concentrator's involute profile and for the parabola equations 11 and 12 are performed on a  $xy$  plane, where  $r$  is the external radius of the receiving tube. Furthermore, the rim angle  $\varphi$  is the angle between the axis and a tangential line coming from the focus to the edge of the collector. Recalling the case where  $\theta_a = 90^\circ$  the involute is plotted in Figure 9 (blue line).

Finally,  $\theta_a$  is the half-angle of acceptance [38,39] considered for the collector design. Figure 9 displays the 2D representation for a CPC of  $CR = 1 \text{ sun}$  for a tube with external  $r = 16.1 \text{ mm}$ , the  $CR$  is specified in equation 13 where an angle of  $90^\circ$  was specified.

$$x = r (\sin \varphi - \varphi \cos \varphi) \quad (9)$$

$$y = -r (\varphi \sin \varphi + \cos \varphi) \text{ with } 0 \leq \varphi \leq \pi/2 + \theta_a \quad (10)$$

$$x_2 = r (\sin \varphi - A \cos \varphi) \quad (11)$$

$$y_2 = -r (A \sin \varphi + \cos \varphi) \quad (12)$$

$$\text{where } A = \frac{\left[ \frac{\pi}{2} + \theta_a + \varphi - \cos(\varphi - \theta_a) \right]}{1 + \sin(\varphi - \theta_a)} \text{ with } \frac{\pi}{2} + \theta_a \leq \varphi \leq \frac{3\pi}{2} - \theta_a$$

$$CR = \frac{1}{\sin \theta_a} \quad (13)$$

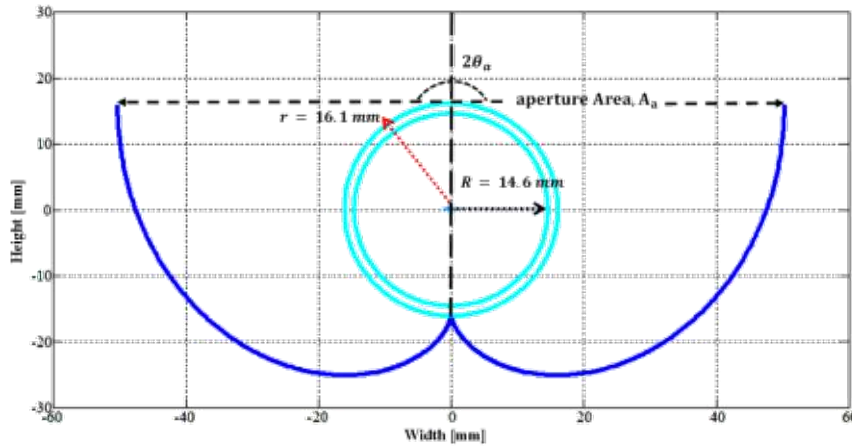


**Figure 9.- Ideal 1-sun CPC design for a 32.2 mm glass tube diameter**

### 2.1.5. CPC manufacture and evaluation

Concerning the collector's fabrication, the main methods used for fabrication are lamination (hydraulic press) and some crafted machining methods. Nonetheless, these processes produce inaccuracies and damage in geometry and to the high-reflectivity film respectively, affecting (optically) the collectors' efficiency.

Studies on thermal efficiency are investigated from the perspective of the support structure, design, and construction [40]. Some others [41], use assemblies that required joints that generate gaps between them. Besides, a study presented by Meiser and collaborators tries to minimize the deviation that occurs from gravity load on mirror shape, examining its deformation, and its effect on the shape of the mirror, where the resulting focus deviation values were evaluated [42,43].

Balghouthi et al. analyzed the performance of a parabolic trough solar collector (PTSC) by photogrammetric techniques referred to [44]. Osório et al. in an attempt to minimize the energy cost proposed a tracking CPC-type solar collector design [45], however, their

results are based on a simulated ideal collector, leaving aside the potential malformations or manufacture bending that may affect their performance. Moreover, in Atul S.Jadhav et al. [46], these bending or malformations phases imply an energy loss of 17% in its performance, having a negative impact directly on the results for their low-cost collectors' method.

In this regard, are some methods to evaluate the collector's profile. Some applying pattern photogrammetry technique [47,48] or reflection deflectometry [49–52]; particularly, Sainath A.Waghmare and Nitin P.Gulhane [53] establish in their study that the spread of reflected rays in the CPC evaluated grew due to manufacturing errors. Others use geometries ideally defined and processed into 3D models to measure the ray-trace flux distribution by simulation software [54,55]. Either one of these methods is effective and validated, remarking that depends on the particular purpose of the object to be evaluated. Carrillo et al. [56] propose a methodology to manufacture 2D cylindrical CPCs collectors recently, by using a Styrofoam mold, obtaining the profile necessary without using mechanical methods. Where to analyze and so identify the technique's efficiency, the manufacturing results were evaluated by a photogrammetric technique.

In this context and awareness of the problem, this technique is described and implemented (in chapter 3), where a proposal for the fabrication of cylindrical CPCs consisted of using a mold made by a 3D printer and styrofoam molding that contributes to the structure. This technique shows the advantage to improve the CPC profile quality achieving decreased deformations and a reduced amount of damage to the high-reflectivity coating. To estimate the effectiveness of this technique, a hybrid experimental simulation assessment was made based on photogrammetric and Ray tracing methods. The test compared the CPC manufactured with the proposed methodology versus one manufactured by conventional machining techniques. The results from this assessment are presented in chapter IV.

#### **2.1.6. Water quality measurement**

Drinking water quality is an essential factor, mainly for human and biodiversity welfare, in this way water indicators and their parameters are key since good quality water defines as well an efficient water treatment system. Monitoring water quality is therefore crucial to



identify potential purification issues and operate effective strategies for the system treatment.

Hence, some indicators impact water quality, consequently, it is required to monitor and assess the treatment process employed to maintain it within the standard parameters required by Mexican regulations. The most important are listed below [57].

- ❖ Dissolved oxygen. - Dissolved oxygen is one of the most important indicators of water quality. Normal values vary between 7.0 and 8.0 mg/L. The main source of oxygen is the air, which is rapidly diffused into the water by turbulence in rivers and by the wind in lakes.
- ❖ pH. - This parameter is expressed on a scale ranging from 0 to 14. Low numbers indicate the degree of acidity in the water; higher numbers how basic water is. A score of 7 is neutral. Normally, the photocatalysis process is more efficient in an acid medium ( $3 \leq pH \leq 5$ ). pH affects the surface properties of the catalyst and the chemical form of the mineral or pollution to be degraded, and this is manifested in changes in the rate of degradation. The normal range of pH in drinking water is about 6.5 - 8.5 pH. So, in this case, reconditioning needs to be done, thus the water is established on the standard ratio required.
- ❖ Conductivity. - It is a property that aqueous solutions possess to conduct electric current. This property depends on the presence, concentration, mobility, valence, and temperature measurement of the ions. This conductivity provides information about the decomposition of organic matter and also contributes to the detection of sources of contamination, the evaluation of the attitude of water for irrigation, and the evaluation of the geochemical nature of the land. Conductivity is reported in units of Siemens/cm (S/cm). Where milliSiemens/cm (mS/cm) or microSiemens/cm ( $\mu$ S/cm) are the most utilized to describe common waters. Deionized and distilled water are, in a range of 0.05  $\mu$ S/cm, seawater is around 50 mS/cm and finally drinking water goes from 200 to 800  $\mu$ S/cm. The reverse osmosis permeate unit varies based on the feed concentration and operating pressure. RO water conductivity should be at the deionized water and drinking water range (0.05  $\mu$ S/cm-200  $\mu$ S/cm) [58].

- ❖ Temperature. - The speed of the photocatalytic reactions does not change appreciably with the variation of the system temperature, even in tests carried out using solar radiation. This behavior is typical of initiated photochemical reactions, by absorption of a photon.

### **2.1.7. Reactor design**

As described, there are main factors when designing a photocatalytic reactor, the catalyst might be set solid, dissolved, or suspended and thus, complicates the entire process of engineering. In this way, is evident that, besides succeeding a reliable contact between the reactants and the catalyst (high catalyst surface area per reactor unit volume), it is also necessary to obtain efficient exposure to the irradiated light (either sun or artificial) for the process, that is the optimal distribution of light inside the reactor.

In addition, other parameters (conventional) must be considered, such as flow distribution, mixing, the interaction between reagents and catalyst, mass transfer, etc., also play a relevant role. For all these reasons, the practical application of any photocatalytic process requires the design of an efficient photoreactor [59].

Nowadays, most of the basic research in photoreactors has been performed in a laboratory scale and this has been where efficiency was not as important as obtaining experimental conditions that allow adequate reproducibility to obtain extensive knowledge about the influence of the different relevant parameters in the process. This is adequate from a scientific point of view, nevertheless is not enough when trying to make a change of scale and thus, be able to put the evidence generated into a practical application.

Another relevant aspect of the photoreactor design is the complexity to compare different photocatalytic reactors with each other which tends to complicate both design and its optimization. This is due, besides the numerous parameters that get involved in the process, to the significant differences presented between different reactors when their scale also varies. Furthermore, the localization when working with solar radiation that is changing continuously and besides is different according to the site, makes it more challenging.

### **2.1.8. Solar water treatment reactors**

Over the last few years, different systems of solar reactors for water treatment based on collectors have been built and assessed. The first successful application of water disinfection using sunlight was published in 1980 [60]. Solar disinfection has proven to be an effective treatment method, which is practical and also has low operational costs.

The first reports of the potential for disinfection through the use of titanium dioxide ( $TiO_2$ ) were made by Matsunaga et al. In 1985 [61]. These authors showed the inactivation of bacteria such as *Lactobacillus acidophilus*, *E. coli*, the yeast *Saccharomyces cerevisiae*, and the alga *Chlorella vulgaris*, after 120 minutes of incubation with  $TiO_2/Pt$  powders. One of the most interesting applications of disinfection by means of solar radiation is known as SODIS and refers particularly to domestic amounts of approximately 1.5 to 2 liters carried out in bottles of polyethylene terephthalate. This technique has been successfully verified in the real field for applications under different projects around the world [25,37,62,63]. Gradually, research on  $TiO_2$  disinfection moved from basic laboratory studies to the first trials with real disinfection applications. In 2000, Herrera Melián et al. reported on the assisted  $TiO_2$  disinfection of urban wastewater [64]. Two microbial groups, total coliforms and *Streptococcus faecalis*, were totally eliminated from water samples, using both UV-C lamp and sunlight. This publication was one of the first to report disinfection applied to water coming from superficial receptor bodies, finding very little difference between photocatalysis with  $TiO_2$  in sunlight or direct UV-C lamp.

A couple of decades ago, only two demonstrations of water treatment/purification using solar radiation at an industrial scale were known, one for groundwater treatment in the United States [65] and another for wastewater treatment in the Solar Platform of Almeria, Spain [66]. Since then various engineering systems have been built and installed, In 2018, Neal and coworkers [67], they have conducted a study, in which  $TiO_2$ -coated quartz optical fibers were coupled to light-emitting diodes (OF/LEDs) to improve the delivery of light in situ. With the use of fiber optic bundles coated with  $TiO_2$ , they achieved to reduce the energy requirements to deliver photons and increase the available surface area, which improved the performance for the elimination of oxidative contaminants. Besides, in 2016 [68] a continuous flow photocatalytic disinfection device was presented with a capacity of  $1 m^3/h$ . The central reactor of the photocatalytic device was structured by installing a  $TiO_2$  coated helical support around a UV lamp in an annular reactor. This

photocatalytic device exhibited superior disinfection ability to UV technology. *Escherichia coli* (*E. coli*) was flowed through the photocatalytic device, and the assessment found that the reactor improve the elimination of the bacteria compared to conventional UV disinfection.

Besides, [69], in 2016 carried out a research project where the disinfection of domestic wastewater for reuse was studied, evaluating the potential of combining a solar photocatalytic process that uses hydrogen peroxide (solar  $UV/H_2O_2$ ) with a horizontal subsurface flow constructed wetland system (HSSF WS), as an alternative for the reuse of domestic wastewater for irrigation. To do this, a photoreactor was built in polymethylmethacrylate (PMMA) tubes exposed to UV solar radiation, and the effect of photolysis and the addition of hydrogen peroxide was evaluated. Their results indicated that it is possible to obtain a degree of disinfection of 99.999% of fecal and total coliforms when advanced oxidation technologies and the biological system are coupled with a retention time of three days in the HSSF WS and five hours in the photoreactor. Figure 10 shows the systems designed and currently under investigation for this type of reactor.

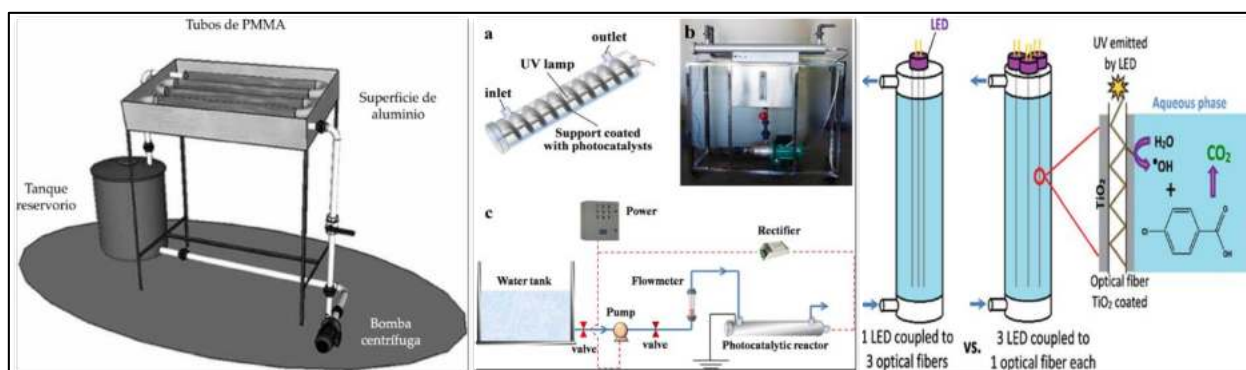


**Figure 10.- Shows photocatalytic reactor designs that are currently being investigated. Left Casalino-Blanco, 2016, center Yu, H, 2016 and right Neal, 2018.**

In recent years, very innovative fabrication techniques have emerged which are noteworthy to mention and that were helpful in the construction and design process of the water treatment system. In this way, the research studies in the area of the photocatalytic reactor have been considered, where stands out Sacco in 2018 [70], using a reactor with low-concentration CPC-type solar collectors, achieves inactivate *E. Coli* from municipal wastewater.

Besides, Terrón et.al, in 2018 demonstrated through ray-tracing simulation the use and comparison of different tube configurations to be arranged in a photocatalytic reactor, where they study the best performance given the possible patterns [71].

Finally, the transcendence papers in the construction of these systems are also the main part of this project, as in Salgado I. et. al in 2015 [38], where they investigate the collectors' manufacture and their arrangement for  $TiO_2$  supported tubes, or Augugliaro in 2005, which demonstrates a hybrid reactor using CPC collectors and membranes [72].

Table 3 shows the most relevant literature sourced for this project.

**Table 3.- Most relevant articles and research analyzed during the project referring to Wastewater treatment solar reactor**

Research article	Contaminant	Solar collector type	Catalyzer	Highlights
Augugliaro et al., 2002	Methyl orange	CPC*	Suspended $TiO_2$	CPC in the solar platform of Almería. complete decontamination Photocatalytic and membrane hybrid reactor
Augugliaro et al., 2005	Lincomicina (antibiotic)	CPC	Suspended $TiO_2$	Reactor híbrido fotocatalítico y de membrana
Rodríguez-Chueca et al., 2014	E. coli	CPC	ferrous sulfate	Complete bacterial inactivation with pH=3 and for pH=5 requires more solar energy to achieve the same results
Malato et al., 2016			Suspended $TiO_2$ particles	Strategies to improve quantum efficiency
Onotri et al., 2017	Copper, Iron, Zinc	CPC	Suspended $TiO_2$	Removal efficiencies of 93.5% (copper), 99.6% (iron), 99.4% (zinc), 97.2% (EDDS), and 80.7% (TOC)
Almomani et al., 2018	Estrogen and antibiotic	CPC	Iron perchlorate $TiO_2$	The efficiencies with ferric ions did not exceed 12.7% and 28.3%, respectively. Adding $H_2O_2$ to iron or $TiO_2$ increased the removal to the 80-96% range.
Mecha et al., 2018	E. Coli and salmonella		Calcined powder $TiO_2$ and ozonation	Wastewater Solar disinfection (SODIS)
Nahim-Granados et al. 2018	E. Coli and salmonella	IPC**	Ferrous sulfate and ferric nitrates	Disinfection even with high turbidity (100 NTU)
Orlandi et al., 2018	Industrial wastewater	PDC***	iron oxide and iron chloride	Rapid reduction of large amounts of surfactants in industrial wastewater.


Sacco et al., 2018	E. Coli	CPC	$TiO_2$ nitrogen-doped	Inactivation of E. Coli in municipal wastewater
Vela et al., 2018	Methylparaben and bisphenol	CPC	$TiO_2$	The use of $TiO_2$ with an electron acceptor strongly improves the degradation rate. Cost 150 € m <sup>-3</sup>
[73]		CPC	$TiO_2$ supported	Try another type of tube configuration.
[74]		CPC	Various agents	Types of CPCs, specific description, construction, future.
Cabrera-Reina et al., 2019	Acids (red and yellow) and reagents (black and orange)	CPC/IPC	Iron	Collectors efficiency comparison.

\*Compound Parabolic Concentrator \*\*Inclined Plane Clarifier \*\*\*Paraboloid Dish Collector

### 2.1.9. Reactors in Market

Concerning to photocatalysis-based water treatment devices, currently, there are some reactors and technologies on the market that are meant to contrast them in terms of production, energy consumption, and price. The intention is to identify and reach a near-competent low-cost/production ratio for this project. Table 4 shows some of the products that are currently on the market and that are qualified for delivering treated water through photocatalytic processes. As seen, these devices use artificial light instead sunlight, which makes this project even more worthwhile and remarkable by exploiting alternate energies such as the sun.

**Table 4.- Comparison of some photocatalytic reactors available as a purchase option in the market nowadays**

System	Frontal view	Company	Production (L)	Energy consumed (kW/h)	Price (MXN)
Photocatalytic and photochemical reactor		Roctec	20	1.2	~120,000.00

<p>Photocatalytic reactor: UV lamp</p>		<p>Anyang Goakang medical co.</p>	<p>50</p>	<p>1</p>	<p>~550,000.00</p>
<p>Photocatalytic reactor: UV lamp</p>		<p>Techinstro</p>	<p>0.1-100</p>		<p>~62,000.00</p>

### 3. CHAPTER 3: Methodology

---

#### 3.1. APPROACH

To perform the water purification system, and thus sketch a monitoring scheme, the steps to manufacture the system right from the beginning were defined. These steps are shown in the block diagram in Figure 11. Which is distributed as follows:

- a) The preliminary prototype design for the water treatment system construction is performed to have established the elements that are part of the equipment. This design has the components referenced with the actual dimensions or approach to the final design.
- b) The desalination system is dimensioned through the water characterization following the quality regulations and the data obtained by the analyzes performed in localized wells in Aguascalientes city. Additionally, the control system for monitoring the conditions of the water treated is implemented in the assembly.
- c) The photovoltaic system is dimensioned according to the electrical equipment that will be used for the control and automation of the water treatment system. With this procedure, we will know the energy consumption that will be had, whilst the system will harness the solar energy source with photovoltaic panels.
- d) The water treatment plant structure will be built using aluminum profile supports, for the optimal setting up equipment.
- e) Once the water quality control and monitoring assessments have been accomplished, the available technology will be integrated, such as pressure, temperature, pH, dissolved oxygen sensing devices, etc. to name a few.
- f) Finally, the system quality will be evaluated so it attends to the optimal standards required for the final features of the treated water, such as; the monitoring system, the photocatalytic reactor, the desalination system, etc.



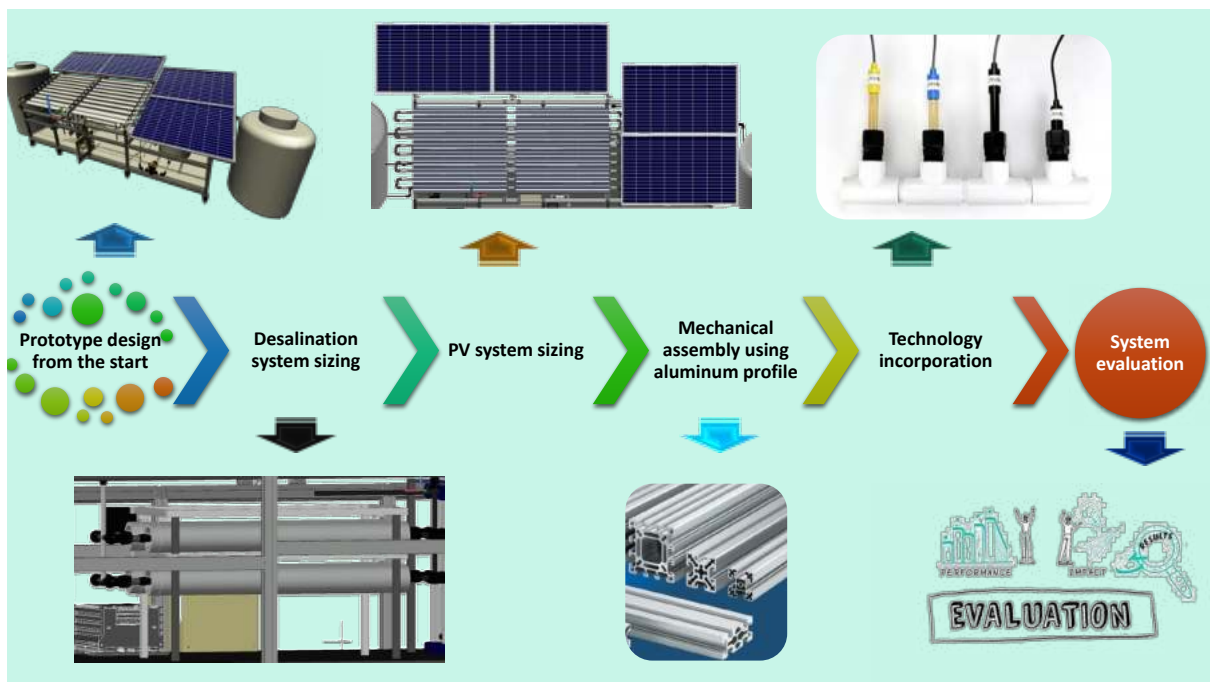


**Figure 11.- Block scheme of the steps followed for the integral water-treatment system fulfillment.**

Once the block scheme system for the water-treatment system construction has been planned, a procedure method is also followed to complete the water purification, therefore a methodology is presented in Figure 12. Where, it is schemed to purify the locality well and/or dam untreated water, which will be previously analyzed and later stream through the water treatment plant. This system incorporates a photovoltaic modules system to energize electrically the system. First, the water sample flows through the desalination stage which consists of reverse osmosis membranes, to remove salts and minerals. It is then circulated through a tubular photoreactor to inhibit recalcitrant microorganisms and chemical species in the water that possibly surpass through the desalination system. The potabilizer includes a control system for the monitoring and automation of the process. Likewise, specific sensors are included for the sensing of the main parameters for drinking water quality and thus establish whether or not the treated water has the required conditions according to these factors. Finally, an optimal and unpolluted product is obtained, where final sampling analyses will be done to guarantee adherence to the established Mexican regulations.



Figure 12.- Procedure followed to accomplish the water purifier

### 3.2. INTEGRAL SOLAR WATER POTABILIZER: DESIGN AND ESTIMATION

Initially, the water potabilizer project starts from sizing and sketching the prototype concept, thus, every stage was scheduled and designed to produce (altogether)  $1\text{ m}^3/\text{day}$ ; desalination, stand-alone PV system, tubular photoreactor (collectors fabrication), and control system. Afterward, a mechanical design was made in a 3D model generator software creating each stage item and system that integrates the prototype. It is mentioned that, since most of the processes were unknown, it was begun from scratch, reviewing the existing sources mentioned in Chapter II. It must be mentioned, that this project was performed using reverse engineering in some stages of its construction.

#### 3.2.1. Desalination stage

The proposal made by Gomez [75] in 2018, has served as the basis to assemble the membrane desalination simultaneously with the use of PV modules for the entire water treatment plant in this project and is after such proposal (extension of it). The aforementioned location parameters are from Aguascalientes and therefore the solar conditions and water to treat are the same for the PV modules and the well water respectively.

For the RO membranes selection, there is specific software that uses some factors from the water to be processed, and setting this data in the software generates a suggestion

of the possible RO types to use. This is the case of ROSA (Reverse Osmosis System Analysis), which is a software (by Dow Chemical™) created to calculate RO at industrial installations grade. ROSA uses variables such as Temperature, pH, flow, and some quality parameters from the water to be treated and as a result of simulation made in the software, delivers physical characteristics of both RO membranes and pressure flow needed. The water quality to be treated it's described in annex A in the final section of annexes. The Water Quality variables were obtained from the analysis performed in the Instituto Mexicano de Tecnologías del Agua (IMTA) laboratory on 3 samples from different locality wells (downtown, northeast, and south). The main significant IMTA water study reveals values above those allowed by the Mexican regulation NOM-SSA1- 127-1994 (Table 5) where fluorine is one of the main critical pollutants in the city, its nominal range in drinking water according to the Mexican Standards should be 0-1.5 mg/l.

**Table 5.- Well water samples from different points in Aguascalientes city were provided by IMTA.**

<b>Zone (Aguascalientes)</b>	<b>Factor</b>	<b>mg/l</b>
<b>Overall</b>	Bicarbonates	495
	Carbonates	<0.188
	Sulfates	779
	Calcium	41.9
	Sodium	455.6
	TDS	1514
<b>Downtown</b>	Fluorine	1.08
<b>Northeast</b>	Fluorine	<b>2.28</b>
<b>South</b>	Fluorine	<b>2.73</b>

In this case, once the simulation is done ROSA delivers the results presented in Figure 13 where a platform software screenshot is shown, and thus using these calculations, membranes RE4040-BLN are selected according to the simulation with no more than 100 PSI pump pressure. The RO membranes highlights and operating limits are:

- Permeate flow rate: 2,500 GPD (9.5 m<sup>3</sup>/day)
- Nominal salt rejection: 99.2%
- Effective membrane area: 7.9 m<sup>2</sup>
- Nominal operating pressure: < 150 psi
- Max. operation flow rate: 68 L/min
- Max. Operating Pressure 600 psi
- Max. Operating Temperature: 45 °C

➤ Operating pH Range 3.0–10.0

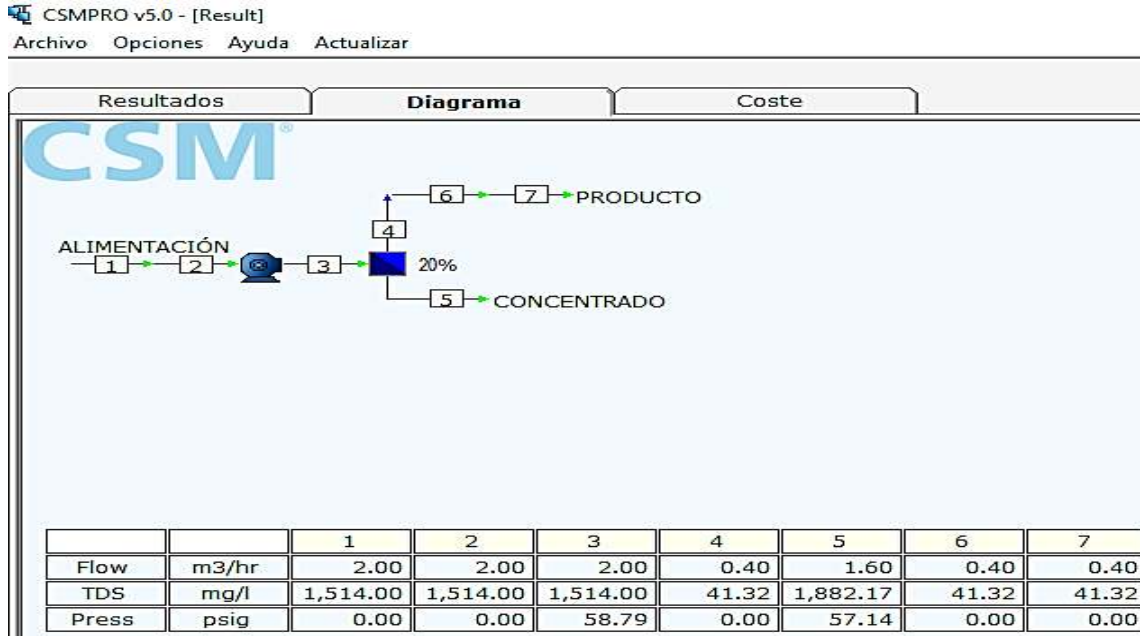


**Figure 13.- Simulation in ROSA software**

In consequence, given the flow and pressure, and analyzing the RO membranes' nominal pressure of <150 psi it is easy to estimate the power of the pump to acquire, using equation 14.

$$\text{Power (HP)} = \frac{\text{pressure (bar)} * \text{flow} \left( \frac{\text{L}}{\text{min}} \right)}{450} \quad (14)$$

hence, the pump power to reach the needed pressure on the RO desalination system is 0.75 HP equivalent to 500 W power consumption.

Once the pump power and the RO membranes were assigned, the construction of the desalination system (Figure 14) was performed. Since the water potabilizer is a complex conformed of varied stages, is appropriate that every one of them is compact, hardworking, reliable in adverse conditions, and low weight, therefore, it was planned an aluminum profile structure for the entire potabilizer.



**Figure 14.- Supported RO membranes on the aluminum profile structure**

### **3.2.2. PV solar energy stage**

The electrical energy used in the potabilizer is another aspect to be determined. In this case, the desalination stage is considered, but additionally, the control system and the photoreactor are involved in the complex power consumption. Hence, calculations were made according to the electronic and electrical equipment utilized to determine the average daily power consumption value for a stand-alone PV system. Firstly, the consumption in the devices was distributed and dimensioned as shown in Table 6.

**Table 6.- Devices and their power consumption and energy per day demanded**

<b>Device</b>	<b>N°</b>	<b>P (W)</b>	<b>t (h)</b>	<b>Days per week</b>	<b>E(kWh/day)</b>
RO pump (75%)	1	412	8	7	3.296
Photoreactor pump	1	367	8	7	2.936
Charge regulator	1	390	8	7	3.120
Measuring	6	100	8	7	0.800
Nextion HMI	1	5	8	7	0.004
Arduino	1	0.3	8	7	0.0024
Items	5	4	8	7	0.032
<b>TOTAL</b>		<b>1,278.3 W</b>			<b>10.190</b>

Due to the RO pump and the photoreactor pump will not work at the same time, only the RO pump (higher value) is considered in the calculation (7.254 kWh/day) with a power factor of 75% according to the pump specifications, that's left total energy of 5.440 kWh/day. Successive to the dimensioned devices and from the total energy demanded in the water potabilizer, the number of PV modules is calculated using equation 15 where

$E_T$  is the total energy per day demanded,  $h$  is the solar hour utilized,  $F_s$  is the safety factor which is an increment determined by losses due to connection, wiring, environment (dust), battery self-discharge, etc. (10-25% is recommended) [76,77], meanwhile  $mP$  is the module power, in this case, the PV modules are 270 W output power supply. Hence, the number of panels is stated as 4.

$$N_m = E_T * F_s / (h * mP) \quad (15)$$

In a stand-alone system, a battery bank is employed to store the generated energy through the PV modules during the daytime and supply it to electrical loads as needed (during cloudy weather in this case) to provide electrical loads with stable voltages. To determine the batteries to utilize in the storage bank the equations 16 (daily battery capacity average) and 17 (number of batteries) are employed where the batteries exhibit an efficiency factor  $F_e = 0.9$ , an output voltage  $V_o = 38.23$  V, displaying an autonomy of 1 day, a  $B_c = 60$  Ah battery capacity and a discharge limit of  $D_L = 95\%$ .

$$B_{cavg} = E_T / (F_e * V_o) \quad (16)$$

$$N_B = B_{cavg} * \text{Autonomy days} / (D_L * B_c) \quad (17)$$

As a result, the number of batteries according to the  $B_{cavg} = 158.1$  Ah/day is estimated as **2.7**. However, since the potabilizer will be powered only 8 hours/day it was decided to use only 2 batteries. In [75] more detailed information on the design and construction of each component for this stage is found.

### **3.2.3. Photoreactor design**

The photoreactor stage encompasses two parts, design and manufacture. On the one hand, the reactor sizing (Total volume, rate flow, etc.) is according to the main factors that impact the potabilizer performance, and on the other hand, the collector reactor proposal design and manufacture. The latter is the main component in the photoreactor stage since it is the element that performs the function of redirecting the sun's rays to the receiving tubes for the water treatment.

#### **3.2.3.1. Photoreactor sizing**

According to J. Galvez et al. [78] when assessments for photocatalytic degradation on different substances need to be done, the generally used parameter to denote the results and the evolution of the process is the residence time ( $t_R$ ), which indicates the time of light exposure to the aqueous mixture passing through the reactor. Hence, the use of residence time does not allow comparing procedures in different systems or acquiring conclusions about their efficiency. This problem can be avoided by expressing the evolution of the photocatalytic process as a function of the effective energy that the reactor accumulates over time, instead of the residence time. This can be done using the following equation (18) that integrates the main parameters of the reactor:

$$E_{UV,n} = E_{UV,n-1} + \Delta t_n \overline{UV}_{G,n} \left( \frac{A}{V} \right); \Delta t_n = t_n - t_{n-1} \quad (18)$$

where  $E_{UV,n}$  is the accumulated energy per reactor volume unit, for a  $n$  sample of the photocatalytic process;  $\overline{UV}_{G,n}$  is the average effective incident radiation ( $W_{UV}m^2$ ) on the reactor surface in the time interval  $\Delta t_n$  between two consecutive experimental samples;  $A$  is the external surface and  $V$  is the total volume of the reactor. This relation helps to express the evolution of a photocatalytic process as a function of the energy captured by the reactor (per volume unit) and, therefore, allows to compare the efficiency of different photoreactors.

Furthermore, to calculate the necessary surface  $A_r$  for the reactor, the energy required per unit volume of the solar reactor  $Q_{UV}$  related to the annual volume  $V_t$  and operation time  $T_s$  according to the average effective incident radiation  $\overline{UV}_{G,n}$  is expressed in equation 19.

$$A_r = Q_{UV} * V_t / (\overline{UV}_{G,n} * T_s). \quad (19)$$

This stage contemplates that the potabilizer treats a water volume of  $1 m^3/day$ . In this case, to get the design and construction done, it is required to consider the factor mentioned above related to the photoreactor. Hence, recalling equation 18 and 19 which references the energy utilized in the reactor and the surface to a required volume for water treatment respectively, the following table (table 7) shows the parameters projected for the potabilizer. For the energy accumulated receiving tubes with a thickness of 0.001 m

and an inner diameter of  $D = 0.032$  m are contemplated according to the ideal parameter limit and a reactor area  $A_r = 3$  m<sup>2</sup>.

**Table 7.- Design parameters employed for the photoreactor sizing**

Parameter	Quantity	Unit
$E_{UV,n}$	647	J/m <sup>3</sup>
$Q_{UV}$	3196	KJ/m <sup>3</sup>
$\overline{UV}_{G,n}$	37	J/m <sup>2</sup>
$V_t$	365	m <sup>3</sup>
$T_s$	$10.51 \times 10^6$	s
$A_r$	3	m <sup>2</sup>

### 3.2.3.2. Photoreactor pump

In a photocatalytic reaction with TiO<sub>2</sub>, the slowest process is a mass transfer process, hence, the flow velocity inside the photoreactor is a fundamental parameter because it determines the mass transport phenomenon. A laminar flow allocates regions with different reactants concentration and decreases the contact between them and the catalyst, while a turbulent flow helps mass transfer between the solution and the catalyst and ensures a better dispersion of the reactants in the solution. Therefore, the selection of the photoreactor feeding water pumping is essential to generate a turbulent flow causing in this way optimal conditions for the photochemical reactions. To calculate the turbulent flow in a tubular path, equation 21 considers the water density  $\rho$ , the flux velocity  $u$  flowing through the inner tube in m/s, the hydraulic diameter  $D_H$  (tubes) and the viscosity  $\mu$ . The Reynolds number (dimensionless) plays a significant role, numbers  $\geq 4,000$  gives the required turbulent flow, while numbers  $\leq 2000$  provide a laminar fluid. Hence a pump that offers the optimal flow rate and power required with the lowest possible energy and cost spending needs to be projected. In this case, a ½ HP power pump with a flux velocity  $\approx 0.9$  m/s is proposed. In this way, a Reynolds number for a turbulent flow higher than the minimum demanded is obtained and guaranteed.

$$Re = \rho u D_H / \mu. \tag{21}$$

Relating the photochemical process and the caudal, Figure 15 shows the different existing technologies for the treatment of contaminants in water classified by the flow rate and the



total organic carbon load, including photocatalysis processes. As is depicted the importance for the POA and the photo-reactive process to be within the flow rate, which is expected in the photoreactor pump for the project.

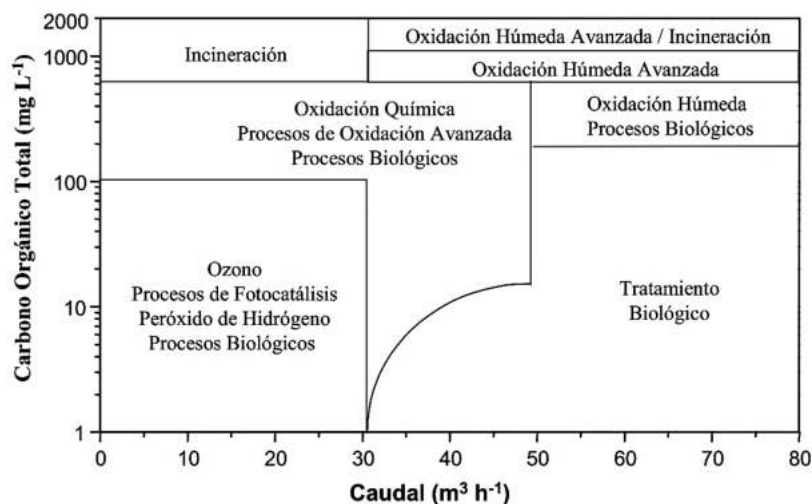


**Figure 15.- Illustration for the different water treatment technologies, associating caudal with the COT to neutralize [79]**

### 3.2.4. CPC design and manufacture

Looking for an improvement in the optical efficiency of CPCs, a manufacturing method that consists of using a 3D printed mold elaborated in a 3D printer with the given shape of a CPC profile was implemented. By using the printed mold, it is possible to eliminate the machining or manual manufacture in addition structures/clamps and joints that may deform the parabolic shape of the collector are avoided. The proposed technique has the advantage that the reflective sheet of the concentrator will not experience any kind of contact deformation since the mold is used to give the form of the involute to the aluminum sheet. Obtaining in this way, a deformation-free surface contributes to improving the capture of optical energy and thus, it is possible to concentrate and redirect the solar radiation to the receiving tubes and thus, get higher efficiency.

To evaluate this enhancement in the structure and optically-simulated efficiency of the CPC fabricated using this new technique, besides it was assessed by implementing photogrammetry and ray tracing [80]. The procedure to fulfill these two assessments are described consequently and the results evaluations are presented in chapter IV. This methodology generated an article that was accepted for publication during the period of this project, more detailed information on the paper is found in Annex B.

### 3.2.4.1. CPC fabrication process using a 3D-printed mold

From the 2D-involute (Figure 9), the 3D design that functions as a mold for the 1-Sun collector is performed. Processed in AutoCAD® 2019, the scheme goes from 2D-involute to becoming the 3D mold of the collector shown in Figure 16. The mold design consists of 4 pieces (male-female) assembled and fabricated with dimensions limited to the 3D printing parameters of 99.4 x 330 x 40.9 mm. Thus, reaches the length necessary to cover the whole size of the receiver tube (1320 mm) in this case for low concentration (1-Sun). The mold was fabricated in a 3D printer that uses a 1.75 mm PLA filament thickness (Figure 17).

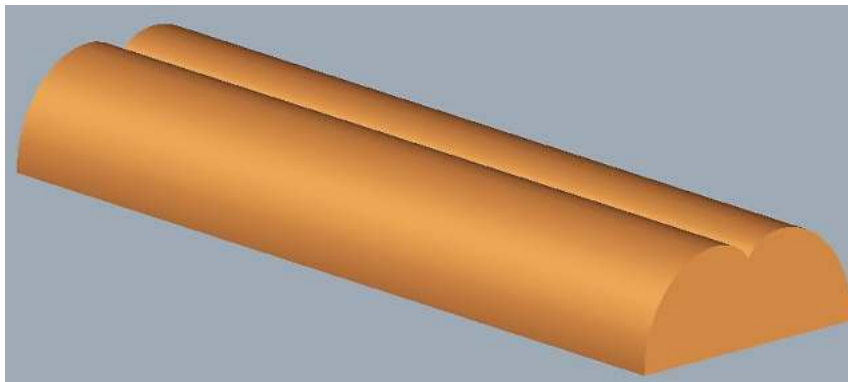


Figure 16.- 3D Mold AutoCAD design used for the 3D printer



Figure 17.- 3D-Mold male piece (left) and assembled pieces forming the CPC 3D-Mold.

In addition, to achieve that the printed mold gives the geometric shape to the aluminum sheet, a steel container was developed. The steel container affords the adequate deposit to conserve the mold and the aluminum sheet together when are under tension causing the latter shapes the CPC designed. The mold, aluminum sheet and steel container are exposed in Figure 18.



**Figure 18.- 3D-Mold and aluminum sheet inside the container developed.**

To obtain the appropriate CPC shape of the aluminum sheet, styrofoam is added to the aluminum and the mold previously placed into the steel container. In this way, styrofoam exerts pressure on the aluminum sheet against the mold as it increases its volume all over the container taking the shape of the collector expected without the need of using fasteners.

The process to produce the polyurethane foam is done simply and consists of a mixture of A and B components which are combined in a 50:50 ratio with 20 s of reaction time to start expanding and a drying time of 4-6 hours depending on the temperature and density of the components.

Figure 19 exhibits the manufacturing methodology used. Where the flat surface of the mold is placed in the container (Figure 19a). Then, the aluminum sheet is cut according to the calculated CPC design and positioned on the mold molding it to the parabolic design (Figure 19b). Once both (the sheet and mold) are inside the steel container, the styrofoam mixture (A-B) is added and instantaneously after that, the steel container is sealed (Figure 19c). The A-B styrofoam mixture changes into an expanding foam as a chemical reaction result, pressuring the high-reflective sheet against the mold and reproducing the designed CPC profile (Figure 19d). As a final point, after the drying time, the mold is removed from

the collector and a parabolic sheet with the CPC shape and a styrofoam bottom is obtained (Figure 19e).

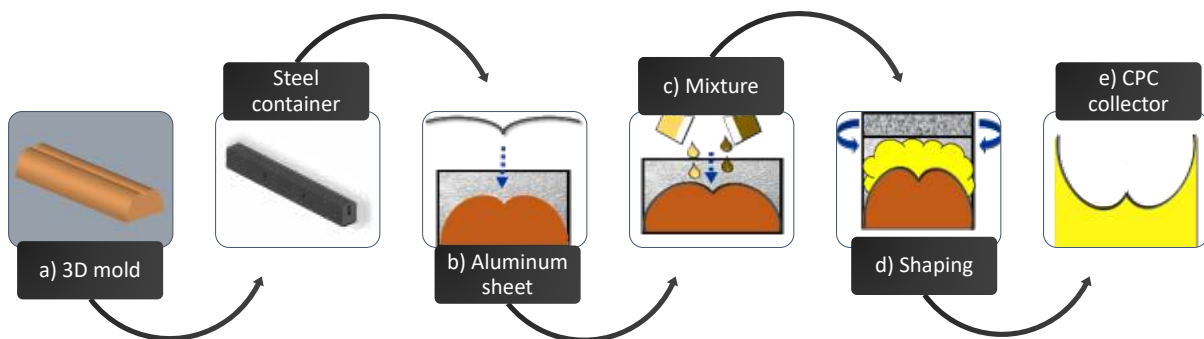


**Figure 19.- CPC manufacture technique.** a) the mold is placed into the steel container, b) the aluminum sheet is situated over the mold, c) styrofoam is poured, d) instantaneously locked and e) the CPC is obtained.

As a result, a molded CPC profile with less damage on the surface of the high reflectivity coating and reduction deformations due to its machining processes is obtained as shown in Figure 20.



**Figure 20.- Final result of the CPC Collector built with the 3D mold**

To accomplish the parallel comparative evaluation with the 3D-Molded CPC a conventionally manufactured CPC was contemplated. It is worth mentioning that there is no fully established methodology, however, the most suitable way is by rolling and machining the aluminum sheet to form the needed collector, such as the one contemplated for the analysis (Figure 21).



**Figure 21.- Conventionally manufactured CPCs assembled in a special structure to maintain the collector shape.**

### **3.2.4.2. Collectors efficiency assessment**

Regarding the collector evaluation, a photogrammetry methodology was developed to validate the result of manufacturing the collector and calculate the deficiencies in the surface sheet shape-CPC. Figure 22 shows the procedure to perform a 3D-surface reconstruction processing photographs taken of the object to be studied.

The processing was executed through the photogrammetry software Caesoft® (v. 2016.0.5.1718). To perform this technique, a 2 mm dot pattern with a 5 mm separation between each dot defined by the software (Figure 22a) was printed on vinyl and deposited all over the CPC surface (Figure 22b) so the printed dots takes the shape of the evaluated collector (Figure 22c). Then, using a Nikon® D3000 camera, photographs from distinct points around the pattern covering the collector were taken. Afterward, the images acquired were treated and processed through the PhotoModeler software [52,81].

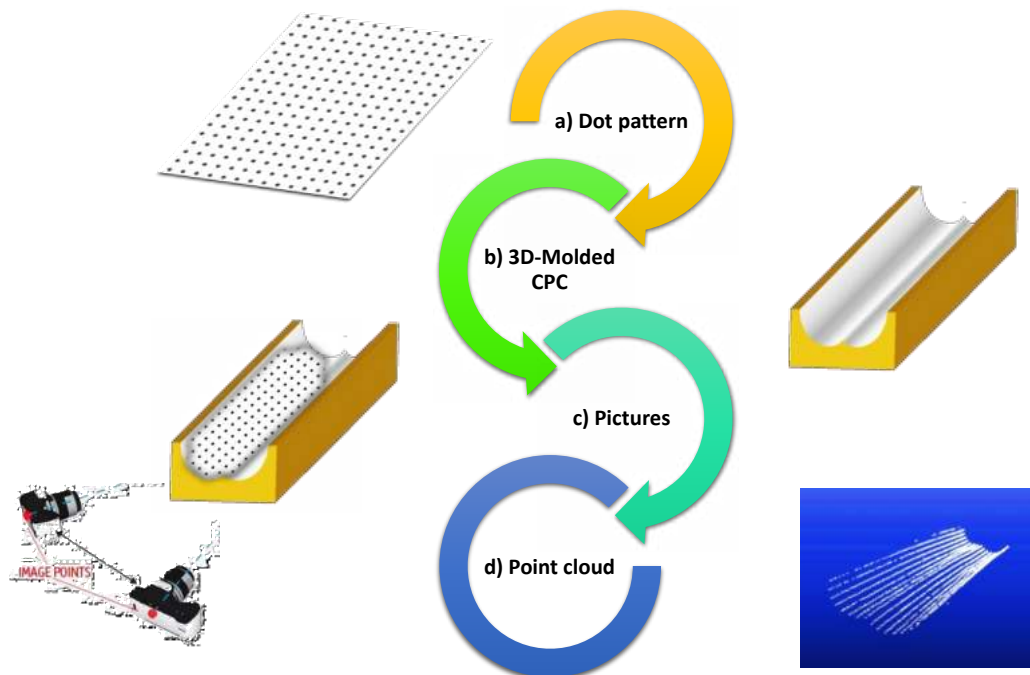


**Figure 22.- Photogrammetry technique: a) vinyl placed on top of the b) CPC collector and c) a sequence of pictures are taken to process and d) a point cloud is generated.**

Two types of evaluations were made to evaluate the construction of the 3D molded collector: 1) Photogrammetric assessment (by a mathematical process) and 2) ray-trace analysis based on the data previously generated by the PhotoModeler software.

The closest dot algorithm was used to evaluate the CPC 3D surface, obtained by the technique used with the polyurethane foam, and thus compare it with a 1-sun ideal collector previously designed for the 3D mold (Figure 9).

In addition to the closest dot algorithm by a mathematical process, an additional feasible evaluation using the data obtained in an innovative ray-trace analysis was made, where a flux chart for the procedure is shown in Figure 23. Treating the dot pattern of the images obtained (Figure 23a), the PhotoModeler software generates a 3D layer collector (Figure 23b) and is exported to the design software AutoCAD® in a .STL file to process it and with this arrangement manipulate it in Tonatiuh.

Utilizing the generated 3D layer model in the AutoCAD® software a pretreatment was made (Figure 23c) where a refined mesh was assigned to the 3d layer collector. This procedure helps to shape smaller regions on the whole model.

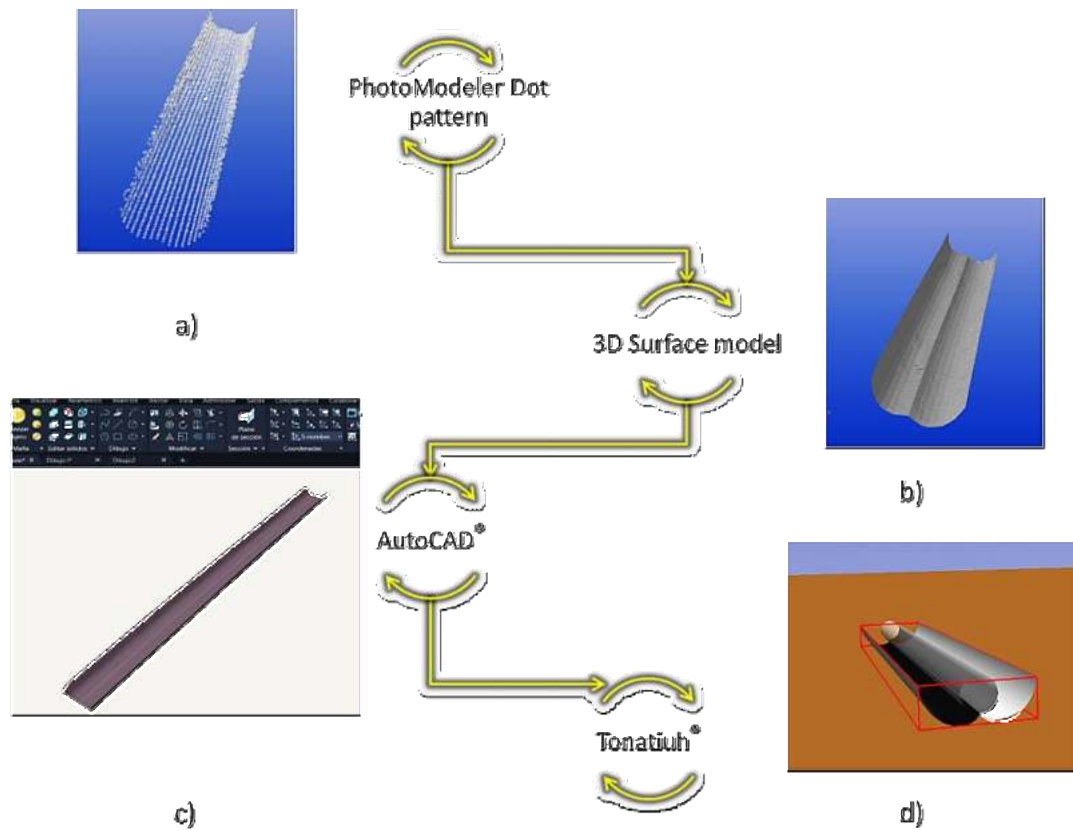


**Figure 23.- Flux chart of the procedure to treat in AutoCAD the dot pattern obtained and simulate the model generated in a ray-trace software.**

A new file of the meshed collector model was generated, which can be used in the Tonatiuh® software (v. 2.2.4). The software consists of a 3D ray tracing Monte Carlo algorithm in this case utilized for the optical simulation of the solar collector structure. It allows the comparison of the 3 studies; ideal, 3D-molded, and manually manufactured 1-sun CPC collector on its collecting efficiency by simulating the optical behavior of the system. For this simulation, an inclination of the collectors of 21° in a 21.00 latitude and -102.00 longitude sun position was stipulated as boot parameters. Regarding these aspects, the receiver tube has 96% and 95% of absorbance and reflectance respectively as optical parameters.

### 3.2.5. Control system

This stage involves on the one hand the system control for the water monitoring and sensing and on the other hand power circuit related to the pumps and devices utilized throughout the whole water streaming process. Therefore, the stage is distributed into two parts; the digital control and the power circuit, being the digital control operated by those devices that utilize digital signals and low power voltage. On the other hand, in the power

circuit; pumps, circuit breakers, contactors, push buttons and high-power instruments are supported. Hence, the next sensing devices and power instruments (described in table 8) were planned to be utilized according to the main requirements to reach the quality parameters. Thus conductivity, dissolved oxygen, and flow, among others measured, automated, and operated in this system.

**Table 8.- Digital control and power circuit devices and materials list and its specifications**

<b>Device</b>	<b>Reads</b>	<b>Range</b>	<b>Accuracy</b>
Industrial pH Probe	pH	0 - 14	+/- 0.002
Dissolved Oxygen Probe	mg/L	1 - 100	+/- 0.05
1/2" Flow Meter	L/min	19 - 114	+/- 10%
Industrial Conductivity Probe K 1.0	µS/cm	5 - 200,000	+/- 2%
pH Embedded Dosing Pump	mL/min	0.5 - 105	+/- 1%
Level sensor	V	5-24 VDC	± 0.020 in
3 way valve ¾	V	24VDC	-
3 way valve ½	V	24VDC	-
Arduino Mega board	16 analog I/O ports 54 digital I/O ports	0 - 5 V	-
4 channel relay	4 CH	Input: 5 VDC Output: 24 VDC Output: 250 VAC	-
HMI Nextion enhanced display 7"	I/O signal	5 VDC	-
Regulated Power Supply 5 VDC	-	Input: 100-240V AC Output: 5V, 3.6 A	-
Regulated Power Supply 24 VDC	-	Input: 100-240V AC Output: 24V, 1.2 A	-
2 TeSys Deca contactors	-	Operational voltage: <= 690 VAC and <= 300 VDC Control voltage: 24 VDC	-
2 green start push button	Normally open (NO)	Operational Current: 3 A at 240 VAC	-
1 red stop push button	Normally closed (NC)	Operational Current: 3 A at 240 VAC	-
1 Emergency stop switching off button	Normally closed (NC)	Operational Current: 3 A at 240 VAC	Turn to release

To schematize the entire control system performance, a component linkage graphical depiction is shown in Figure 24, where the main automation route is divided by two devices; an Arduino Mega microcontroller board and a 4-channel relay. The Arduino board



receives the signals (digital and analog) coming from the pH, dissolved oxygen, electric conductivity, flow, and level sensors. Subsequently, the Arduino board sends signals programmed for the actuation devices (pumps, valves, etc.) to the 4-channel module, which receives the assigned tasks according to the water status (level tank or quality) and initiates the open/close valve task or the start/stop pump according to the status case. Furthermore, the system automation displays the status of every sensor and water cycle on the Nextion HMI screen previously configured and programmed.

The control stage incorporates level sensors (high and low) connected to each storage tank. Initially, the RO feeding tank is full and the system starts activating the RO pump, in this stage the desalination process recirculates the polluted water in the RO membranes to obtain permeate water, therefore the parameter to read is the conductivity. Whereas this factor is  $\geq 800 \mu\text{S}/\text{cm}$  the water is recirculated via a  $\frac{1}{2}$  3-way valve (closed) to the RO feeding tank, once a value lower than  $800 \mu\text{S}/\text{cm}$  is read, the  $\frac{1}{2}$  3-way valve opens the line to the photoreactor tank until filling it up (detected by a high-level sensor).

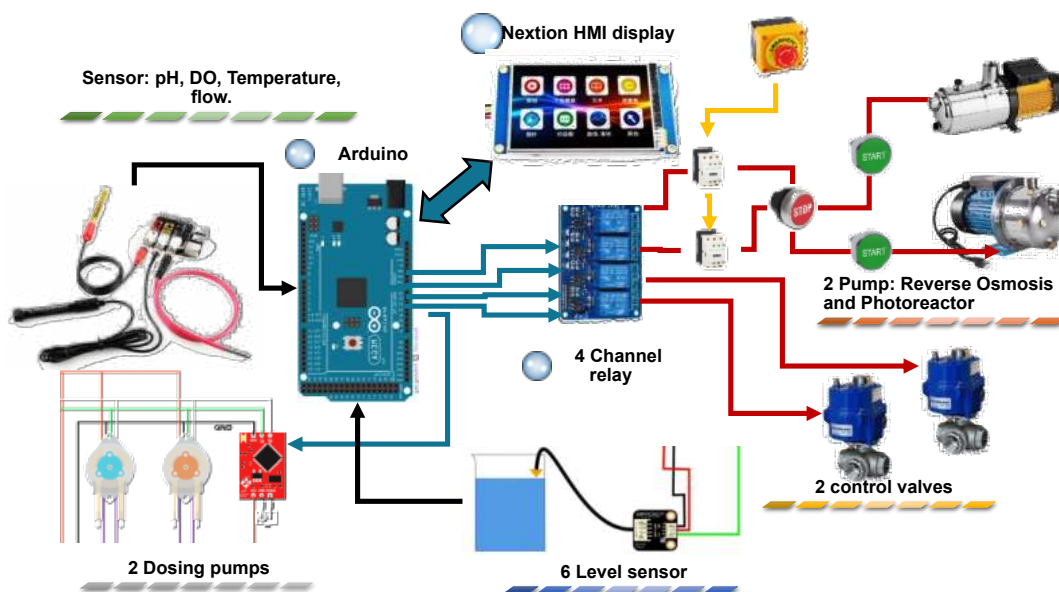


**Figure 24.- Control system graphical depiction**

Immediately, the RO pump stops its operation and the  $\frac{1}{2}$  3-way valve waits for the water status to get back to its initial position (closed) and the photoreactor pump starts working followed by a flow meter to observe the pump functioning and the turbulent stream into the photoreactor tubes.

At the end of the line, there is an OD and pH sensor to measure the water treated once have traveled within the entire tubular solar reactor. If the OD is  $\leq 6$  mg/l the water is sent through the  $\frac{3}{4}$  3-way valve (closed) to the photoreactor tank, while if the value is higher than this limit, then the  $\frac{3}{4}$  3-way valve opens the line to the final storage tank. On the other hand, a pH range = 5-8 in the photoreactor is required due to the photochemical reactions are improved at this pH scale. If the water is out of range, a data signal is sent by the pH sensor to the Arduino, and thus dosing pumps (high and low pH) regulate the pH in the photoreactor tank to its optimal level, it is worth mentioning that only the OD sensor activates the 3-Way valve and the pH activates merely the dosing pumps.

Finally, the final storage tank gathers the clean water coming from the photoreactor stage. This tank includes two level sensors (high and low), on one hand, the low-level sensor indicates that the tank is available for the reactor pump to fill it up and on the other hand, the high-level sensor sends the signal to the Arduino to stop the photoreactor pump and the  $\frac{3}{4}$  3-way valve back to its initial position (closed) according to the water conditions.

All these measurements and tasks are displayed in a Nextion HMI screen via Arduino to show the readings of the instruments, change the pH ranges (if necessary), and access the status information in case of maintenance or report.

Despite the system is fully automated it counts with a manual start, stop, and emergency stop button for the pumps through the use of two 24 VDC contactors in case of probes, start-up, or malfunctioning to name a few.

To illustrate the overall stage a piping and instrumentation diagram (P&ID) was outlined in Figure 25 to notify the path and lines in the process as well as the placing of the instruments and equipment for installation and register.

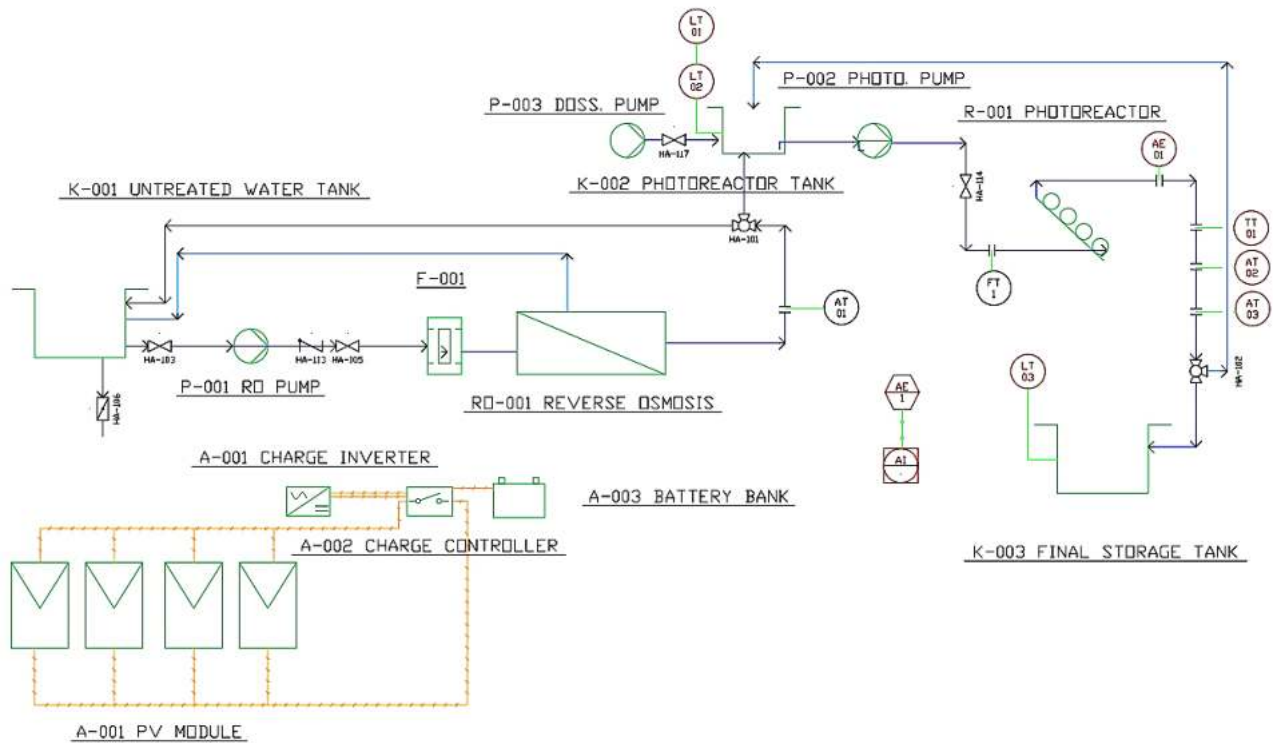


**Figure 25.- P&ID traced to indicate the lines and components in the control stage.**

In addition, to illustrate the particular sections in the control stage, schemes for the two segments were correspondingly made; both the control circuit and the power circuit. To specify the connection network for the instruments and devices in each segment. Thus, Figure 26 shows the digital control circuit meanwhile Figure 27 exhibits the power circuit.

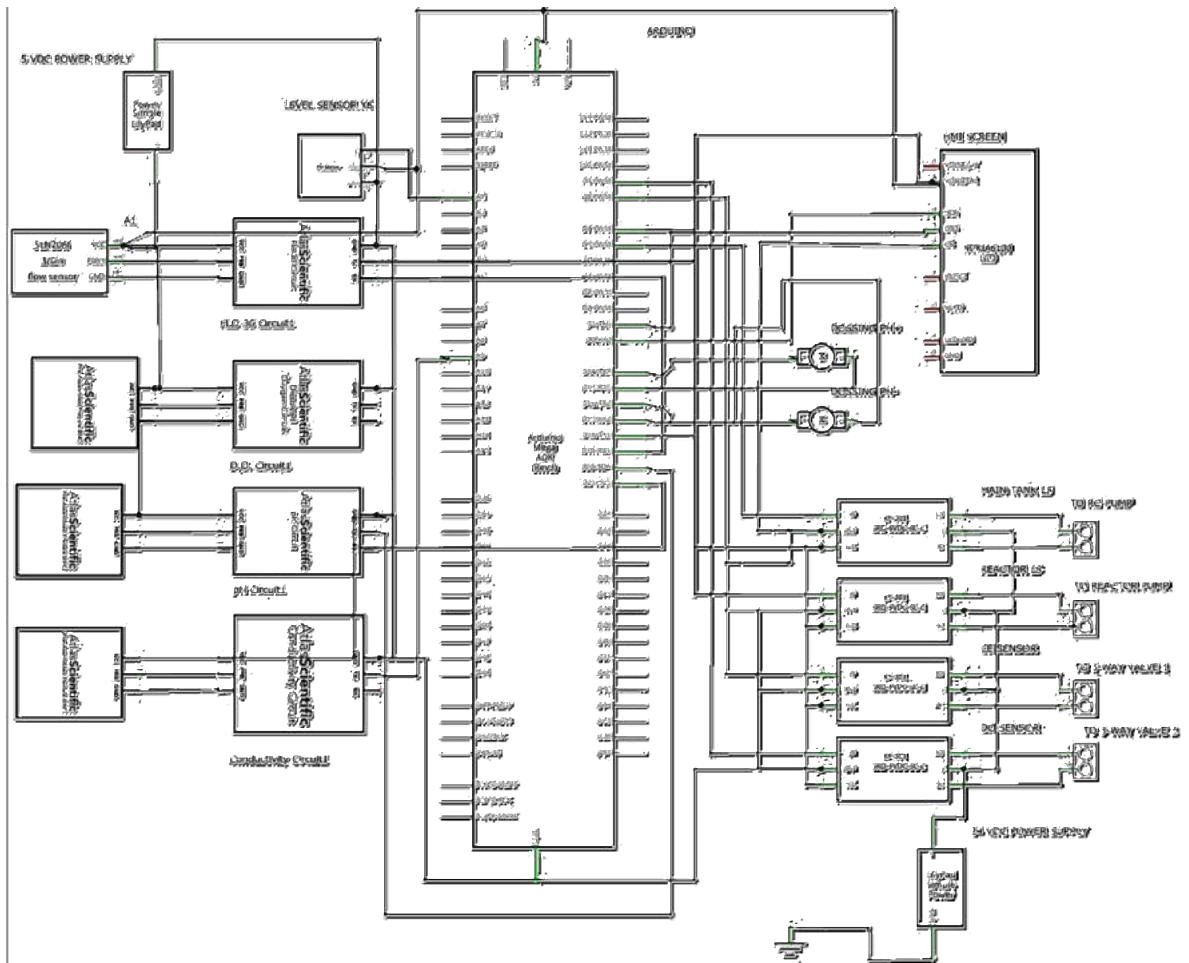


Figure 26.- Digital control circuit designed to run the programmed task according to the signals from main and reactor tank level (high and low), CE and DO sensors.

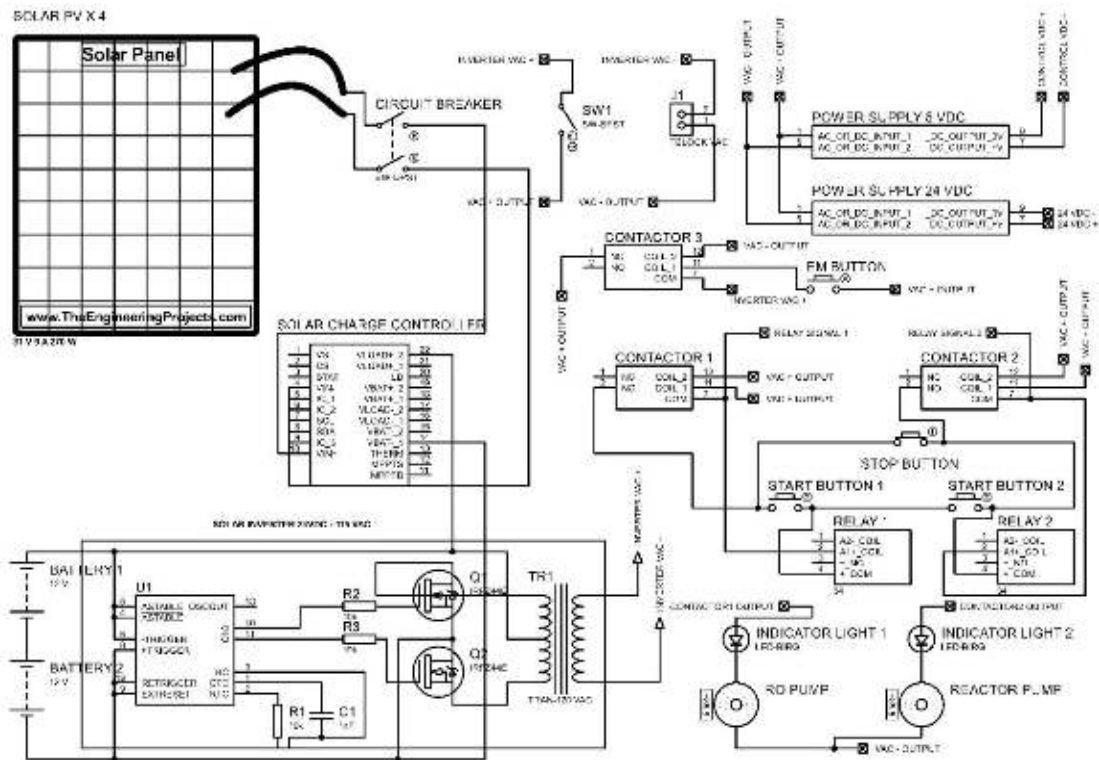


Figure 27.- Power circuit assembled to operate the high-power equipment controlled by the digital control circuit.

### 3.2.6. Integral Potabilizer 3D Model design

Once the stages were determined, the prototype potabilizer 3D model was scheduled and designed. The model was sketched in CAD software using the measures and sizing of each element and device included in every stage. Figure 28 shows the altogether stages making up the potabilizer conceptual prototype. As described before, the potabilizer consists of 3 storage tanks (Left, center, and right) selected for the desalination system, the photoreactor, and the clean water storage respectively. The PV modules for the stand-alone system were placed as follows; two foldaway modules in the back (for transportation if it's the case) and above the photoreactor tank to save space owed to its extension.



**Figure 28.- Potabilizer 3D model CAD designed showing the altogether stages (front view).**

On the superior front is allocated the solar photoreactor containing the CPC collectors and its 20 receiving tubes used for the water photochemical treatment process. In the front below is distributed the control stage made up of the Control-Power station in an outdoor electrical cabinet next to the battery bank. Right below the photoreactor (shown in Figure 29), is found the desalination stage constituted by the RO pump, carbon water filter, the two RO membranes, and the conductivity sensing device.

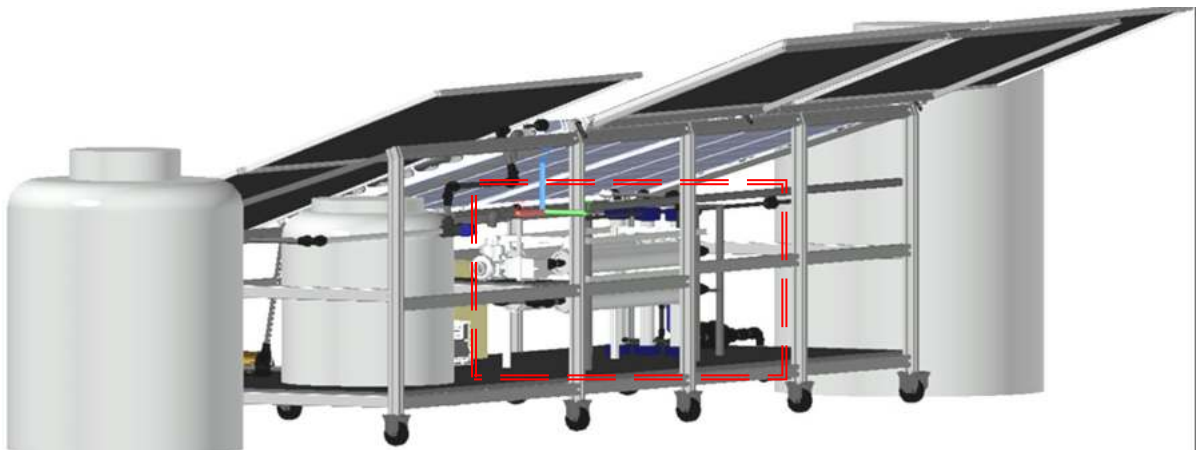


**Figure 29.- Potabilizer 3D model CAD designed (back view), RO stage is marked in the red dashed box.**

### **3.2.7. Equipment and materials**

Once the devices, instruments, and material have been schemed and designed (3D-model), the equipment selection, quotation, and acquisition were made. For the selection, all materials were designated stage by stage and their sizing was considered in the 3D model.

In table 9 the principal equipment, devices, and material list are presented according to their prices (offered in 2017-2018) to picture an estimate and relate it to the cost-benefit when 1 m<sup>3</sup> of water is decontaminated.

**Table 9.- Most relevant quotes in device and materials for the integral water treatment plant construction (in USD)**

System/stage	Device/material	Quote
Stand-alone PV	Modules, Batteries, Inverter, wiring, etc.	\$ 2845.00
Hydraulics	Pipe tubes, PVC elbows, union pipes, hosepipes, etc.	\$ 143.00
Desalination	RO membranes, filter, pump, feeding tank, etc.	\$ 948.00
Sensors	Sensors: pH, temperature, DO, level, etc.	\$ 2370.00
Mechanical structure	Aluminum profile, alucobond, junctions, nuts and bolts, etc.	\$ 2133.00
Photoreactor	Photor. Pump, photor. Tank, PMMA tubes, anodized aluminum sheet, etc.	\$ 2844.00
Control/Automation	HMI display, Arduino, wiring, 3-way valves, etc.	\$ 711.00
Samples	Water analysis	\$ 380.00
<b>Total</b>		<b>\$ 12,370.00</b>

Afterward, the quotation for every section was required, that is, hydraulic, electrical, electronics, construction, and PV. Subsequently, the equipment was required for the stores and suppliers where the main components and equipment are visualized in Figure 30. Having all the materials was proceeded to manufacture the water potabilizer, whose construction, start-up, and results obtained by the stages are described and exposed in chapter IV.



**Figure 30.- Main components and materials to develop the prototype**



## 4. Chapter IV: Results

### 4.1. WATER POTABILIZER ASSEMBLY

Once the equipment was acquired the entire system was assembled according to the stages schemed by the 3D model. Therefore, to follow a structure sequence, the first stage built was the desalination stage followed by: the support structure, stand-alone PV, photoreactor, collectors, hydraulics, and finally the control system stage.

#### 4.1.1. Desalination stage

This stage was structured using an aluminum profile as base support and consists of the feeding tank followed by the RO pump that is connected at the feeding side to a carbon water filter and afterward the RO membranes having the electric conductivity sensor at the permeate outline fixed to the 3-way valve, meanwhile, the rejected outline leads to the feeding tank inflowing to a recirculating process. On the 3-way valve, one way of the valve leads to the photoreactor tank if the quality is found within the standards, and the other way of the valve streams to the feeding tank if the quality is out of the NOM limits, Figure 31 exhibits the arrange to evaluate this system, where the stand-alone PV system was evaluated too.

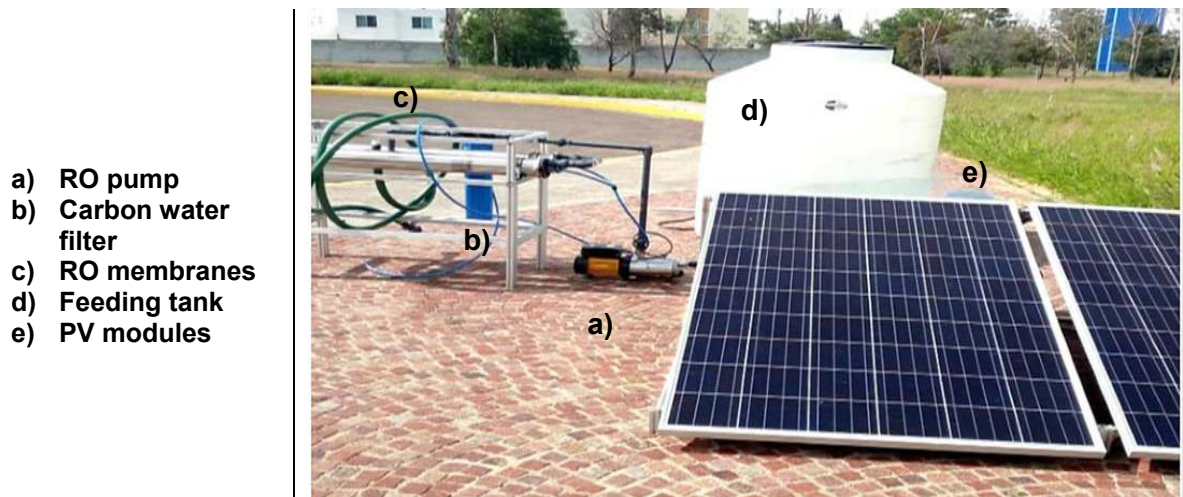


Figure 31.- Desalination system arrange to test its performance

The desalination stage was assessed by running 3 water samples prepared with different concentrations, the nominal values evaluated were 689 mg/L, 1245 mg/L, and 1510 mg/L respectively. It is worth mentioning that the desalination system does not completely prevent the treated water from containing a minimum of minerals. Nonetheless, high



pressure in the membranes at the inflow (within the limits) guarantees an effluent with an acceptable minerals quantity according to clean water standards.

Table 10 shows the results from the 3 concentrations measured using the electric conductivity sensor designated for the potabilizer system compared to the Official Mexican Standards (NOM-127). Furthermore, table 11 indicates samples chosen from commercially bottled water evaluated to verify and support the desalination system performance, these studies were compared too.

**Table 10.- Inflow and Outflow desalination evaluation**

Parameter	NOM range	Sample	Inflow	Outflow
EC ( $\mu\text{S}/\text{cm}$ )	50-600	1	1400	54.4
		2	2460	40
		3	2960	45
TDS (mg/L)	$\leq 1000$	1	689	25.5
		2	2460	18.65
		3	2960	24.7

**Table 11.- Commercial bottled water and desalination system comparison. Adapted from [75]**

Parameter	NOM limit	Commercially bottled water	Concentration
TDS (mg/l)	$\leq 1000$	Ciel	110
		Bonafont	164
		Water Dispenser	19.64
		Desalination system	18.65

#### 4.1.2. Support structure

Based on the schemed water potabilizer 3D model design the support structure was built using aluminum profile series 25x25 and 50x25 and an alucobond made flat bottom base. The water potabilizer overall dimensions are 4.1x1.1x1.28 m in length, width, and height respectively. The structure dimensions of the most significant pieces used to raise the base are detailed below in table 12.

**Table 12.- Most significant structure pieces to build the water potabilizer**

Profile quantity	Size	Type	Depiction
2	410 cm	50x25	Potabilizer frame base: front and back
5	64 cm	50x25	Front legs
4	110 cm	50x25	Back legs

10	128 cm	25x25	The frame supports: base and laterals
12	85 cm	25x25	The frame supports: front and back (bottom and top)
10	10 cm	25x25	The frame supports: Collectors

In Figure 32 can be seen the structure base where the potabilizer stands, it is important to highlight that the entire structure was designed to have wheels to move it if necessary.



**Figure 32.- Structure base for the solar water potabilizer**

#### **4.1.3. Stand-alone PV stage**

For this stage, four PV modules were selected and installed in the potabilizer system to supply the required electrical energy to the whole process. The stand-alone stage was evaluated simultaneously with the desalination stage due that this stage has the higher power consumption. The evaluation of the PV modules was performed under clear sky conditions in December 2017, in Figure 33 presents the dependence of the power required by the system over the incident solar radiation, despite dispersion present (related to an electrical pump connection problem in the installation) a linear distribution is observed in the PV operation.

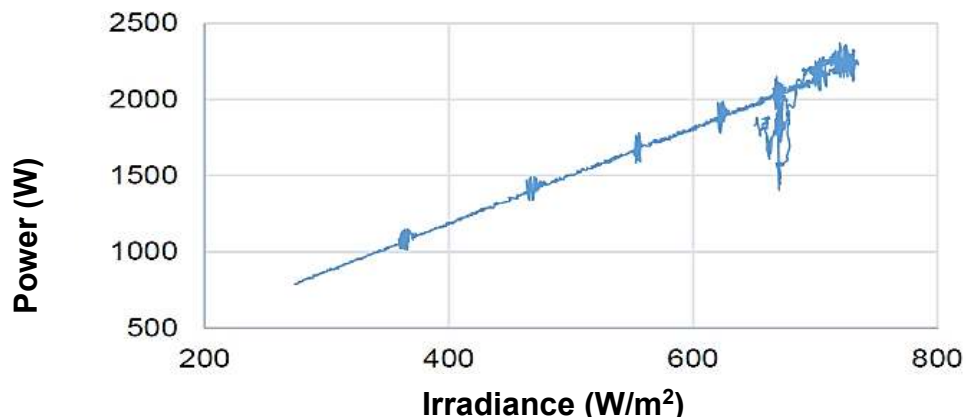


**Figure 33.- PV performance displaying the power dependence related to irradiance**

The evaluation was made using 2 PV panels, since these accomplish the charging batteries function (connected in series) and the DC-AC solar power inverter supplied by such batteries going from 24 VDC to 120 VAC, distributing power to the RO pump of the feeding water tank. Figure 34 shows the prototype structure (for performance test only) of the panels including the mentioned components.

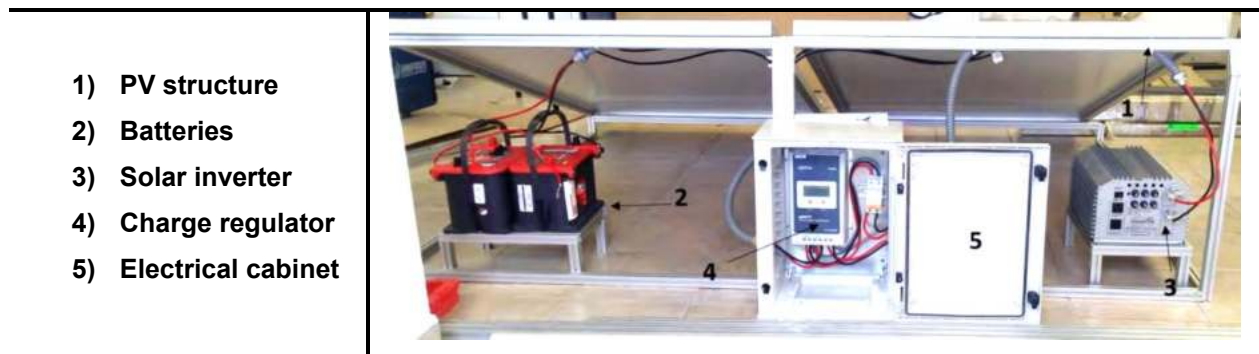


**Figure 34.- Stand-alone PV prototype structure to test its performance. Adapted from [75]**

After evaluating the stand-alone PV performance in the prototype structure, it was placed on the water potabilizer, using the 4 module panels previously calculated. Two panels were located at the top of the reactor tank to save space, meanwhile, the other 2 panels were assembled in the back of the potabilizer to fold them since it is desired to make it mobile and adaptable when transported. Hence, the PV panels were mounted to a frame previously coupled by 2 multi-angle profile connectors joints to the potabilizer, and at the edge of the frame 3 foldable pods stand as is shown in Figure 35.



**Figure 35.- Stand-alone PV installation on the water potabilizer structure**

#### **4.1.4. Photoreactor**

This stage is composed of 2 main components; the structure base and the solar collectors CPC in addition to its components (tubes, hydraulic elements, etc.). The first one was manufactured as two rectangular steel frames having dimensions of 1.3 x 1.2 m with 10 circular inlets and outlets on the sides (left and right) of 3.4 cm diameter for the tubes and separated every 12 cm to distribute the borosilicate receptor tubes simultaneously with the collectors, the structure can be seen in Figure 36. Because the maximum sun energy utilization is desirable, this frame structure has an inclination of 21° according to the Aguascalientes area sun conditions. Using this arrangement, the optimal conditions can be reached.



**Figure 36.- Structure frames on the top of the structure (left side) utilized to mount the collectors**

#### **4.2. CPC COLLECTORS**



The main photoreactor element probably is the collectors that help to fulfill the task of concentrating the sun rays in the receiving tubes. The processes and methods for the 3D-molded CPC's fabrication were described in section 3.1.5, hence the resultant collectors are exposed in Figure 37 where the 20 collectors are mounted in the structure frames to cover the reactor area considered to be irradiated.



**Figure 37.- CPC collectors mounted on the top of the photoreactor structure**

To evaluate the 3D fabrication method, a hybrid assessment was applied employing the photogrammetric and ray trace methods. These test associates the collectors manufactured with the presented methodology in chapter III versus one manufactured by conventional machining technique, the procedure presents the advantage to improve the CPC quality profile with less damage on the surface of the high reflectivity coating and reduction deformations due to its machining processes. The results obtained in the evaluations are presented below which are separated into two: the one with the photogrammetry technique and the optical assessment using a ray tracing method.

Additionally, the Solar Advisor Model (SAM) software was used to estimate the thermal energy produced by the CPCs to evaluate. This software uses equation 22 to characterize the collector's performance in a steady state as follows:

$$Q_u = A \cdot [\eta_{opt} \cdot FR_{\tau\alpha} \cdot \kappa_{\tau\alpha}(\theta_b) \cdot G_I - FRU_L(T_i - T_{amb})] \quad (22)$$

where:

$Q_u$ - Solar field useful gain (kW)

A- Total system collector area ( $m^2$ )

$\eta_{opt} \cdot FR\tau\alpha$  - Optical gain

$\kappa_{\tau\alpha}(\theta_b)$  - Modifier at AM 1.5

$G_I$ - Incident solar irradiance normal to the collector plane  $W m^{-2}$

$FRU_L$ - Thermal loss coefficient

$T_i$ - Solar field inlet temperature of the working fluid

$T_{\infty}$ - Dry bulb temperature

The optical gain factor ( $FR\tau\alpha$ ) was deduced as a function of the average CPC optical efficiency as shown in Table 13.

**Table 13.- Relative gain in equation 22 as a function of the collector efficiency.**

Type	Average optical efficiency $\eta_{opt}$	Coef. $\eta_{opt} \cdot FR\tau\alpha$
Ideal CPC	1	0.607
3DM - CPC	0.95	0.57665
CM - CPC	0.82	0.49774

The main parameters considered in the SAM simulation (Table 14) were:

**Table 14.- Simulation parameters behaved for the solar system (water heating)**

Parameter	Value
Average hot water usage	1000 L·day <sup>-1</sup>
Collector tilt angle	22 °
Total system flow rate	0.83 kg·s <sup>-1</sup>
Working fluid	Water
No. of Collectors	15
Collector Area	2.78 m <sup>2</sup>
FR $\tau\alpha$	0.607, 0.57665, 0.49774
FRUL	3.72 W·m <sup>-2</sup> °C
Incident angle modifier	0.95
Test fluid	Glycol
Test flow	0.0556 kg·s <sup>-1</sup>
Solar tank volume	1000 L
Outlet set temperature	80 °C

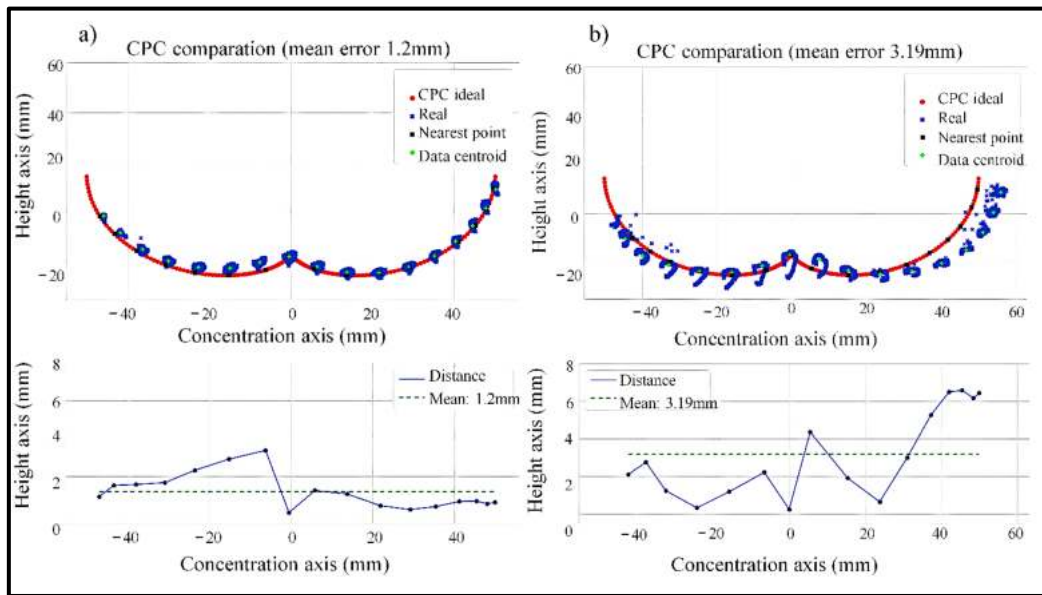
#### 4.2.1. Photogrammetric evaluation

Figure 38a (up-left) exposes the 3D-molded CPC data processed running the photogrammetry software which are plotted in blue dots and its mean absolute error

(down-left) is compared to the ideal 1-sun collector CPC, plotted with red dots line and elaborated in Matlab software following equations 9-13.

Likewise, Figure 38b exhibits the CPC handcraft manufacturing comparison (up-right) and its mean error (down-right) along the x-axis, where traditional techniques (bending, punching, etc.) were used. The 3D-mold CPC mean error indicated in Figure 38a around 1.2 mm is noteworthy according to the technique. Demonstrating that the manufacturing technique can be noticeably approached to the ideal shape of the collector ideally designed.

The results demonstrate that the traditional fabrication technique has a greater mean error (3.19 mm) when used. Figure 38b illustrates how the involute does not reach the curved shape, especially at the collectors' borders, this consequence may be attributed to the traditional manufacturing technique.



**Figure 38.- Ideal 1-sun collector (red dotted line) and its comparison with the 3D-mold technique (a) and the traditional procedure (b), below their mean error.**

The mean absolute error (MAE) could have two origins, 1) the considerably extensive CPC collector which is 1300 mm and 2) the number of clusters in data centroids, being a complex number to process for the software. Nonetheless, using the data processed in the software the root means square standard error (RMSE) was calculated. The RMSE value calculated is  $\pm 0.01$  px or 0.002 mm.

### 4.2.2. Ray trace evaluation

To perform this evaluation, the Tonatiuh software was used to process the data obtained using the methodology described in section 3.2.4.2. For this software, the flux distribution uses the surface divided corresponding to a regular grid of equal-area cells.

Using Tonatiuh® software, a Monte Carlo ray trace studio was simulated for the three surface models in the same solar conditions (angle, position, location) to evaluate the concentrating performance. Figure 39 shows a way to illustrate the ray trace simulation for a 21.00 latitude and -102.00 longitude sun position to compare the ideal, 3D-molded, and traditional manufactured CPC at a point in time.

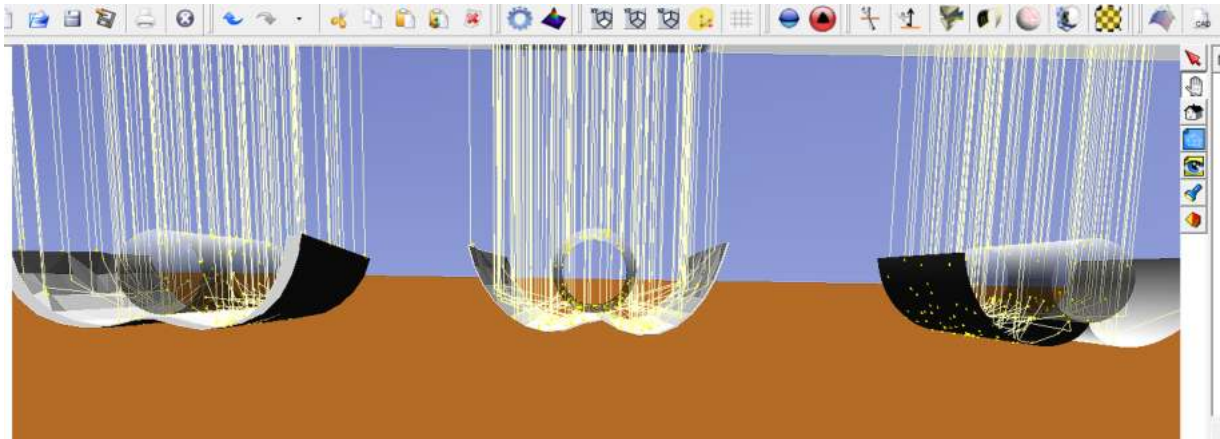


**Figure 39.- Ray trace simulation environment for all CPC configurations: ideal (right), 3D-molded (center), and manually manufactured (left) CPC.**

This evaluation consists in estimate the solstices and equinoxes (four-day) to relate and determine the collector's efficiency and proficiency of the ideally designed 1-sun collector against the 3D-molded (3DM-CPC) and the conventionally manufactured (CM-CPC), evaluating hourly each one of the 4-day on a period of 9 hours the radiative flux collected for the receiving tube by ray trace simulation, obtaining the results displayed in Figure 40.



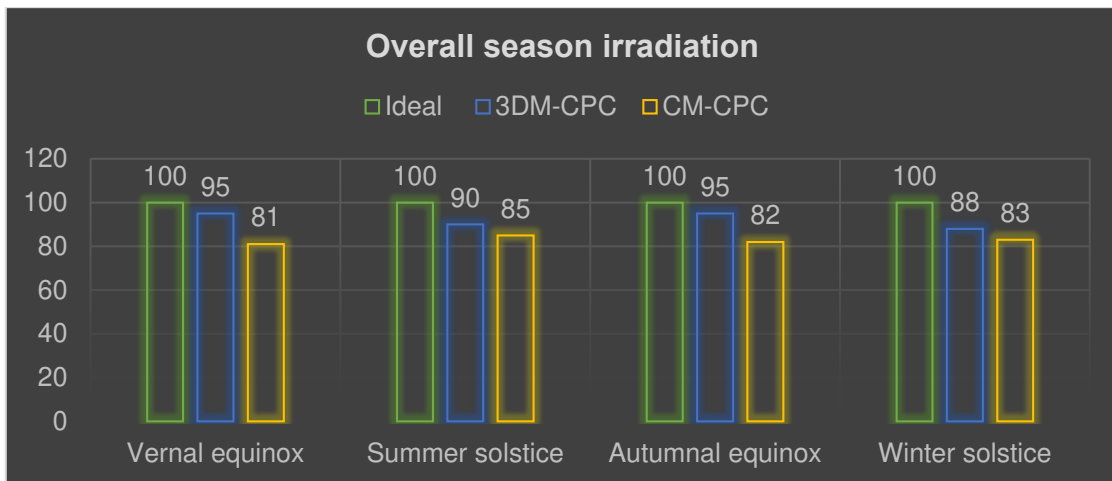


**Figure 40.- Shows the ideal 1-sun, 3D-Molded, and conventionally manufactured CPC performances for the 4-day seasons; March 21 (Vernal), June 21 (Summer), September 23 (Autumnal) and December 23 (Winter) corresponding to the equinoxes and solstices**

Figure 40 exhibits the solar irradiation hourly in each collector simulated on the four dates using the sun irradiation integrated mathematically. The data collected hourly are computer-generated for every collector modeled in the Tonatiuh software. Then, a data summation of the different irradiance runs (hourly solar day) is calculated and measured as the average irradiation resultant (irradiance/time). Finally, this integral irradiation estimate is employed to display the area under the curve for each season on that four dates; solstices and equinoxes (represented by the bar graphs). Thus, the concentrating capability of the 3DM-CPC and a CM-CPC were simulated and contrasted with the ideal 1-sun CPC.

As can be seen in the last Figure, the difference between a conventionally made and a molded collector is relevant. The methodology for the construction of the proposed 3DM-CPC and the one using CM-CPC methodology showed a higher solar collection efficiency factor for the 3DM-CPC over the CM-CPC.

The 3DM-CPC obtains a 95 % max – 88 % min meanwhile the CM-CPC has an 85% max – 81% min range considering the ideally designed collector as a 100% percent efficiency factor. As can be seen, the 3DM-CPC is close to the ideal shape due to the manufacturing technique despite having a small number of inaccuracies in the collecting surface. Figure 40 validates the difference between the methods to fabricate, being the most efficient the 3DM-CPC, followed by the CM-CPC collector shape compared to the ideally designed 1-sun collector on the four graphs.

### 4.3. AUTOMATION AND CONTROL STAGE

This stage consists of processing the data acquired by the sensing devices and performing the programmed tasks at every stage in the water potabilizer according to the required needs such as; open/close valves, start/stop pumps, and display water conditions. Due to the nature of the system, it is necessary to divide its environment into two parts; the digital control circuit and the power circuit, being in the digital control those devices that utilize digital signals and low power voltage. On the other hand, in the power circuit; pumps, circuit breakers, contactors, push buttons and high-power instruments are supported.

#### 4.3.1. Digital control circuit

Operating the open source Arduino software, an Arduino mega was programmed to operate the tasks necessary to take the signals from the sensing devices to the 4-channel relay and the Nextion HMI display. The entire code is found in annex C and Figure 41 illustrates the connections and probes to the equipment while is programmed. The Nextion display was also tested at this point both in real-time and simulated using the Nextion Editor software, this is shown in Figure 42. Moreover, the scheme for connections and network components testing and simulation were charted in Figure 43.

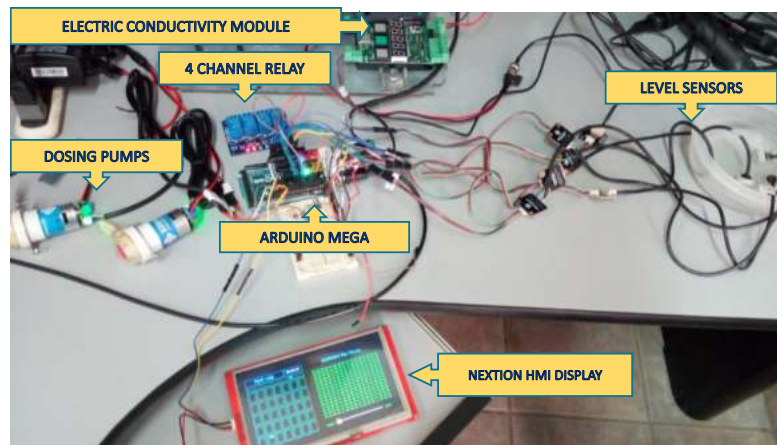


Figure 41.- Programming and trial of the devices for the control system



Figure 42.- Evaluating the Nextion display status in real-time (left) and virtually simulated (right).

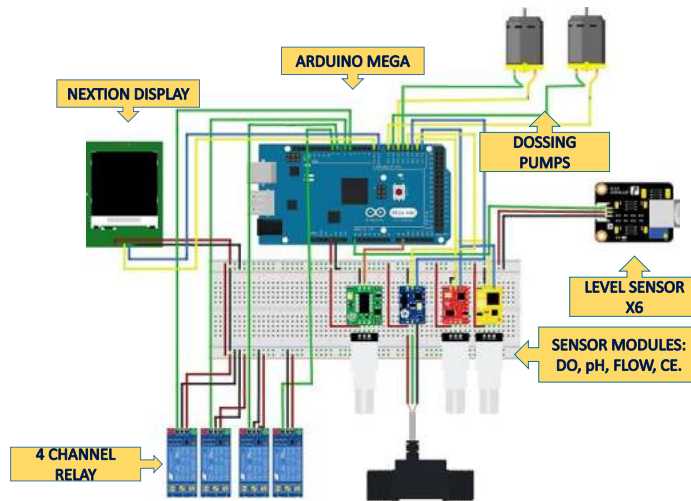
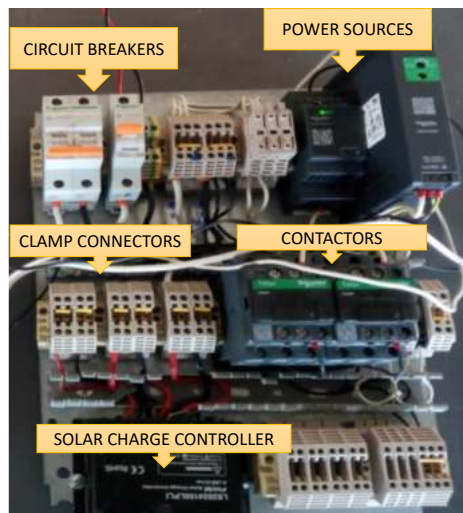


Figure 43.- Control circuit Scheme for the testing and probes of every digital control device.

#### 4.3.2. Power circuit

The power circuit involves power sources, screw clamp connectors, and contactors that support the stage to energize the electrical devices as pumps and valves among others. This stage has a start and a stop button for every pump and an emergency stop button to disable the entire power circuit if necessary. The power circuit is connected to the 120 VAC generated power in the PV system and feeds all the control-stage. The power circuit can be seen in the arrangement made for the system in the outdoor cabinet enclosure in Figure 44.



**Figure 44.- Power circuit array for the outdoor cabinet enclosure.**

Afterward, the entire control stage was arranged into two outdoor enclosure cabinets, one for the digital control circuit and the other for the power circuit. Where the HMI display was placed inside the one with the digital control and the stop/start buttons were arrayed on the external side of the power circuit enclosure door. The entire control stage array is observed in Figure 45.



**Figure 45.- Control circuit system outdoor cabinets arrangement.**

#### **4.3.3. Installation and assessment in an operational environment**

Finally, the installation (Figure 46) and assessment of the overall potabilizer system (Figure 47) were performed, running water coming from water supplied in the locality and testing out/ensuring the system's autonomy.

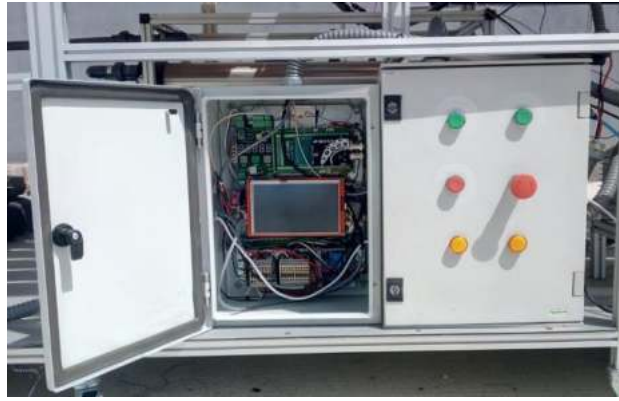


**Figure 46.- Control panel installation during the last section assembled on the structure**



**Figure 47.- Water potabilizer full operation as an evaluation for the whole process**

Initially, level sensors control the filling of the tanks by turning on/off the operation of the water pumps and the 3-way valves. Once the control system senses high-level water in the feedwater tank the RO pump started its operation and the conductivity sensor sends the reading to the HMI screen, where a conductivity value smaller to  $800 \mu\text{S}$  acts the 3-way valve and changes its stream going from recirculating water to flux to the reactor tank. The sensing device data at this point are shown in Figure 48 where a conductivity – time graph plots a decreasing conductivity timeline which corresponds to the RO membrane's demineralization performance. Recalling that the Mexican standard establishes the conductivity parameter for drinking water between  $600 - 800 \mu\text{S}/\text{cm}$  (marked in the dotted yellow line).

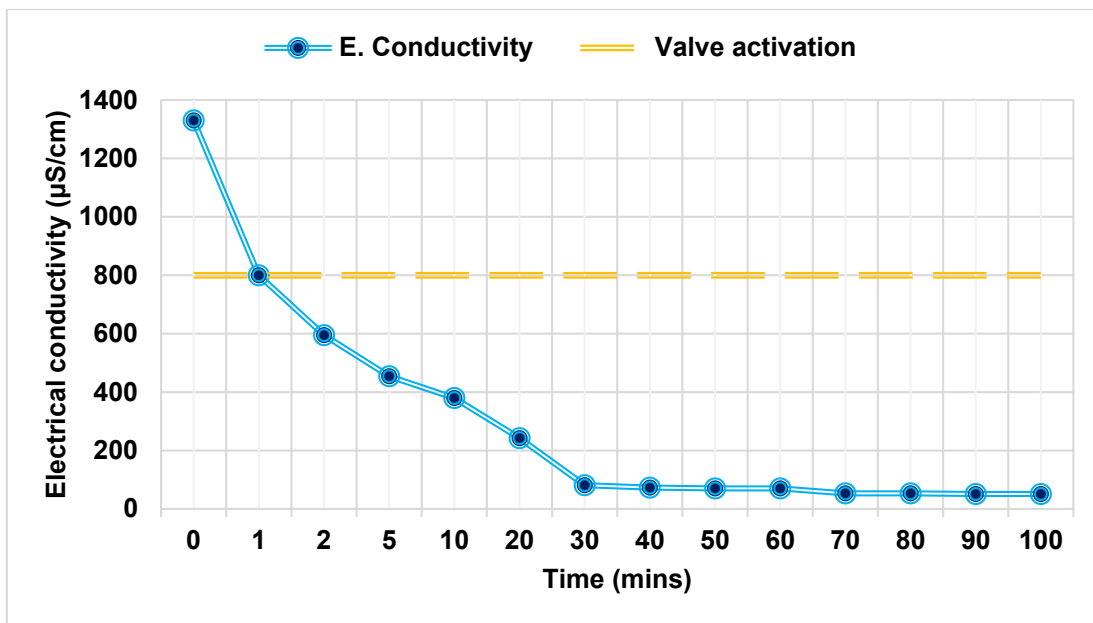


**Figure 48.- Electrical conductivity sensor performance during the evaluation of the potabilizer system**

As soon as the reactor tank was filled and the level sensors detected water, the reactor pump began to flow water through the reactor. There, the pH, temperature and DO sensors were measuring the water quality, and once the DO values were greater than 6 mg/L (according to the Mexican standards) the second 3-way valve acts streaming water from recirculating to send it towards the final tank. Figure 49 shows a DO concentration, pH and temperature versus time graph that plots the reactor stage performance according to the sensing devices' readings. As seen, the DO increase its value as a result of the decontamination performed by the reactor. Meanwhile, the pH decreased according to the demineralization that occurred in the RO desalination and the dissolved minerals remnants removal in the reactor. Finally, the temperature increase results from sun radiation exposure, but being low-concentration collectors, it does not increase considerably. Recalling that the DO Mexican standard for clean water establishes a range between 6-8 mg/L a dotted yellow line indicates the valve activation.



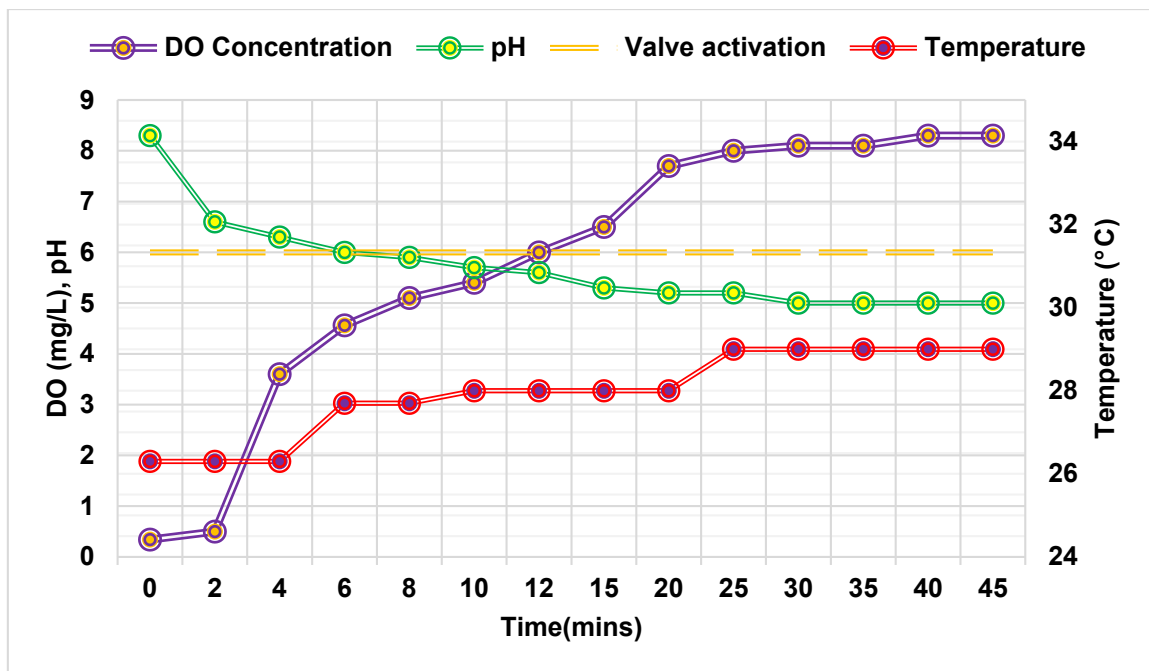


Figure 49.- DO, pH and Temperature sensors activity during the evaluation of the potabilizer system

All these tasks were performed by the control system, displayed on the HMI screen and powered by the stand-alone PV system. For a system overview, a video link of the potabilizer operation is attached, as well as the HMI screen.

[https://drive.google.com/drive/folders/1oYYKwltuvRULDXSr59b37oPmWOldU\\_zE?usp=sharing](https://drive.google.com/drive/folders/1oYYKwltuvRULDXSr59b37oPmWOldU_zE?usp=sharing)

#### 4.4. WATER COST PROTOTYPE EVALUATION

The system cost estimation was evaluated using the methodology proposed by Banat, F. & Jwaied [82] where production capacities and design characteristics were considered to obtain the cost of the water treatment system. More detailed data and specifications are found in [75] about the estimates and calculations.

The results of the cost evaluation are presented in table 15 and the economic hypotheses according to the methodology considerations proposed in the study are the following:

- The life expectancy of the plant is 20 years.
- Operation and maintenance costs are estimated at 20% of the plant's annual payment. Approximately 13% is related to maintenance.
- The annual rate of equipment replacement is 10% according to the methodology.
- 7% interest rate, when financing is required.

**Table 15.- Cost evaluation using the methodology proposed by Banat, F. & Jwaied**

Treated water unit costing	Cost (US\$/m <sup>3</sup> )
Total capital investment	3.26-1.63
Element replacement	0.4-0.2
Annual cost operation	0.64-0.32
<b>Final unit cost</b>	<b>4-2</b>

Since the potabilizer is a multistage prototype assessed preliminarily to an operational environment, a real cost/production water estimation requires an update process beyond the project objectives and scope. However, knowing the cost of 2-4 \$/m<sup>3</sup> obtained in table 15, a preliminary comparison with the fabricated system (green row) in table 16 was developed, where an economic evaluation review of membrane distillation systems and prototypes was listed according to their source energy, capacity, feedwater and costs. According to the published literature related to membrane distillation systems, the treated water cost/product corresponds to a range not greater than these water treatment technologies, which could appoint it accessible to its production.

**Table 16.- Economic evaluation studies of membrane distillation (MD) and water costs for different water treatment factors (capacity, feedwater, source energy) [83].**

Capacity (m <sup>3</sup> /day)	Feedwater	Energy factors	Costs (\$/m <sup>3</sup> )
<b>1</b>	<b>Raw water</b>	<b>Solar powered</b>	<b>2-4</b>
20	Seawater	Solar powered	16.42
24,000	Seawater	Heat recovery	1.07
24,000	Seawater	No heat recovery	1.12
30,000	Seawater	n.a	0.56-1.57
n.a*	Seawater	Solar powered	13.68-16.42
n.a	Seawater	Geothermal	11.86
n.a	Seawater	Waste heat	1-1.37
n.a	Seawater	Solar powered	16.70
n.a	Seawater	Waste heat	4.84
n.a	Seawater	Solar powered	14.6
n.a	Seawater	Waste heat	1.82
10	Wastewater	Waste heat	8.21-8.94
1000	Wastewater	Waste heat	4.01-4.38

\*n.a: not available



## CONCLUSIONS

---

A water potabilizer prototype was designed, fabricated and assessed with a production capacity of 1 m<sup>3</sup>/day was built. This water treatment system is electrically supplied by a solar PV stage, providing the necessary energy to the entire control stage and electric devices. Yielding thus autonomy to the system, due to its capacity to run and operate the whole process without requiring human oversight. All the water potabilizer stages were completed and through this, an important generation of technological engineering has been obtained in the design and construction of these water treatment systems applied simultaneously (henceforward) with photocatalytic processes, completely attached to the main objective to fulfill the obtaining of a quality clean water in accordance to the Mexican standards.

In this regard, a control stage with communication between an Arduino Mega board - HMI display – power circuit was assembled, where the Arduino board receives the signals (digital and analogous) for monitoring the water potabilizer and sends signals programmed for the operating of the whole system devices. Additionally, the system automation displays the status of every watered cycle on the HMI screen. Furthermore, a control system evaluation was performed through the charting of the CE, DO, pH and temperature versus time, showing the operation of the whole coupled stages. Achieving hence, the required water quality (according to the sensing devices behaved) and the full prototype stages automation.

On the other hand, during the development of the photocatalytic reactor, the irradiance collection capability of the CPC collectors in the system was improved through a novel methodology using a 3D model printed it was possible to avoid traditional methods (hydraulic press, stamping, etc.), which may produce damage to the aluminum sheet and inaccuracies in the fabricated curvature decreasing the optical efficiency of the collector.

A manuscript was generated, submitted and published (DOI:10.5937/jaes0-37918) which involves an optical assessment of the 3D printed mold technique by a combination of photogrammetry and Monte Carlo ray tracing model analysis, where two techniques to fabricate CPC collectors were compared; the conventionally manufactured CPC (CM-

CPC) employing styrofoam with a 3D printed mold (3DM-CPC) to ideally designed 1-sun collector.

The photogrammetry results yielded for the 3DM-CPC and the CM-CPC showed a MAE of 1.2 and 3.19, respectively. Whereas, to validate the collector profile evaluation a ray tracing study was made, where a seasonal sun position (4-days) analysis shows that in every day assessed the 3DM-CPC collector demonstrates a better performance over the CM-CPC, despite the particular case of the winter solstice where low contribution in solar irradiance was obtained the 3DM-CPC exposed better performance in the evaluation.

3DM-CPC obtain 95% against the CM-CPC with the 82% of efficiency on autumnal equinox day e.g. The assesses validate the effectiveness of the fabrication technique. This assessment infers a determinant factor in solar collectors' optical performance, especially when low-power concentrations are used (e.g. for chemical processes) resulting from the limited UV solar radiation available. Furthermore, the manufacturing techniques are corroborated by analyzing its operation on a simulated Thermal Plant. The advantage found was around 1,631 kWh ( $\approx 9.4\%$ ) performed annually with the proposed CPC fabricated.

The above helped to publish the relevant results of this methodology in an international congress and the publication of the research article in an indexed journal. Besides, hereafter the prototype may expand the research line into the photocatalytic reactor through the degradation of the pollutant in the treated water. Furthermore, it may have continuity of the study and the assessment of the CPC collector's performance and efficiency in situ using dyes, pesticides, or microorganisms to name a few.

## RECOMMENDATIONS

---

It is important to specify some advice to improve and adjust the functions of the potabilizer stages. In this case, these recommendations are listed below according to the stage. And to conclude, the contribution of this project to the expertise generated is mentioned.

RO stage: is necessary to complement this system with a pressure sensor device to determine the increasing or decreasing pressure coming from the pump. Adding this device, it is possible to graph and obtain data to implement either adjustments or replacements in the stage.

Reactor stage: in this stage, it was contemplated an inline refractometer sensing device. Assessing in this way the microorganism population, giving a finer measurement and a greater consistency to the water cycle. Furthermore, evaluations using supported  $TiO_2$  catalyzer is essential to asses this stage and its degradation competency.

Stand-alone PV: To protect and avoid accidents due to the high tension coming from the power supplied, this stage must have a waterproof outdoor case. Besides, when wiring this system, it is important to be very careful using protective equipment and/or ask an expert for help since the battery bank installation may generate short circuits by grounding the system with some part of the structure by mistake.

Short-term planning: This system will be an innovative prototype, unique in Mexico, moreover, an autonomous system that does not require human oversight or specialized knowledge running without any other type of energy than solar energy. The prototype will be useful to assess and conclude scaling factors suitable for the rural area necessity, especially those localities where hydric, monetary, sanitary, and human conditions are unfavorable.

Long-term planning: A proposal to manufacture prototypes from this design to be installed in rural communities of the country will be made, thereby impacting the life quality of the population in need. In this manner, the illnesses derived from drinking polluted water will be drastically reduced, to fulfill the Mexican standards for clean water. Thus, demonstrating that a photocatalytic water purifier constitutes a viable alternative, in the implementation of decentralized alternative energies context in Mexico.

Finally, this project has contributed to generating technology transfer mechanisms such as:

- 3D model prototype: Design and sizing of the autonomous water treatment system (innovative)
- CPC: Manufacturing technique and evaluations that generated 1 article and congress meetings
- Autonomy: a control system fully automated and self-sustainable powered by solar energy
- Scaling: study according to the requirement
- Linkage: Dealings with public, private, and government companies to commercialize this technology and seek patents

## REFERENCES

---

1. "2.1 billion people lack safe drinking water at home, more than twice as many lack safe sanitation," <https://www.who.int/en/news-room/detail/12-07-2017-2-1-billion-people-lack-safe-drinking-water-at-home-more-than-twice-as-many-lack-safe-sanitation>.
2. "SDG Goal 6: Clean Water and Sanitation - UNICEF DATA," <https://data.unicef.org/sdgs/goal-6-clean-water-sanitation/>.
3. WHO/UNICEF, "Progress on Drinking Water, Sanitation and Hygiene - Joint Monitoring Programme 2017 Update and SDG Baselines," World Heal. Organ. 66 (2017).
4. E. Funari, T. Kistemann, S. Herbst, and a Rechenburg, "Technical guidance on water-related disease surveillance," World Heal. Organ. Eur. 1–139 (2011).
5. C. Nacional and D. A. México, "Estadísticas DEL AGUA EN," (2017).
6. A. M. F. D. E. L. O. S. Romo, "7. problemática 7.1. entorno natural. clima.," 219–234 (n.d.).
7. B. No, "Investigador de la UAA indaga sobre el problema de la fluorización del agua en el estado," (n.d.).
8. COMISIÓN NACIONAL DE AGUA, *Diseño De Plantas Potabilizadoras Tipo De Tecnología Simplificada* (2007).
9. W. Q. Betancourt and J. B. Rose, "Drinking water treatment processes for removal of Cryptosporidium and Giardia," Vet. Parasitol. **126**, 219–234 (2004).
10. M. Herraiz-Carboné, S. Cotillas, E. Lacasa, C. Sainz de Baranda, E. Riquelme, P. Cañizares, M. A. Rodrigo, and C. Sáez, "A review on disinfection technologies for controlling the antibiotic resistance spread," Sci. Total Environ. **797**, 149150 (2021).
11. "¿Qué es la ósmosis inversa y cómo funciona? - Pure Aqua, Inc.," <https://es.pureaqua.com/que-es-la-osmosis-inversa/>.

12. D. Pepper, "Basics of Reverse Osmosis.," Symp. Pap. - Inst. Chem. Eng. North West. Branch 1–16 (1980).
13. "Puretec Industrial Water | What is Reverse Osmosis?," <https://puretecwater.com/reverse-osmosis/what-is-reverse-osmosis>.
14. A. Sagle and B. Freeman, "Fundamentals of membranes for water treatment," *Futur. Desalin. Texas* 1–17 (2004).
15. "Membrane Technology: A Break Through in Water Treatment – WCP Online," <https://wcponline.com/2009/02/10/membrane-technology-break-water-treatment/>.
16. M. S. Benavides and M. M. Miranda, *Desalación de Agua de Mar Mediante Sistema Osmosis Inversa y Energía Fotovoltaica Para Provisión de Agua Potable En Isla Damas, Región de Coquimbo* (n.d.).
17. "Solar Overview – Ruaha Energy," <https://ruahaenergy.com/solar/solar-overview/>.
18. S. A. Kalogirou, "Chapter 3 - Solar Energy Collectors," *Sol. Energy Eng.* (Second Ed. 125–220 (2014)).
19. "On-Grid and Off-Grid system | NT Energy Solutions," <http://www.nt-energysolutions.com/en/Article/Detail/101927>.
20. V. P. Katekar and S. S. Deshmukh, "A review on research trends in solar still designs for domestic and industrial applications," *J. Clean. Prod.* **257**, 120544 (2020).
21. J. Blanco-Galvez, P. Fernández-Ibáñez, and S. Malato-Rodríguez, "Solar photo catalytic detoxification and disinfection of water: Recent overview," *J. Sol. Energy Eng. Trans. ASME* **129**, 4–15 (2007).
22. "Advanced Oxidation Processes for Wastewater Treatment | SUEZ," <https://www.watertechnologies.com/products/disinfection-oxidation/aop-systems>.
23. S. Malato, J. Blanco, A. Vidal, and C. Richter, "Photocatalysis with solar energy at a pilot-plant scale: An overview," *Appl. Catal. B Environ.* **37**, 1–15 (2002).
24. M. C. Nevárez-martínez, P. J. Espinoza-montero, F. J. Quiroz-chávez, and B. Ohtani, "Fotocatálisis : inicio , actualidad y perspectivas a través del TiO 2," **12**,

45–59 (2017).

25. Y. Abdel-Maksoud, E. Imam, and A. Ramadan, "TiO<sub>2</sub> solar photocatalytic reactor systems: Selection of reactor design for scale-up and commercialization—analytical review," *Catalysts* **6**, (2016).
26. H. N. C. Dharma, J. Jaafar, N. Widiastuti, H. Matsuyama, S. Rajabsadeh, M. H. D. Othman, M. A. Rahman, N. N. M. Jafri, N. S. Suhaimin, A. M. Nasir, and N. H. Alias, "A Review of Titanium Dioxide (TiO<sub>2</sub>)-Based Photocatalyst for Oilfield-Produced Water Treatment," *Membr.* 2022, Vol. 12, Page 345 **12**, 345 (2022).
27. I. Di Somma, "Applied Catalysis B : Environmental Solar photocatalysis : Materials , reactors , some commercial , and pre-industrialized applications . A comprehensive approach," **171**, 90–123 (2015).
28. A. Echevarría, "Diseño De Un Colector Cilindro Parabólico Compuesto Con Aplicación Para El Calentamiento De Agua," 27–43 (2011).
29. "Tecnologías solares para el tratamiento, reutilización de aguas residuales urbanas y valorización de recursos extraídos | FuturENVIRO - Revista técnica bilingüe de medio ambiente," <http://futurenviro.es/tecnologias-solares-para-el-tratamiento-reutilizacion-de-aguas-residuales-urbanas-y-valorizacion-de-recursos-extraidos/>.
30. M. Tian, Y. Su, H. Zheng, G. Pei, G. Li, and S. Riffat, "A review on the recent research progress in the compound parabolic concentrator (CPC) for solar energy applications," *Renew. Sustain. Energy Rev.* **82**, 1272–1296 (2018).
31. M. Antonelli, A. Baccioli, M. Francesconi, U. Desideri, and L. Martorano, "Electrical production of a small size Concentrated Solar Power plant with compound parabolic collectors," *Renew. Energy* **83**, 1110–1118 (2015).
32. D. Tiwari, A. F. Sherwani, D. Atheaya, and A. Arora, "Energy and exergy analysis of solar driven recuperated organic Rankine cycle using glazed reverse absorber conventional compound parabolic concentrator (GRACCP) system," *Sol. Energy* **155**, 1431–1442 (2017).
33. M. Elashmawy, "An experimental investigation of a parabolic concentrator solar

- tracking system integrated with a tubular solar still," *Desalination* **411**, 1–8 (2017).
34. X. Xue, H. Zheng, Y. Su, and H. Kang, "Study of a novel sunlight concentrating and optical fibre guiding system," *Sol. Energy* **85**, 1364–1370 (2011).
  35. J. B. Gálvez, S. M. Rodríguez, C. A. E. Gasca, R. Erick, and S. Gelover, "Purificación de aguas por fotocatalisis heterogénea: estado del arte," 51–76 (1985).
  36. J. B. Gálvez, "El reactor solar fotocatalítico : estado del arte," 277–302 (n.d.).
  37. M. A. Fendrich, A. Quaranta, M. Orlandi, M. Bettonte, and A. Miotello, "Solar concentration for wastewaters remediation: A review of materials and technologies," *Appl. Sci.* **9**, (2018).
  38. I. Salgado-Tránsito, A. E. Jiménez-González, M. L. Ramón-García, C. A. Pineda-Arellano, and C. A. Estrada-Gasca, "Design of a novel CPC collector for the photodegradation of carbaryl pesticides as a function of the solar concentration ratio," *Sol. Energy* **115**, 537–551 (2015).
  39. H. P. Baum and J. M. Gordon, "Geometric characteristics of ideal nonimaging (CPC) solar collectors with cylindrical absorber," *Sol. Energy* **33**, 455–458 (1984).
  40. M. Chafie, M. F. Ben Aissa, S. Bouadila, M. Balghouthi, A. Farhat, and A. Guizani, "Experimental investigation of parabolic trough collector system under Tunisian climate: Design, manufacturing and performance assessment," *Appl. Therm. Eng.* (2016).
  41. P. Forman, S. Müller, M. A. Ahrens, J. Schnell, P. Mark, R. Höffer, K. Hennecke, and J. Krüger, "Light concrete shells for parabolic trough collectors - Conceptual design, prototype and proof of accuracy," *Sol. Energy* **111**, 364–377 (2015).
  42. S. Meiser, S. Schneider, E. Lüpfer, B. Schiricke, and R. Pitz-Paal, "Evaluation and Assessment of Gravity Load on Mirror Shape of Parabolic Trough Solar Collectors," in *Energy Procedia* (2015).
  43. S. Meiser, S. Schneider, E. Lüpfer, B. Schiricke, and R. Pitz-Paal, "Evaluation and assessment of gravity load on mirror shape and focusing quality of parabolic



- through solar mirrors using finite-element analysis," *Appl. Energy* (2017).
44. M. Balghouthi, A. B. H. Ali, S. E. Trabelsi, and A. Guizani, "Optical and thermal evaluations of a medium temperature parabolic trough solar collector used in a cooling installation," *Energy Convers. Manag.* (2014).
  45. T. Osório, P. Horta, and M. Collares-Pereira, "Method for customized design of a quasi-stationary CPC-type solar collector to minimize the energy cost," *Renew. Energy* **133**, 1086–1098 (2019).
  46. A. S. Jadhav, A. S. Gudekar, R. G. Patil, D. M. Kale, S. V. Panse, and J. B. Joshi, "Performance analysis of a novel and cost effective CPC system," *Energy Convers. Manag.* **66**, 56–65 (2013).
  47. M. El Ydrissi, H. Ghennioui, E. G. Bennouna, and A. Farid, "Geometric, optical and thermal analysis for solar parabolic trough concentrator efficiency improvement using the photogrammetry technique under semi-arid climate," *Energy Procedia* **157**, 1050–1060 (2019).
  48. S. Skouri, A. Ben Haj Ali, S. Bouadila, and S. Ben Nasrallah, "Optical qualification of a solar parabolic concentrator using photogrammetry technique," *Energy* **90**, 403–416 (2015).
  49. H. Zhu, Z. Wang, H. Wang, and Q. Yu, "Shape Measurement and Reconstruction of Solar Concentrator Based on Two-dimensional Phase Shift Method," *Energy Procedia* **69**, 1921–1927 (2015).
  50. S. Meiser, E. Lüpfert, B. Schiricke, and R. Pitz-Paal, "Analysis of parabolic trough concentrator mirror shape accuracy in different measurement setups," *Energy Procedia* **49**, 2135–2144 (2014).
  51. M. I. Peña-Cruz, C. A. Arancibia-Bulnes, A. Monreal Vidal, and M. Sánchez González, "Improving parabolic trough mirror module qualification by FOCuS tool," *J. Renew. Sustain. Energy* **6**, (2014).
  52. C. Weber, S. Ulmer, and H. Koch, "Enhancements in high-resolution slope deviation measurement of solar concentrator mirrors," *Energy Procedia* **49**, 2231–2240 (2014).

53. S. A. Waghmare and N. P. Gulhane, "Optical evaluation of compound parabolic collector with low acceptance angle," *Optik (Stuttg)*. **149**, 359–371 (2017).
54. B. Schirricke, R. Pitz-Paal, E. Lüpfert, K. Pottler, M. Pfänder, K. J. Riffelmann, and A. Neumann, "Experimental verification of optical modeling of parabolic trough collectors by flux measurement," *J. Sol. Energy Eng. Trans. ASME* **131**, 0110041–0110046 (2009).
55. F. Lara, J. Cerezo, A. Acuña, A. González-Ángeles, N. Velázquez, A. Ruelas, and R. López-Zavala, "Design, optimization and comparative study of a solar CPC with a fully illuminated tubular receiver and a fin inverted V-shaped receiver," *Appl. Therm. Eng.* **184**, 116141 (2021).
56. J. G. Carrillo, M. Peña-Cruz, M. Terrón-Hernández, and L. Valentin, "Low Cost High-Accuracy CPC System - A Manufacturing Methodology," *J. Sol. Energy Eng.* 1–13 (2020).
57. "What Are the Main Water Quality Indicators and Parameters?," <https://sinay.ai/en/what-are-the-main-indicators-of-water-quality/>.
58. "Measuring Conductivity of RO Water | Reverse Osmosis | Sensorex," <https://sensorex.com/blog/2017/07/12/conductivity-monitoring-reverse-osmosis/>.
59. H. Estado and D. E. L. Arte, "Purificación De Aguas Por Fotocatálisis," (2016).
60. A. Acra, Y. Karahagopian, Z. Raffoul, and R. Dajani, "Disinfection of Oral Rehydration Solutions By Sunlight," *Lancet* **316**, 1257–1258 (1980).
61. T. Matsunaga, R. Tomoda, T. Nakajima, and H. Wake, "Photoelectrochemical sterilization of microbial cells by semiconductor powders," *FEMS Microbiol. Lett.* **29**, 211–214 (1985).
62. S. Dong, J. Feng, M. Fan, Y. Pi, L. Hu, and X. Han, "Recent developments in heterogeneous photocatalytic water treatment using visible light- responsive photocatalysts : a review," *RSC Adv.* **5**, 14610–14630 (2015).
63. A. O. Ibhaddon and P. Fitzpatrick, "Heterogeneous photocatalysis: Recent advances and applications," *Catalysts* **3**, 189–218 (2013).

64. J. A. Herrera Melián, J. M. Doña Rodríguez, A. Viera Suárez, E. Tello Rendón, C. Valdés Do Campo, J. Arana, and J. Pérez Peña, "The photocatalytic disinfection of urban waste waters," *Chemosphere* **41**, 323–327 (2000).
65. J. C. Crittenden, R. P. S. Suri, D. L. Perram, and D. W. Hand, "Decontamination of water using adsorption and photocatalysis," *Water Res.* **31**, 411–418 (1997).
66. P. A. S. S. Marques, M. F. Rosa, F. Mendes, M. Collares Pereira, J. Blanco, and S. Malato, "Wastewater detoxification of organic and inorganic toxic compounds with solar collectors," *Desalination* **108**, 213–220 (1997).
67. H. O. Neal, S. Garcia-segura, K. Hristovski, and P. Westerhoff, "Science of the Total Environment Compact light-emitting diode optical fiber immobilized TiO<sub>2</sub> reactor for photocatalytic water treatment," *Sci. Total Environ.* **613–614**, 1331–1338 (2018).
68. H. Yu, L. Song, Y. Hao, N. Lu, X. Quan, S. Chen, Y. Zhang, and Y. Feng, "Fabrication of pilot-scale photocatalytic disinfection device by installing TiO<sub>2</sub> coated helical support into UV annular reactor for strengthening sterilization," **283**, 1506–1513 (2016).
69. H. C. J. Casalins-blanco, "353549828006.Pdf," (2016).
70. O. Sacco, V. Vaiano, L. Rizzo, and D. Sannino, "Photocatalytic activity of a visible light active structured photocatalyst developed for municipal wastewater treatment," *J. Clean. Prod.* **175**, 38–49 (2018).
71. M. Terrón-Hernández, M. I. Peña-Cruz, J. G. Carrillo, U. Diego-Ayala, and V. Flores, "Solar Ray Tracing Analysis to Determine Energy Availability in a CPC Designed for Use as a Residential Water Heater," (n.d.).
72. V. Augugliaro, E. García-López, V. Loddo, S. Malato-Rodríguez, I. Maldonado, G. Marcì, R. Molinari, and L. Palmisano, "Degradation of lincomycin in aqueous medium: Coupling of solar photocatalysis and membrane separation," *Sol. Energy* **79**, 402–408 (2005).
73. M. I. Peña-Cruz, P. J. Valades-Pelayo, C. A. Arancibia-Bulnes, C. A. Pineda-Arellano, I. Salgado-Tránsito, and F. Martell-Chavez, "Annual optical performance

of a solar CPC photoreactor with multiple catalyst support configurations by a multiscale model," *Int. J. Photoenergy* **2018**, (2018).

74. M. Tian, Y. Su, H. Zheng, G. Pei, G. Li, and S. Riffat, "A review on the recent research progress in the compound parabolic concentrator (CPC) for solar energy applications," *Renew. Sustain. Energy Rev.* **82**, 1272–1296 (2018).
75. O. Gómez, "Desalinización De Agua Para Aplicaciones De Potabilización Mediante El Desarrollo De Tecnología Solar Sustentable," 12–50 (2018).
76. A. Khaligh and O. C. Onar, "Energy sources," *Power Electron. Handb.* 1289–1330 (2011).
77. G. DE CANARIAS, C. Y. N. T. CONSEJERIA DE INDUSTRIA, V. D. I. Y. N. TECNOLOGÍAS, and D. G. D. I. Y. ENERGÍA, "Guia TéCnica De Aplicación Para Instalaciones De Energías Renovables Instalaciones Fotovoltaicas," 55 (2010).
78. J. B. Gálvez, "El reactor solar fotocatalítico : estado del arte," *Sol. safe water* 277–302 (2005).
79. "2-Estudio comparativo de las tecnologías existentes para el tratamiento... | Download Scientific Diagram," [https://www.researchgate.net/figure/Estudio-comparativo-de-las-tecnologias-existentes-para-el-tratamiento-de-aguas-en\\_fig2\\_41223550](https://www.researchgate.net/figure/Estudio-comparativo-de-las-tecnologias-existentes-para-el-tratamiento-de-aguas-en_fig2_41223550).
80. P. R. Martínez-Manuel, L. M. Valentín-Coronado, I. Salgado-Transito, M. I. Peña-Cruz, F. Martell-Chávez, J. G. Carrillo-Baeza, and C. A. Pineda-Arellano, "OPTICAL EVALUATION OF 3D PRINTED CPC BY COUPLING PHOTOGRAMMETRY AND RAY TRACING ANALYSIS," *J. Appl. Eng. Sci.* 1–11 (2022).
81. P. King, C. Sansom, and P. Comley, "Photogrammetry for concentrating solar collector form measurement, validated using a coordinate measuring machine," *Sustain.* **12**, 1–20 (2020).
82. F. Banat and N. Jwaied, "Economic evaluation of desalination by small-scale autonomous solar-powered membrane distillation units," *Desalination* **220**, 566–573 (2008).

83. D. Amaya-Vías and J. A. López-Ramírez, "Techno-economic assessment of air and water gap membrane distillation for seawater desalination under different heat source scenarios," *Water (Switzerland)* **11**, (2019).

## ANNEX A

496

		ID DE LA MUESTRA	
ANALITO	UNIDADES	1	Método
Cloruros	mg/L	268.05	Volumetría
Dureza total	mg/L	35.44	Volumetría
pH		7.02	Potenciometría
Conductividad		259.48	Potenciometría
Nitrógeno Amoniacal	mg/L	0.13	Potenciometría
solidos disueltos totales	mg/L	1.50	Gravimetría
Sulfatos	mg/L	66.94	ICP OES
Alcalinidad Total (mg CaCO <sub>3</sub> /L)	mg/L	7.00	Volumetría
Cd	mg/L	<0.01	ICP OES
As	mg/L	0.11	ICP OES
Pb	mg/L	<0.01	ICP OES
Sn	mg/L	<0.01	ICP OES
Cu	mg/L	<0.01	ICP OES
Zn	mg/L	0.02	ICP OES
Hg	mg/L	<0.001	ICP OES
P	mg/L	0.10	ICP OES
Na	mg/L	12.54	ICP OES
K	mg/L	15.31	ICP OES
Ca	mg/L	9.31	ICP OES
Mn	mg/L	0.02	ICP OES
Mg	mg/L	2.90	ICP OES
B	mg/L	<0.01	ICP OES
Bicarbonato (HCO <sub>3</sub> <sup>-</sup> )	mg/L	6.86	Volumetría
Carbonatos (CO <sub>3</sub> <sup>-2</sup> )	mg/L	Ausencia	Volumetría

495

		ID DE LA MUESTRA	
ANALITO	UNIDADES	36	Método
Cloruros	mg/L	80.84	Volumetría
Dureza total	mg/L	175.03	Volumetría
pH		8.08	Potenciometría
Conductividad		283.32	Potenciometría
Nitrógeno Amoniacal	mg/L	0.09	Potenciometría
solidos disueltos totales	mg/L	1.20	Gravimetría
Sulfatos	mg/L	36.92	ICP OES
Alcalinidad Total (mg CaCO <sub>3</sub> /L)	mg/L	17.00	Volumetría
Cd	mg/L	<0.01	ICP OES
As	mg/L	0.03	ICP OES

Pb	mg/L	<0.01	ICP OES
Sn	mg/L	<0.01	ICP OES
Cu	mg/L	<0.01	ICP OES
Zn	mg/L	<0.01	ICP OES
Hg	mg/L	<0.001	ICP OES
P	mg/L	<0.05	ICP OES
Na	mg/L	54.58	ICP OES
K	mg/L	22.54	ICP OES
Ca	mg/L	60.63	ICP OES
Mn	mg/L	<0.01	ICP OES
Mg	mg/L	5.59	ICP OES
B	mg/L	<0.01	ICP OES
Bicarbonato (HCO <sub>3</sub> <sup>-</sup> )	mg/L	16.66	Volumetría
Carbonatos (CO <sub>3</sub> <sup>-2</sup> )	mg/L	Ausencia	Volumetría

494

		ID DE LA MUESTRA	
ANALITO	UNIDADES	107	Método
Cloruros	mg/L	46.80	Volumetría
Dureza total	mg/L	251.31	Volumetría
pH		7.59	Potenciometría
Conductividad		331.92	Potenciometría
Nitrógeno Amoniacal	mg/L	0.10	Potenciometría
solidos disueltos totales	mg/L	0.90	Gravimetría
Sulfatos	mg/L	58.72	ICP OES
Alcalinidad Total (mg CaCO <sub>3</sub> /L)	mg/L	14.00	Volumetría
Cd	mg/L	<0.01	ICP OES
As	mg/L	0.03	ICP OES
Pb	mg/L	<0.01	ICP OES
Sn	mg/L	<0.01	ICP OES
Cu	mg/L	<0.01	ICP OES
Zn	mg/L	<0.01	ICP OES
Hg	mg/L	<0.001	ICP OES
P	mg/L	<0.05	ICP OES
Na	mg/L	140.24	ICP OES
K	mg/L	23.57	ICP OES
Ca	mg/L	92.62	ICP OES
Mn	mg/L	<0.01	ICP OES
Mg	mg/L	4.71	ICP OES
B	mg/L	0.24	ICP OES
Bicarbonato (HCO <sub>3</sub> <sup>-</sup> )	mg/L	39.20	Volumetría
Carbonatos (CO <sub>3</sub> <sup>-2</sup> )	mg/L	Ausencia	Volumetría

493

		ID DE LA MUESTRA	
ANALITO	UNIDADES	126	Método

Cloruros	mg/L	49.65	Volumetría
Dureza total	mg/L	99.49	Volumetría
pH		8.16	Potenciometría
Conductividad		274.05	Potenciometría
Nitrógeno Amoniacal	mg/L	0.09	Potenciometría
solidos disueltos totales	mg/L	0.10	Gravimetría
Sulfatos	mg/L	36.03	ICP OES
Alcalinidad Total (mg CaCO <sub>3</sub> /L)	mg/L	40.00	Volumetría
Cd	mg/L	<0.01	ICP OES
As	mg/L	0.02	ICP OES
Pb	mg/L	<0.01	ICP OES
Sn	mg/L	<0.01	ICP OES
Cu	mg/L	<0.01	ICP OES
Zn	mg/L	<0.01	ICP OES
Hg	mg/L	<0.001	ICP OES
P	mg/L	<0.05	ICP OES
Na	mg/L	38.24	ICP OES
K	mg/L	7.87	ICP OES
Ca	mg/L	34.90	ICP OES
Mn	mg/L	<0.01	ICP OES
Mg	mg/L	2.92	ICP OES
B	mg/L	<0.01	ICP OES
Bicarbonato (HCO <sub>3</sub> <sup>-</sup> )	mg/L	13.72	Volumetría
Carbonatos (CO <sub>3</sub> <sup>-2</sup> )	mg/L	Ausencia	Volumetría



ilpp publishing

## Journal of Applied Engineering Science

---

CENTRO DE INVESTIGACIONES  
EN OPTICA, A.C. LOMA DEL  
BOSQUE NO. 115, LOMAS DEL  
CAMPESTRE C.P. 37150,  
LEON, GTO. MÉXIC

Belgrade, 22.08.2022.

Subject: Confirmation of a positive review and final decision of the JAES Editorial Board

Dear Sirs,

This is to inform you that the article on the following topic: "Optical evaluation of 3D printed CPC by coupling photogrammetry and ray tracing analysis", ID 37918, and following authors: Carlos A. Pineda-Arellano, Pedro R. Martínez-Manuel, Luis M. Valentín-Coronado, Iván Salgado-Transito, Manuel I. Peña-Cruz, Fernando Martell-Chávez, J. Gonzalo Carrillo-Baeza was positively reviewed and accepted by the Editorial Board for publication in the Journal of Applied Engineering Science (JAES). The article will be published in the December issue of the JAES in 2022, Volume 20 Number 4.

JAES provides indexing of the paper in title through Scopus, DOAJ, Google Scholar, Scindeks, Kobson, ROAD.

With best regards  
Editor in Chief



Prof. Dr Gradinir Danon



---

[www.engineeringscience.rs](http://www.engineeringscience.rs)

## OPTICAL EVALUATION OF 3D PRINTED CPC BY COUPLING PHOTOGRAMMETRY AND RAY TRACING ANALYSIS

Pedro R. Martínez-Manuel<sup>1</sup>, Luis M. Valentín-Coronado<sup>2</sup>, Iván Salgado-Transito<sup>2</sup>, Manuel I. Peña-Cruz<sup>2</sup>, Fernando Martell-Chávez<sup>3</sup>, J. Gonzalo Carrillo-Baeza<sup>4</sup>, Carlos A. Pineda-Arellano<sup>2\*</sup>

<sup>1</sup> Posgrado Interinstitucional de Ciencia y Tecnología – Centro de Investigaciones en Óptica, A.C. Unidad Aguascalientes, Prol. Constitución 607 Fracc. Reserva Loma Bonita, CP 20200 Aguascalientes, Aguascalientes, México

<sup>2</sup> CONACYT – Centro de Investigaciones en Óptica, A.C. Unidad Aguascalientes, Prol. Constitución 607, Fracc. Reserva Loma Bonita, CP 20200 Aguascalientes, Aguascalientes, México

<sup>3</sup> Centro de Investigaciones en Óptica, A.C. Unidad Aguascalientes, Prol. Constitución 607, Fracc. Reserva Loma Bonita, CP 20200 Aguascalientes, Aguascalientes, México

<sup>4</sup> Centro de Investigación Científica de Yucatán, Unidad de Materiales, Calle 43 No. 130 x 32 y 34, Chuburná de Hidalgo, CP 97205 Mérida, Yucatán, México

\* capia@cio.mx

Manufacturing methods of CPC collectors, regardless the application, have not undergone significant modifications in recent years; the main manufacturing methods are hydraulic press stamping and some other machining methods, which generate errors in geometric curvature and damage to the high-reflectivity film coating, reducing the overall optical efficiency of the CPC. In this work, we propose a method for the fabrication of cylindrical CPCs (widely used in water-heating, disinfection, and wastewater treatment applications), which comprises the use of a 3D printed mold complemented with a structural styrofoam molding. The proposed method presents the advantage of improving the quality of the CPC profile with less damage on the surface of the high reflectivity coating and with a reduction in the quantity of deformations because of its machining processes. To evaluate the effectiveness of the presented method, an experimental-simulation test was carried out based on a photogrammetric technique combined with a Ray tracing Monte Carlo method. The test procedure compared the CPC manufactured with the proposed method (called 3DM-CPC) versus one manufactured by a conventional machining technique (referred as CM-CPC). The results obtained show a geometrical mean error value of 1.2 mm for the 3DM-CPC compared to 3.19 mm for the CM-CPC. Optical assessment by ray tracing showed a relative efficiency of 95% for the 3DM-CPC versus 82% of the CM-CPC, both of them compared to the theoretical ideal geometry of a 2D-1 Sun CPC. The benefit could be estimated in a simulation to be 9.4% in the annual performance of a 1000 L CPC thermal energy solar plant.

**Keywords:** CPC manufacturing, 3D printed molds, photogrammetric technique, photocatalytic reactor, solar concentrator

### 1 INTRODUCTION

Compound Parabolic Concentrators (CPC's) are non-image concentrators composed of parabolic reflectors that conduct solar radiation from the aperture area to the absorber. CPCs are widely used in many solar applications [1] such as photovoltaics [2], thermal [3], [4], daylighting [5], water detoxification and disinfection [6], [7], among others [8], [9]. This is because of their high optical efficiency, no-solar tracking system requirement at low solar concentration and their ability to capture both direct and diffuse solar radiation. Two key CPCs design parameters are concentration (C) and acceptance half-angle ( $\theta_a$ ), which are related by:  $C = 1/\sin(\theta_a)$ . The concentration is the ratio of aperture to absorber area, while half-angle is the angle between the line of the edge of the parabola and the axis of symmetry. CPCs have the optical property that all rays incident on the aperture area within acceptance angle will reach the absorber, whereas all the rays with an angle of incidence greater than  $\theta_a$  will bounce off the reflector and get lost off the aperture area.

The two-dimensional concentrator with cylindrical absorber is a particular type of CPC very useful for working with fluids. A popular geometry is the special case when  $\theta_a = 90^\circ$ , so the Concentration Ratio (CR) is equal to 1 Sun [10]; in which, if an ideal surface is considered, all the solar radiation that reaches the aperture is reflected towards the receiver tube. The CPC reflector is usually made of silver metallic foil-polymer or high specular reflectivity aluminum sheets [11], while the absorber is made of transparent glass or copper tubes depending on the application.

However, despite innovative changes in the geometric configurations of CPCs collectors for diverse applications, their manufacturing methods have not undergone significant modifications in recent years. The main manufacturing methods are lamination with a hydraulic press and by other machining methods, which generate errors in geometry and damage the high-reflectivity film, reducing the overall optical efficiency of the CPC. Recently, Carrillo et al. [12] developed a methodology to manufacture 2D cylindrical CPCs collectors using a Styrofoam mold cut by hot-wire technique, obtaining in this way the required shape without using mechanical fasteners. The performance results were analyzed by a photogrammetric technique.

In some studies, the thermal efficiency is investigated from the perspective of the support structure, design and construction where a frame of support ribs is used for its setting [13]. Other studies [14], use assemblies that required



joints which generate gaps between them. To reduce weight, they use light concrete shells as support structure instead of the steel frames, which provide stiffness and fill the gap between the supporting structure and reflecting surface. A study presented by Meiser et al. focused to investigate the deviation that occurs by the gravity load on the mirror shape and to study the deformation of the mirror because of gravity load and mounting forces and its effect on the shape of the mirror [15]. Balghouthi et al. studied the optical and thermal performance of a parabolic trough solar collector (PTSC) by photogrammetric techniques [16]. Besides, Osório et al. propose a method for customized design of a tracking CPC-type solar collector to minimize the energy cost [17], their results are based on the simulated ideal collector, discarding in this way, the fabrication bending or malformations that may affect the real performance. Atul S. Jadhav et al. [18] studied this factor that implies an energy loss of 17% in a low cost CPC system.

There are several methods to evaluate the collector's surface. Either by using pattern reflection deflectometry [19] or photogrammetry technique [20]; where Waghmare and Gulhane [21] found that the spread of reflected rays in the studied CPC increased because of manufacturing errors. Even using geometries mathematically defined and converted into CAD 3D models to be simulated with ray-tracing for estimating the flux distribution [22]. So, either one of these methods is effective depending on the particular purpose of the evaluation test.

In this context, to improve the optical efficiency of 2D cylindrical CPCs, this paper presents a manufacturing method that employs a 3D printed mold with the shape of the required CPC profile. Subsequently, a matrix is formed with the CPC mold, a drawer and a high reflectivity aluminum sheet. The polyurethane is injected into the cavity and waiting a time until the solidification reaction is completed. In the solidification process, the polyurethane expands and compresses the aluminum foil against the CPC mold and acquired the designed profile of the CPC. To evaluate the improvement in the geometry and optical efficiency of the CPC manufactured by the herein proposed method, a hybrid test was implemented using photogrammetry and ray tracing. Experimentally, the shape of the CPCs profile was characterized by photogrammetry. With this information, the shape of the entire CPC was reconstructed and a 3D model of the geometry was generated with CAD software. Subsequently, the geometry was exported to the TONATIUH software and a ray tracing simulation was carried out to determine the optical efficiency.

## 2 MATERIALS AND METHODS

The presented method to manufacture the collectors using the 3D printed mold comprises two stages. The first one is about the design, 3D printing and construction of the CPC. The second one describes the evaluation made to the collectors to verify the manufacturing process by calculating their optical efficiency using Monte Carlo ray tracing.

### 2.1 CPC design

The design is performed using equations 1 and 2 for the involute shape and equations 3 and 4 for the parabola profile on a  $xy$  plane, where  $r$  is the external radius of the receiving tube, the rim angle  $\varphi$  is the angle between the axis and a tangential line from the focus to the physical edge of the concentrator. In the especial case where  $\theta_a = 90^\circ$  just the merely involute is schemed (blue line in Fig. 1) since there is no macrofocal parabola for the collector. Finally,  $\theta_a$  is the half acceptance angle of the collector [23]. Fig. 1 shows the design for the CPC of  $CR = 1 \text{ sun}$  for a tube with  $r = 16.1 \text{ mm}$ ,  $CR$  is given by equation 5 where an angle of  $90^\circ$  was defined.

$$x = r(\sin\varphi - \varphi\cos\varphi) \quad (1)$$

$$y = -r(\varphi\sin\varphi + \cos\varphi) \quad (2)$$

$$\text{with } 0 \leq \varphi \leq \pi/2 + \theta_a$$

$$x_2 = r(\sin\varphi - A\cos\varphi) \quad (3)$$

$$y_2 = -r(A\sin\varphi + \cos\varphi) \quad (4)$$

$$\text{where } A = \frac{\frac{\pi}{2} + \theta_a + \varphi - \cos(\varphi - \theta_a)}{1 + \sin(\varphi - \theta_a)} \quad \text{with } \frac{\pi}{2} + \theta_a \leq \varphi \leq \frac{3\pi}{2} - \theta_a$$

$$CR = \frac{1}{\sin\theta_a} \quad (5)$$

### 2.2 3D printing and software tools

From the 2D generated involute, the 3D parabolic design that serves as a mold for the CPC is obtained. For this activity, AutoCAD® 2019 was used where the 2D involute is converted into a 3D mold of the collector. The design of the mold was made in 4 assembled parts (male-female), each piece has dimensions of 99.4 x 330 x 40.9 mm (limited to the 3D printing parameters), and thus reach the length required to cover the entire CPC receiver tube (1320 mm) used commonly in a photocatalytic reactor (low concentration e.g. 1-Sun). The mold manufacturing process was carried out in the 3D printer (ADEN®), with a 1.75 mm PLA filament thickness. The highly reflective aluminum sheet takes the geometric shape of the printed mold. In addition, a steel container was developed. This container has internal dimensions of 1320 x 102 x 50 mm, with a wall thickness of 5 mm. The mold container provides the adequate

setting to maintain the mold and the aluminum sheet together under tension, causing the latter to take the form of the designed CPC

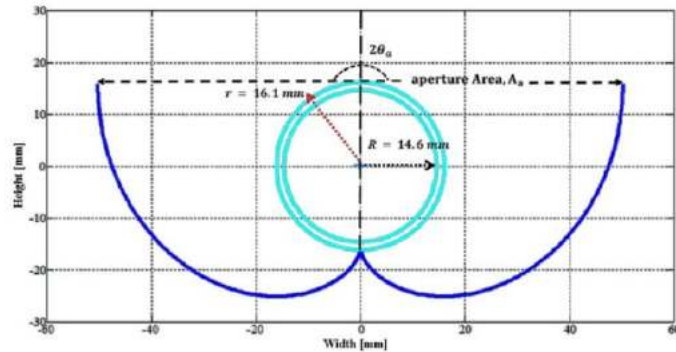


Fig. 1. Ideal 1-sun CPC design for a 32 mm glass tube diameter.

### 2.3 Polyurethane foam

In order to get the appropriate folding of the CPC laminate, liquid polyurethane foam was added into the container with the aluminum foil and the mold previously placed. The liquid polyurethane fulfills the function of exerting pressure on the reflective sheet against the mold as it expands throughout the container, thus taking the shape of the desired collector without using fasteners. The polyurethane foam is composed of two components (A and B) which are mixed in a 50:50 ratio and has a reaction time of 20 s to expand, while the drying time varies from 4 to 6 hours depending on the temperature and density of the components. 60 mL of each resin was used to cover the volume of the container enough to press the sheet against the mold.

### 2.4 Compound Parabolic Concentrator construction

Fig. 2 shows the manufacturing process. The flat surface of the 3D printed mold is placed inside the container in such a way that remains in contact with the bottom of the mold recipient (Fig. 2a). Subsequently, the aluminum sheet is placed on the mold (previously cut according to the calculated area of the CPC design) thus adjusting to the parabolic design (Fig. 2b). Once the sheet and mold are inside the container, the A-B polyurethane foam mixture is added and immediately, the container is closed (Fig. 2c). As a chemical reaction result of the A-B polyurethane mixture, it turns into a foam that expands, generating pressure on the anodized aluminum sheet against the mold, acquiring the CPC profile (Fig. 2d). Finally, the lid of the container is removed, and the mold is separated from the collector. In this way, a sheet with the involute-shape made with a polyurethane foam base is obtained (Fig. 2e).

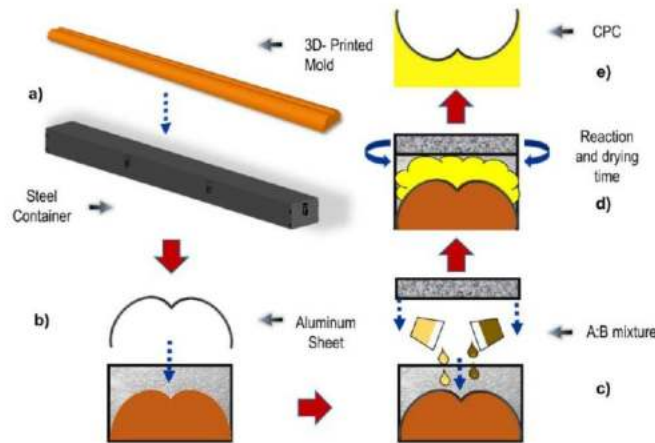


Fig. 2. CPC manufacturing process. a) the 3D-printed mold is introduced into the container, b) the anodized aluminum sheet is placed on top of the mold, c) the polyurethane foam mixture is poured, d) immediately closed where takes place the reaction and drying time and then e) the CPC is completed.

### 2.5 Evaluation of the CPC efficiency

A photogrammetry method was developed in order to validate the optical performance of the fabricated CPC and to evaluate the imperfections in the CPC sheet surface by machining or mechanical stress. As is illustrated in Fig. 3,



the method consists of performing a three-dimensional surface reconstruction by photographs taken to the object under study. The modeling of the images obtained from the CPC was carried out through the software Caesoft® (v. 2016.0.5.1718). The technique was performed using a 2 mm dot pattern (Fig.3a) printed on vinyl with 5 mm separation between each dot, previously defined by the software itself; according to the camera calibration performance, where angles and location were processed and those photographs who were out of calibration were removed by the software itself. The dot pattern was placed on the entire surface to model (Fig. 3b), so that the points follow the shape of the CPC (Fig. 3c). After that, pictures from different positions around the pattern were taken with a Nikon® D3000 camera equipped with AF-S Nikkor 18-55 mm lens. Afterwards, the images obtained were processed and analyzed by Photomodeler software [24].

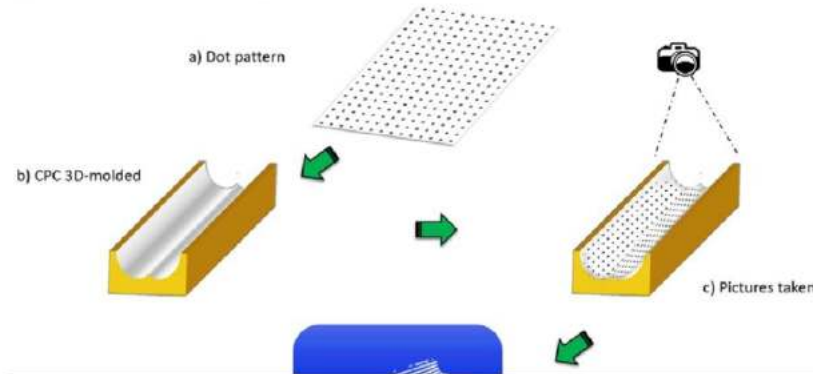


Fig. 3. Photogrammetry technique: a) 2 mm diameter dot pattern placed over the b) CPC 3D-molded and instantly c) a series of pictures are taken to process in PhotoModeler software and thus d) a point cloud is generated.

## 2.6 Analysis

Three types of evaluations were made in order to characterize and analyze both 3DM-CPC and CM-CPC: 1) a photogrammetric evaluation using a mathematical algorithm, 2) a Monte Carlo ray trace analysis of the structure based on the obtained data and 3) thermal energy generated by a water heating system simulated with SAM software.

The closest dot algorithm was used to evaluate the CPC-3D-surface of each CPC elaborated (3DM-CPC and CM-CPC) and thus compare it with an ideal design of a CPC of 1 sun geometric concentration (Fig. 1). This mathematical evaluation uses the dots array in x, y and z axis given by the PhotoModeler software and group the closest dots into clusters. The algorithm begins with an arbitrary starting data point. The neighborhood of this point is extracted using a distance (reference, in this case the 1-sun ideal CPC shape), if there are enough points within this neighborhood then the clustering process starts and the current data point becomes the first point of the new cluster. Otherwise, the point will be labeled as noise. For this first point in the new cluster, the points within a given  $\epsilon$  distance neighborhood also become part of the same cluster. This procedure of making all points in the  $\epsilon$  neighborhood belong to the same cluster is then repeated for all the new points that have been just added to the cluster group. After all dots are assigned, the centroids in the clusters are fixed. Finally, the closest clusters' centroids are compared to the 1-sun ideal CPC-reference[12]. These results are presented in the Fig. 5.

## 2.7 Evaluation with Ray Tracing software

To the closest point algorithm procedure, another workable assessment proposal with the data obtained is an advanced ray tracing study. The PhotoModeler software produces a 3D surface layer model (Fig. 4b) using the dot pattern of the images obtained according to the actual size of the 1-Sun CPC Collector (Fig. 4a). Afterwards, a .STL file is generated in PhotoModeler and exported to the design software AutoCAD®. In order to provide a real size and so manipulate it in Tonatiuh software, a pretreatment in AutoCAD® was made to the layer model (Fig. 4c) where a 5 mm thickness given to the surface, an aluminum solid material and a refined mesh model was assigned to the collector layer surface. Refinement of the surface mesh helps to mold smaller sections with less effect on the overall shape of the model. A mesh model comprises vertices, edges, and faces that use polygonal representation and it's applied to define a 3D shape model.

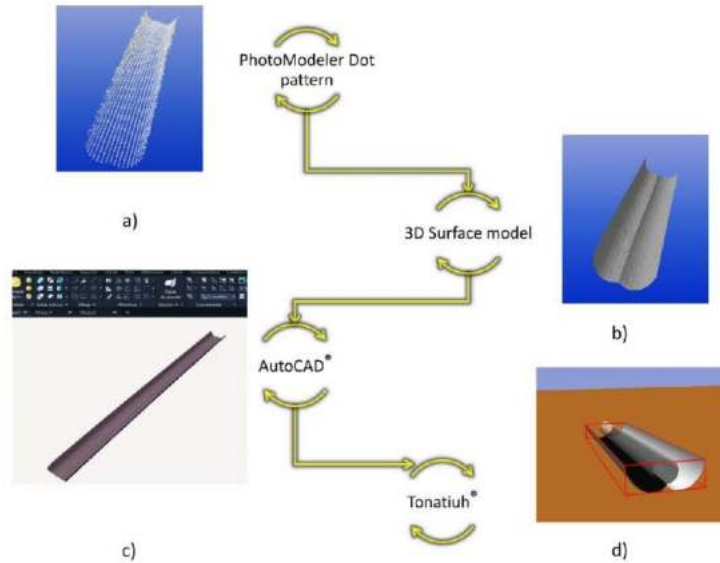


Fig. 4. Scheme showing the processing of the dot pattern obtained in PhotoModeler through the AutoCAD software and so finally simulate the ray trace model in Tonatiuh.

Subsequently, a file with extension .STL of the model was generated, which can be exported to be used with Tonatiuh® software (v. 2.2.4). This software is a Monte Carlo ray tracer for optical simulation of solar concentration systems. Parameters such as incident solar power, minimum, maximum and average flux, uniformity and centroid location are visualized in the Tonatiuh environment. The described evaluation procedure based on the simulation of the optical performance allows to compare the irradiance collection efficiency of the three 1-sun CPCs under study; ideal CPC, 3D-molded (3DM-CPC) and the conventionally manufactured (CM-CPC). For this study, a 21.00 latitude and -102.00 longitude sun position and an inclination of the collectors of 21° were included as simulation parameters. Absorbance in the receiver tube of 96% and a reflectance of 95% were established as optical parameters according to the standard material specification.

The software flux distribution utility divides the selected surface according to a bi-dimensional regular grid of equal area cells. The number of grid divisions in the width (I) and length (J) dimensions are defined by the user. For flat surfaces, the grid applies to the smallest rectangle enclosing the surface. Since in local coordinates, a flat surface always lies in the y=0 plane, the 3D impact position of photons hitting the 3D flat surface is transformed to the 2D rectangular grid following the transformation:

$$(u, v) = (x, z) \quad (6)$$

For cylindrical surfaces, the grid applies to the rectangle resulting from the unraveled surface of the cylinder starting from its generatrix. In local coordinates, the cylinder lies in the xy plane with its axis parallel to the z-axis. Thus, a photon hit point at the 2D rectangular grid is given by a suitable transformation of its 3D impact position (x,y,z):

$$(u, v) = (r \cdot \text{Atan2}(x, y), z) \quad (7)$$

Where  $r$  is the cylinder radius and  $\text{arctan2}$  is the two-argument arctangent function. It is then possible to count the number of photons intersecting each grid cell. With this knowledge the flux distribution and other related statistics can be computed. The radiative flux incident on a grid cell (i,j) is:

$$\Phi_{i,j} = \frac{N_{i,j} P_{ph}}{A_c} \quad (8)$$

Where  $N_{i,j}$  is the number of photons intersecting the grid cell (i,j),  $P_{ph}$  is the power carried by each photon and  $A_c$  denotes the grid cell area. The total incident power on the surface is given by:

$$\dot{Q} = P_{ph} \sum_{i=1}^I \sum_{j=1}^J N_{i,j} \quad (9)$$

The average radiative flux in the surface is given by:

$$\bar{\Phi} = \frac{P_{ph} \sum_{l=1}^I \sum_{j=1}^J \Phi_{i,j}}{IJ} \quad (10)$$

### 2.8 Evaluation of thermal efficiency

In order to estimate the impact on the thermal energy generated by a water heating system with the CPCs under study, SAM software was used [25]. SAM applies the Hottel-Whillier-Bliss (equation 11) to express the thermal performance of a collector under steady state. This equation to estimates the useful gain by the solar heating system as follows:

$$Q_u = A \cdot [\eta_{opt} \cdot FR\tau\alpha \cdot \kappa_{\tau\alpha}(\theta_b) \cdot G_I - FRU_L(T_i - T_{amb})] \quad (11)$$

Where:

$Q_u$ - Solar field useful gain (kW)

$A$ - Total system collector area (m<sup>2</sup>)

$\eta_{opt} \cdot FR\tau\alpha$  - Optical gain

$\kappa_{\tau\alpha}(\theta_b)$  - Modifier at AM 1.5

$G_I$ - Incident solar irradiance normal to the collector plane W m<sup>-2</sup>

$FRU_L$ - Thermal loss coefficient

$T_i$ - Solar field inlet temperature of the working fluid

$T_{\infty}$ - Dry bulb temperature

Optical gain factor ( $FR\tau\alpha$ ) in SAM software was assumed as a function of the average CPC optical efficiency calculated by ray tracing in this work ( $\eta_{opt}$ ) as shown in Table 1.

Table 1. Relative optical gain in Hottel-Whillier-Bliss (equation 11) as a function of the CPC optical efficiency.

Type	Average optical efficiency $\eta_{opt}$	Coef. $\eta_{opt} \cdot FR\tau\alpha$
Ideal CPC	1	0.607
3DM - CPC	0.95	0.57665
CM - CPC	0.82	0.49774

The main parameters considered in the SAM simulation were:

Table 2. Parameters of the simulated solar water heating system

Parameter	Value
Location	Aguascalientes, México (21.88° lat, -102.296° lon)
Average hot water usage	1000 L/day <sup>1</sup>
Collector tilt angle	22 °
Total system flow rate	0.83 kg/s <sup>-1</sup>
Working fluid	Water
No. of Collectors	15
Collector Area	2.78 m <sup>2</sup>
FRta	0.607, 0.57665, 0.49774
FRUL	3.72 W/m <sup>2</sup> °C
Incident angle modifier	0.95
Test fluid	Glycol
Test flow	0.0556 kg/s <sup>-1</sup>
Solar tank volume	1000 L
Outlet set temperature	80 °C

## 3 RESULTS

### 3.1 closest dot algorithm

The Fig. 5a (up-left) shows the CPC 3D mold data (blue dots) and its mean absolute error (down-left) acquired by using the photogrammetry technique and represented in a single plane comparing to the ideal geometric 1-sun CPC



shape (red dots line) elaborated in Matlab software in accordance with equations 1-5. Likewise, the Fig.5b exhibits the comparison of the CM-CPC (up-right) specifying its mean absolute error (down-right), in which construction techniques such as bending, punching and manual bending were used. The 3DM-CPC mean deviation stated in the Fig. 5a is barely 1.2 mm which is a remarkable, since a novel and cheap procedure was followed according to the manufacturing method shown in Fig. 3. This proves that the proposed manufacturing technique using a 3D mold and polyurethane foam is adequate and considerably better approximated to the ideal shape of the analyzed CPC.

On the other hand, the results show a major mean deviation of the CM-CPC with a 3.19 mm error. As shown in Fig. 5b the curved shape of the involute was not achieved specially at the CPC edges, it can be attributed to the less precise hand-made manufacture technique.

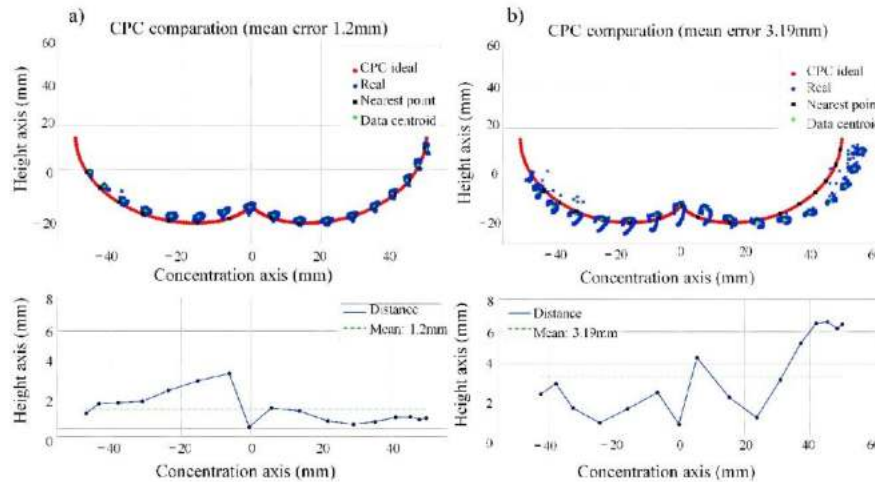


Fig. 5. Graphs showing the ideal 1-sun-CPC (red dotted line), compared to the 3D-mold technique 3DM-CPC (a) and the conventionally manufactured CM-CPC (b) and their mean error in mm, respectively (below).

Regardless of the mean absolute error (MAE) in the 3DM-CPC according to its dimensions and shape, it becomes negligible. This MAE can be attributed to two causes, 1) the length of the CPC (1300 mm) which is considerably large and 2) the data centroids, that is a high data number given by the software itself. This is because of the dots pattern is very close from one point to another (5 mm) for an optimal surface scan, moreover the CPC shape is very curved on its edges because of its parabolic form, which makes it difficult for the software to process the images. It should be noted, however, that there is an inherent uncertainty in the data collected by the photogrammetric technique, which is attributed to different factors that determine the accuracy of a photogrammetric analysis. The key factors affecting accuracy are photo resolution, camera calibration, angles, photo orientation, quality photo redundancy and targets/markings precision. Aspects like focal length, distortion lens, number of pixels, angled photos for more detail, number of photos, target size and software precision marking targets by pixel are some examples of them.

An estimation of the root mean square standard error (RMSE) was calculated using the data collected by the PhotoModeler software that provides a set of residual points in pixels from the 3D surface layer model. The RMSE value calculated is  $\pm 0.01$  px or 0.002 mm. Thus, a general projected error data is considered for the reported result.

### 3.2 Result of ray tracing analysis

Using Tonatiuh<sup>®</sup> software, a Monte Carlo ray trace studio was simulated for the three surface models in the same solar conditions (angle, position, location) in order to evaluate the concentrating performance. Fig. 6 shows the ray trace simulation for a 21.00 latitude and -102.00 longitude sun position to compare the ideal CPC, the 3DM-CPC and the CM-CPC.

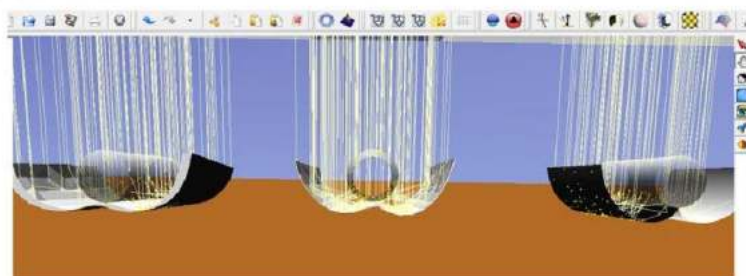


Fig. 6. Ray trace simulation environment for all CPC configurations: ideal (right), 3DM-CPC (center) and CM-CPC (left).



The ray tracing studio consists in estimate the four-day seasons positions (solstices and equinoxes) to show and compare the 3DM-CPC and the CM-CPC functionality and efficiency against the 1-sun ideal collector, measuring hourly during 9 hours (9:00 am – 6:00 pm) the simulated incident radiative flux collected in the receptor tube during each of the four days (vernal equinox, summer solstice, autumnal equinox and winter solstice), the results are shown in Fig.7.

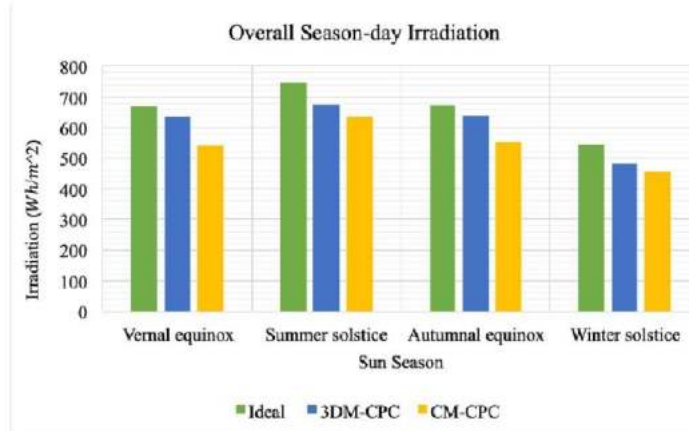


Fig. 7. Shows the irradiances performances of the ideal 1-sun-CPC, 3DM-CPC and CM-CPC for the four sun seasons; vernal equinox (March 21), summer solstice (June 21), autumnal equinox (September 23) and winter solstice (December 23).

The results presented in Fig. 7 show the overall season-day sun irradiation for the four dates in every collector based on the integrated irradiation. The collecting performance of the 3DM-CPC and the CM-CPC are compared with the ideal 1-sun CPC using the results of the area under the curve related to the simulated irradiance along each day for each collector.

As can be seen in Fig. 7, the difference between a CM-CPC and a 3DM-CPC is relevant, the 3DM-CPC showed a higher solar collection efficiency factor than the CM-CPC. Assuming that the ideal 1-Sun collector has the 100% percent efficiency factor, the 3DM-CPC and the CM-CPC obtain a 95 % max – 88 % min and an 85% max – 81% min range, respectively. Although 3DM-CPC has some errors in the reflective surface, it is close to its shape because of the presented manufacturing technique. This allows 3DM-CPC to have a considerably better performance than the CM-CPC built from mechanical shaping techniques and tools. The graphs in Fig. 7 confirms the performance difference according to the manufacturing technique respect to the ideal one, being this the most efficient on the four graphs, followed by the one with the 3DM-CPC and lastly the CM-CPC collector shape.

### 3.3 Result of thermal energy generated

In order to validate the benefits of the different CPCs, the study was complemented by a thermal energy performance analysis of a simulated 1000 L CPC solar plant with 15 collectors and 2.78 m<sup>2</sup> of total area (full parameters are shown in table 2). Fig. 8 shows the thermal energy in kWh generated throughout a year comparing the 3 different CPCs under study. In all the months evaluated, the difference of thermal energy generated by using 3DM-CPC compared with CM-CPC is significant, achieving improvements up to 13% in December. It is important to notice that the performance of the 3DM-CPC collector is, in most cases, similar to the ideal-CPC. The smallest difference between the thermal energy generated by a solar plant modelled with a 3DM-CPC and the hypothetical ideal case is only 1%, evaluated by the SAM software in the months of April and October. As can be seen in table 3, in one year a benefit of 1,631 kWh (≈9.4%) could be obtained, represented by the better reflective quality of the 3DM-CPC in which the surface of the aluminum sheet suffers less damage

Table 3. Summary - thermal energy generated by the system

	CPC Solar Manufacture type		
	Ideal CPC	3DM- CPC	CM – CPC
Annual thermal energy generated [kWh]	19 440.73	19 016.18	17 384.96

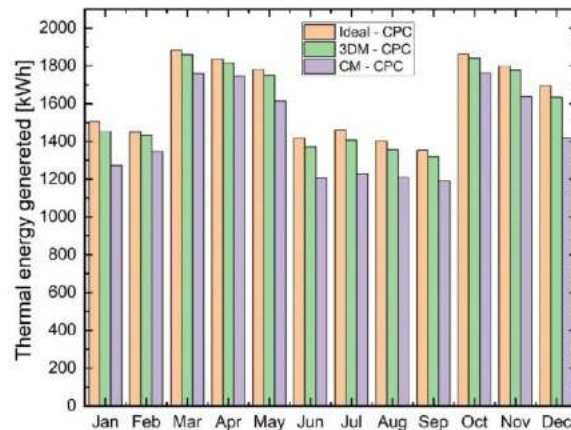


Fig. 8. Monthly thermal energy generated by the solar water heating system.

#### 4 CONCLUSION

In the presented work a manufacturing process to fabricate a CPC with the aid of a 3D printed mold and polyurethane foam (3DM-CPC) is proposed and is compared to a conventionally manufactured CPC (CM-CPC) in reference to an ideal 1-sun concentration system. An alternative method for the optical evaluation of CPC collectors using ray tracing analysis in a 3D model generated by inverse engineering is also proposed. With this novel evaluation procedure, the optical performance of both the 3DM-CPC and CM-CPC CPCs were evaluated through a photogrammetric optical procedure and analyzed by a closest point mathematical algorithm. The results in manufacturing efficiency gives a MAE of 1.2 and 3.19 for the 3DM-CPC and the CM-CPC, respectively. A Monte Carlo ray tracing evaluation was made to support the collector shape assessment, where a four-day sun positions analysis shows under different irradiation conditions the overall performance and effectiveness of the 3DM-CPC and CM-CPC collectors. Showing that in everyday the 3DM-CPC collector obtained a better efficiency than the CM-CPC, where a 95% efficiency on the 3DM-CPC was reached against the 82% efficiency of the CM-CPC in the autumnal equinox day i.e., both compared to the ideal 1-sun-CPC collector (100% efficiency factor). Even though the low irradiance contribution in the case of the winter solstice, the 3DM-CPC shows the best irradiation collecting results. Both results reiterate the advantage and effectiveness of the proposed manufacturing method. This assessment infers a determinant factor in solar collector's optical performance, especially in low-power concentration because the limited UV solar radiation available, e.g. for chemical processes. The improvements in the presented CPC manufacturing process are verified by studying the performance of a Solar CPC Thermal Plant using the SAM software. Yield improves considerably, up to a maximum of 13% in December evaluation. The benefit could be 1,631 kWh ( $\approx 9.4\%$ ) in the annual performance of the plant with the improved CPCs.

#### 5 ACKNOWLEDGMENTS

The authors would like to acknowledge the Consejo Nacional de Ciencia y Tecnología (CONACYT): for the financial support to the project APN 2015-01-1651 and to project 317264. Also, for providing the postgraduate scholarship to Pedro R. Martínez-Manuel. And also thanks to the Instituto para el Desarrollo de la Sociedad del Conocimiento para el Estado de Aguascalientes for the financing received through Fondo de Innovación Tecnológica 2022 project 012-FEIT-2022. Thanks to M.C. Albor Cortés for technical assistance.

#### 6 REFERENCES

- [1] Tian, M., Su, Y., Zheng, H., Pei, G., Li, G., Riffat, S. (2018). A review on the recent research progress in the compound parabolic concentrator (CPC) for solar energy applications. *Renewable and Sustainable Energy Reviews*, vol. 82, no. October 2017, 1272–1296. DOI:10.1016/j.rser.2017.09.050
- [2] Jaaz, A. H., Hasan, H. A., Sopian, K., Haji Ruslan, M. H. Bin, Zaidi, S. H. (2017). Design and development of compound parabolic concentrating for photovoltaic solar collector: Review. *Renewable and Sustainable Energy Reviews*, vol. 76, 1108–1121. DOI:10.1016/J.RSER.2017.03.127
- [3] Santos-González, I., García-Valladares, O., Ortega, N., Gómez, V. H. (2017). Numerical Modeling and Experimental Analysis of the Thermal Performance of a Compound Parabolic Concentrator, *Applied Thermal Engineering*, vol. 114. DOI:10.1016/j.applthermaleng.2016.10.100



- [4] Mishra, R. K., Garg, V., Tiwari, G. N. (2017). Energy matrices of U-shaped evacuated tubular collector (ETC) integrated with compound parabolic concentrator (CPC). *Solar Energy*, vol. 153, 531–539. DOI:10.1016/J.SOLENER.2017.06.004
- [5] Yin, P., Lv, J., Wang, X., Huang, R. (2021). A spectral splitting planar solar concentrator with a linear compound parabolic lightguide for optical fiber daylighting. *Renewable Energy*, vol. 179, 778–787. DOI:10.1016/j.renene.2021.07.100
- [6] McMichael, S., Waso, M., Reyneke, B., Khan, W., Byrne, J. A., Fernandez-Ibanez, P. (2021). Electrochemically assisted photocatalysis for the disinfection of rainwater under solar irradiation. *Applied Catalysis B: Environmental*, vol. 281, no. August 2020, 119485. DOI:10.1016/j.apcatb.2020.119485
- [7] Cabrera-Reina, A., Miralles-Cuevas, S., Rivas, G., Sánchez Pérez, J. A. (2019). Comparison of different detoxification pilot plants for the treatment of industrial wastewater by solar photo-Fenton: Are raceway pond reactors a feasible option?. *Science of the Total Environment*, vol. 648, 601–608. DOI:10.1016/j.scitotenv.2018.08.143
- [8] Tiwari, D., Sherwani, A. F., Atheaya, D., Arora, A. (2017). Energy and exergy analysis of solar driven recuperated organic Rankine cycle using glazed reverse absorber conventional compound parabolic concentrator (GRACCPC) system. *Solar Energy*, vol. 155, 1431–1442. DOI:10.1016/J.SOLENER.2017.08.001
- [9] Elashmawy, M. (2017). An experimental investigation of a parabolic concentrator solar tracking system integrated with a tubular solar still. *Desalination*, vol. 411, 1–8. DOI:10.1016/J.DESAL.2017.02.003
- [10] Moreno-SanSegundo, J., Martín-Sómer, M., Marugán, J. (2022). Dynamic concentration factor: A novel parameter for the rigorous evaluation of solar compound parabolic collectors. *Chemical Engineering Journal*, vol. 437, no. December 2021. DOI:10.1016/j.cej.2022.135360
- [11] Fendrich, M. A., Quaranta, A., Orlandi, M., Bettonte, M., Miotello, A. (2018). Solar concentration for wastewaters remediation: A review of materials and technologies. *Applied Sciences*, vol. 9, no. 1. DOI:10.3390/app9010118
- [12] Carrillo, J. G., Peña-Cruz, M., Terrón-Hernández, M., Valentin, L. (2020). Low Cost High-Accuracy CPC System - A Manufacturing Methodology. *Journal of Solar Energy Engineering*, 1–13. DOI:10.1115/1.4048015
- [13] Chafie, M., Ben Aissa, M. F., Bouadila, S., Balghouthi, M., Farhat, A., Guizani, A. (2016). Experimental investigation of parabolic trough collector system under Tunisian climate: Design, manufacturing and performance assessment. *Applied Thermal Engineering*. DOI:10.1016/j.applthermaleng.2016.02.073
- [14] Forman, P., Müller, S., Ahrens, M. A., Schnell, J., Mark, P., Höffer, R., Hennecke, K., Krüger, J. (2015). Light concrete shells for parabolic trough collectors - Conceptual design, prototype and proof of accuracy. *Solar Energy*, vol. 111, 364–377. DOI:10.1016/j.solener.2014.11.002
- [15] Meiser, S., Schneider, S., Lüpfer, E., Schiricke, B., Pitz-Paal, R. (2017). Evaluation and assessment of gravity load on mirror shape and focusing quality of parabolic trough solar mirrors using finite-element analysis. *Applied Energy*. DOI:10.1016/j.apenergy.2016.04.045
- [16] Balghouthi, M., Ali, A. B. H., Trabelsi, S. E., Guizani, A. (2014). Optical and thermal evaluations of a medium temperature parabolic trough solar collector used in a cooling installation. *Energy Conversion and Management*. DOI:10.1016/j.enconman.2014.06.095
- [17] Osório, T., Horta, P., Collares-Pereira, M. (2019). Method for customized design of a quasi-stationary CPC-type solar collector to minimize the energy cost. *Renewable Energy*, vol. 133, 1086–1098. DOI:10.1016/J.RENENE.2018.10.110
- [18] Jadhav, A. S., Gudekar, A. S., Patil, R. G., Kale, D. M., Panse, S. V., Joshi, J. B. (2013). Performance analysis of a novel and cost effective CPC system. *Energy Conversion and Management*, vol. 66, 56–65. DOI:10.1016/J.ENCONMAN.2012.09.030
- [19] El Ydrissi, M., Ghennioui, H., Bennouna, E. G., Farid, A. (2019). A review of optical errors and available applications of deflectometry technique in solar thermal power applications. *Renewable and Sustainable Energy Reviews*, vol. 116, no. October, 109438. DOI:10.1016/j.rser.2019.109438
- [20] El Ydrissi, M., Ghennioui, H., Bennouna, E. G., Farid, A. (2019). Geometric, optical and thermal analysis for solar parabolic trough concentrator efficiency improvement using the photogrammetry technique under semi-arid climate. *Energy Procedia*, vol. 157, no. 2018, 1050–1060. DOI:10.1016/j.egypro.2018.11.272
- [21] Waghmare, S. A., Gulhane, N. P. (2017). Optical evaluation of compound parabolic collector with low acceptance angle. *Optik*, vol. 149, 359–371. DOI:10.1016/J.IJLEO.2017.09.039
- [22] Lara, F., Cerezo, J., Acuña, A., González-Ángeles, A., Velázquez, N., Ruelas, A., López-Zavala, R. (2021). Design, optimization and comparative study of a solar CPC with a fully illuminated tubular receiver and a fin inverted V-shaped receiver. *Applied Thermal Engineering*, vol. 184, 116141. DOI:10.1016/J.APPLTHERMALENG.2020.116141

- [23] Salgado-Tránsito, I., Jiménez-González, A. E., Ramón-García, M. L., Pineda-Arellano, C. A., Estrada-Gasca, C. A. (2015). Design of a novel CPC collector for the photodegradation of carbaryl pesticides as a function of the solar concentration ratio. *Solar Energy*, vol. 115, 537–551. DOI:10.1016/j.solener.2015.02.034
- [24] King, P., Sansom, C., Comley, P. (2020). Photogrammetry for concentrating solar collector form measurement, validated using a coordinate measuring machine. *Sustainability*, vol. 12, no. 1, 1–20. DOI:10.3390/su12010196
- [25] Li, X., Jin, J., Yang, D., Xu, N., Wang, Y., Mi, X. (2019). Comparison of tower and trough solar thermal power plant efficiencies in different regions of China based on SAM simulation. *AIP Conference Proceedings*, vol. 2126, no. July. DOI:10.1063/1.5117545

*Paper submitted: 17.05.2022.*

*Paper accepted: 25.07.2022.*

*This is an open access article distributed under the CC BY 4.0 terms and conditions.*

## ANNEX C

```
#include <Wire.h> // enable I2C.
//#define address 104 //default I2C ID number for EZO Flow
#define TOTAL_CIRCUITS 2 // <-- CHANGE THIS | set how many I2C circuits are
attached to the Tentacle

//4 CHANNEL RELAY INPUTS
#define DO 8 //CHANNEL 1
#define CE 9 //CHANNEL 2
#define ROPUMP 6 //CHANNEL 3
#define REACTORPUMP 7 //CHANNEL 4

//DOSING PUMP LINES////////////////////////////////////-----
-----
// Needed for the pump reading
bool condicion_activacion_bomba_roja = false;
bool condicion_activacion_bomba_verde = false;
String activar_bomba_consola = "";

// Green dosing pump activation
boolean bV_resp_done = false;
String bV_resp = "";
void serialEvent3() {
    bV_resp = Serial3.readStringUntil(13);
    bV_resp_done = true;
}

// Red dosing pump activation
boolean bR_resp_done = false;
String bR_resp = "";
void serialEvent2() {
    bR_resp = Serial2.readStringUntil(13);
    bR_resp_done = true;
}

//DOSING PUMP LINES////////////////////////////////////
float ml=0;
const unsigned int baud_host = 9600; // set baud rate for host serial monitor(pc/mac/other)
const unsigned int send_readings_every = 800; // set at what intervals the readings are sent to the
computer (NOTE: this is not the frequency of taking the readings!)
unsigned long next_serial_time;

//// Flow sensor lines //////////////////////////////////
String inputstring = ""; //a string to hold incoming data from the PC
String sensorstring = ""; //a string to hold the data from the Atlas
Scientific product
boolean input_string_complete = false; //have we received all the data from the PC
boolean sensor_string_complete = false; //have we received all the data from the
Atlas Scientific product
float tv; //used to hold a floating point number that
is the total volume

//flow sensor //////////////////////////////////
char sensordata[30]; // A 30 byte character array to hold incoming data
from the sensors
byte sensor_bytes_received = 0; // We need to know how many characters bytes have
been received
byte code = 0; // used to hold the I2C response code.
byte in_char = 0; // used as a 1 byte buffer to store in bound bytes
from the I2C Circuit.

int channel_ids[] = {97, 99}; // <-- CHANGE THIS. A list of I2C ids that you set your circuits
to. 104 id for flow sensor
```

```

char *channel_names[] = {"DO", "PH"}; // <-- CHANGE THIS. A list of channel names (must be the
same order as in channel_ids[]) - only used to designate the readings in serial communications
String readings[TOTAL_CIRCUITS]; // an array of strings to hold the readings of each
channel
int channel = 0; // INT pointer to hold the current position in the
channel_ids/channel_names array

const unsigned int reading_delay = 1000; // time to wait for the circuit to process a read
command. datasheets say 1 second.
unsigned long next_reading_time; // holds the time when the next reading should be
ready from the circuit
boolean request_pending = false; // wether or not we're waiting for a reading

const unsigned int blink_frequency = 250; // the frequency of the led blinking, in milliseconds
unsigned long next_blink_time; // holds the next time the led should change state
//boolean led_state = LOW; // keeps track of the current led state
char estado_llenado = 0;
bool irr = true;

bool message_panel = 0;
//CONDUCTIVITY LINES//
float Current = 0; //4-20 mA (mapped)
float rawADCValue = 0; //0-1023
float ADCVoltage = 0; //0-5 V
float conductivity = 0; // uS (mapped)
int ADC_Pin = A9;
unsigned long time_read = 0; // interval for analog reading

void setup() {
  Serial.begin(9600); // Set the hardware serial port.
  Serial1.begin(9600); // Set the hardware serial port 1.
  Serial2.begin(9600); // Set the hardware serial port 2.
  Serial3.begin(9600); //set baud rate for software serial port_3
to 9600
  Wire.begin(); // enable I2C port.
  next_serial_time = millis() + send_readings_every; // calculate the next point in time we should
do serial communications
  //pinMode (3, INPUT);
  pinMode (A0, INPUT); //Level sensor LOW 1
  pinMode (A1, INPUT); //Level sensor HIGH 1
  pinMode (A2, INPUT); //Level sensor LOW 2
  pinMode (A3, INPUT); //Level sensor HIGH 2
  pinMode (A4, INPUT); //Level sensor LOW 3
  pinMode (A5, INPUT); //Level sensor HIGH 3
  pinMode (A9, INPUT); // CE Sensor
  pinMode(8, OUTPUT); // set the digital pin 8 as CE or COND valve1 output
  pinMode(9, OUTPUT); // sets the digital pin 9 as DO valve2 output
  pinMode(6, OUTPUT); // sets the digital pin 10 as main (RO) pump starter
  pinMode (7, OUTPUT); // sets the digital pin 11 as reactor pump starter
  //FLOW METER LINES
  inputstring.reserve(10); //set aside some bytes for receiving data
from the PC
  sensorstring.reserve(30); //set aside some bytes for receiving data
from Atlas Scientific product

  //START CONDITIONS FOR THE POTABILIZER/////
  estado_llenado = 0;
  digitalWrite(ROPUMP, HIGH);
  digitalWrite(REACTORPUMP, HIGH);
  Serial2.print("Dstart,off");
  Serial3.print("Dstart,off");
  delay (100);
}

void serialEvent() {
  { //if the hardware serial port_0 receives a char
    inputstring = Serial.readStringUntil(13); //read the string until we see a <CR>
    input_string_complete = true;
  }
}

```

```

{
  activar_bomba_consola = Serial.read();          //read the string until we see a <CR>

  if ( activar_bomba_consola == "82") {
    condicion_activacion_bomba_roja = true;
    Serial.println("-----");
    Serial.println("Se activo bomba roja");
    Serial.println("-----");
  }
  if ( activar_bomba_consola == "86") {
    condicion_activacion_bomba_verde = true;
    Serial.println("-----");
    Serial.println("Se activo bomba verde");
    Serial.println("-----");
  }
}
}

//set the flag used to tell if we have received a completed string from the PC

void serialEvent1() {                          //if the hardware serial port_1 receives a
char                                           //read the string until we see a <CR>
  sensorstring = Serial1.readStringUntil(13); //set the flag used to tell if we have
  sensor_string_complete = true;              received a completed string from the PC
}

void loop() {

  {
    do_sensor_readings();
    do_serial();
  }

  //FLOW SKETCH
  { //here we go...
    if (input_string_complete == true) {      //if a string from the PC has been received
in its entirety                               //send that string to the Atlas Scientific
    Serial1.print(inputstring);               product
    Serial1.print('\r');                       //add a <CR> to the end of the string
    inputstring = "";                          //clear the string
    input_string_complete = false;            //reset the flag used to tell if we have
received a completed string from the PC
    }
    if (sensor_string_complete == true) {     //if a string from the Atlas Scientific
product has been received in its entirety     // Serial.println(sensorstring);
    Serial.println(sensorstring); //send that string to the PC's serial monitor
    //uncomment this section to see how to convert the total volume reading from a string to a
float
    if (isdigit(sensorstring[0])) {          //if the first character in the string is
a digit                                       //convert the string to a floating point
    tv = sensorstring.toFloat();              number so it can be evaluated by the Arduino
    }
    //
    f ();
    Serial.print("flow.txt=\");
    Serial.print(tv);                        //FLOW
    Serial.print("\");
    f ();
  }
  sensorstring = "";                          //clear the string:
  sensor_string_complete = false;            //reset the flag used to tell if we have
received a completed string from the Atlas Scientific product
}
//FLOW SKETCH

```

```

// LEVEL SENSORS FROM 1 TO 3 (1 RO MAIN TANK, 2 REACTOR TANK AND 3 CLEAN WATER TANK)
uint16_t LSL1 = analogRead(A0);
uint16_t LSH1 = analogRead(A1);
uint16_t LSL2 = analogRead(A2);
uint16_t LSH2 = analogRead(A3);
uint16_t LSL3 = analogRead(A4);
uint16_t LSH3 = analogRead(A5);
// Serial.println(LSL2);
//Serial.println(LSH3);

// // MAIN TANK (1) IS EMPTIED AND THE REACTOR TANK (2) IS FILLED LSH1 AND LSL1 ARE SENSING
WATER AT THE BEGINNING
digitalRead (6);
digitalRead (7);
if ( LSL3 < 400 ) {
    estado_llenado = 1;
}
// Estado 1. TANK 2 IS EMPTIED AND FINAL TANK (3) IS FILLED
if ( estado_llenado == 1) {
    if ( LSL2 > 400 && LSH3 < 400 ) {
        //TURN ON REACTOR PUMP (2)
        digitalWrite(ROPUMP, HIGH);
        digitalWrite(REACTORPUMP, LOW);
        //Serial.print(":\t");
        //          if (message_panel != 1){

        //          message_panel = 1;
    }

    if ( LSL2 < 400 || LSH3 > 400) {
        //TURN OFF REACTOR PUMP (2)
        digitalWrite(ROPUMP, HIGH);
        digitalWrite(REACTORPUMP, HIGH);
        estado_llenado = 0;
        //Serial.print(":\t");
        //          if (message_panel != 2){

        //          message_panel = 2;
        ////          }
    }
}

if ( estado_llenado == 0) {
    if ( LSL1 > 400 && LSH2 < 400 ) {
        //TURN ON MAIN PUMP (1)
        digitalWrite(REACTORPUMP, HIGH);
        digitalWrite(ROPUMP, LOW);

        // Serial.print(":\t");
        //          if (message_panel != 3){

        //          message_panel = 3;
    }

    if ( LSL1 < 400 || LSH2 > 400) {
        // TURN OFF MAIN PUMP (1)
        digitalWrite(REACTORPUMP, HIGH);
        digitalWrite(ROPUMP, HIGH);
        estado_llenado = 1;
        //Serial.print(":\t");
        //          if (message_panel != 4){

        //          message_panel = 4;
    }
}
// Slow things down or the serial monitor will go mad
delay (250);

```





```

    f ();
    Serial.print("states img END");
}
if ( LSL2 > 400 && LSH2 < 400 ) {
    f ();
    Serial.print("p4.pic=26");
    f ();
    Serial.print("states img END");
}
if ( LSH2 > 400 ) {
    f ();
    Serial.print("p4.pic=23");
    f ();
    Serial.print("states img END");
}
if ( LSL3 < 400 ) {
    f ();
    Serial.print("p5.pic=24");
    f ();
    Serial.print("states img END");
}
if ( LSL3 > 400 && LSH3 < 400 ) {
    f ();
    Serial.print("p5.pic=26");
    f ();
    Serial.print("states img END");
}
if ( LSH3 > 400 ) {
    f ();
    Serial.print("p5.pic=23");
    f ();
    Serial.print("states img END");
}
delay (250);
}

//Red dossing pump

if (condicion_activacion_bomba_roja == true) {
    String bombeo_rojo = "3";    //Red pump   [ Serial 2 ]

    //Codigo para activar bomba roja
    Serial2.print("D," + bombeo_rojo + "\r" );           // Red dossing pump activation

    Serial.println("Bomba roja se ha activado");
    condicion_activacion_bomba_roja = false;
}
//Green dossing pump

if (condicion_activacion_bomba_verde == true) {
    String bombeo_verde = "5";    //green pump   [ Serial 3 ]

    //Codigo para activar bomba roja
    Serial3.print("D," + bombeo_verde + "\r" );           // Green dossing pump activation

    Serial.println("Bomba verde se ha activado");
    condicion_activacion_bomba_verde = false;
}

//Read Activation pumps

// Red pump
if (bR_resp_done == true) {
    Serial.println("Respuesta de bomba roja: " + bR_resp);

    if (isdigit(bR_resp[0]) || bR_resp[0] == '-') {
        ml = bR_resp.toFloat();
    }
}

```

```

    bR_resp = "";
    bR_resp_done = false;
}

// Green pump
if (bV_resp_done == true) {
    Serial.println("Respuesta de bomba verde: " + bV_resp);

    if (isdigit(bV_resp[0]) || bV_resp[0] == '-') {
        ml = bV_resp.toFloat();
    }

    bV_resp = "";
    bV_resp_done = false;
}
//End reading pumps

readADC();
}

void f () {
    Serial.write(0xff);
    Serial.write(0xff);
    Serial.write(0xff);
}
void readADC()
{
    rawADCValue = 0; //Reset the value before summation

    for (int i = 0; i < 1000; i++) //Do 100 readings
    {
        rawADCValue += analogRead(ADC_Pin);
        //delay(1); //"settling time" for the ADC
        //Sum the results 100 times
    }
    {
        int intval = millis() - time_read; // get current time

        if (intval >= 1000) // excute new reading if intval over 1000ms

            time_read = millis(); // set read time to 'time_read'
    }

    ADCVoltage = (float)(rawADCValue / 1000.0) * (4020 / 1024.0); //The average is converted into
    voltage (5000 mV = 5 V)

    //For 220 Ohm: 4 mA * 220 Ohm = 880 mV, 20 mA * 220 Ohm = 4400 mV
    //For 250 Ohm: 4 mA * 250 Ohm = 1000 mV, 20 mA * 250 Ohm = 5000 mV
    //Note: measure the 220 (or 250) resistor, and calculate the actual voltages
    Current = mapfloat(ADCVoltage, 1000, 4020, 4, 20);
    // Voltage between 880-4400 mV is distributed as current 4-20 mA
    conductivity = mapfloat(Current, 4.00064, 20, 1, 18800);
    Serial.print("CE: ");
    Serial.println(conductivity);
    if (conductivity <= 800){
        digitalWrite (CE,LOW);
    }
    else {
        digitalWrite (CE, HIGH);
    }
    f ();
    Serial.print("conductivity.txt=\");
    Serial.print(conductivity); //conductivity
    Serial.print("\");
    f ();
    delay (10000);
}
}

```

```

// do serial communication in a "asynchronous" way
void do_serial() {
  if (millis() >= next_serial_time) { // is it time for the next serial communication?
    for (int i = 0; i < TOTAL_CIRCUITS; i++) { // loop through all the sensors

      Serial.print(channel_names[i]); // print channel name
      Serial.print(":\t");
      Serial.println(readings[i]); // print the actual reading

      if (readings[i].toDouble() < 6 && i == 0) { // DO : i = 0
        digitalWrite(DO, HIGH);
      }
      if (readings[i].toDouble() >= 6 && i == 0) { // DO
        digitalWrite(DO, LOW);
      }
      if (readings[i].toDouble() <= 6.5 && i == 1) { // PH : i = 0
        if (irr == true) {
          // digitalWrite(pH, LOW);
          Serial2.print("D,5" "\r" ); // Red pump message
        }
      }
      if (readings[i].toDouble() > 8.5 && i == 1) { // PH

        //digitalWrite(pH, HIGH);
        Serial3.print("D,5" "\r" ); // Green pump message
      }

      // sensors data send tp the Nextion screen
      Serial.write(0xff);
      Serial.write(0xff);
      Serial.write(0xff);
      Serial.print("t1.txt=\");
      Serial.print(readings[0]); //D.O
      Serial.print("\");

      Serial.write(0xff);
      Serial.write(0xff);
      Serial.write(0xff);
      Serial.print("t2.txt=\");
      Serial.print(readings[1]); //PH
      Serial.print("\");
      Serial.write(0xff);
      Serial.write(0xff);
      Serial.write(0xff);
      //delay (500);
      //}
    }

    next_serial_time = millis() + send_readings_every;
  }
}

// take sensor readings in a "asynchronous" way
void do_sensor_readings() {
  if (request_pending) { // is a request pending?
    if (millis() >= next_reading_time) { // is it time for the reading to be taken?
      receive_reading(); // do the actual I2C communication
    }
  } else { // no request is pending,
    channel = (channel + 1) % TOTAL_CIRCUITS; // switch to the next channel (increase current
    channel by 1, and roll over if we're at the last channel using the % modulo operator)
    request_reading(); // do the actual I2C communication
  }
}

// Request a reading from the current channel

```

```

void request_reading() {
  request_pending = true;
  Wire.beginTransmission(channel_ids[channel]); // call the circuit by its ID number.
  Wire.write('r'); // request a reading by sending 'r'
  Wire.endTransmission(); // end the I2C data transmission.
  next_reading_time = millis() + reading_delay; // calculate the next time to request a reading
}

// Receive data from the I2C bus
void receive_reading() {
  sensor_bytes_received = 0; // reset data counter
  memset(sensordata, 0, sizeof(sensordata)); // clear sensordata array;

  Wire.requestFrom(channel_ids[channel], 48, 1); // call the circuit and request 48 bytes (this
is more then we need).
  code = Wire.read();

  while (Wire.available()) { // are there bytes to receive?
    in_char = Wire.read(); // receive a byte.

    if (in_char == 0) { // if we see that we have been sent a null command.
      Wire.endTransmission(); // end the I2C data transmission.
      break; // exit the while loop, we're done here
    }
    else {
      sensordata[sensor_bytes_received] = in_char; // load this byte into our array.
      sensor_bytes_received++;
    }
  }

  switch (code) { // switch case based on what the response code is.
    case 1: // decimal 1 means the command was successful.
      readings[channel] = sensordata;
      break; // exits the switch case.

    case 2: // decimal 2 means the command has failed.
      readings[channel] = "error: command failed";
      break; // exits the switch case.

    case 254: // decimal 254 means the command has not yet been
finished calculating.
      readings[channel] = "reading not ready";
      break; // exits the switch case.

    case 255: // decimal 255 means there is no further data to send.
      readings[channel] = "error: no data";
      break; // exits the switch case.
  }
  request_pending = false; // set pending to false, so we can continue to the next
sensor
}

// {
// readADC();
// }

float mapfloat(float x, float in_min, float in_max, float out_min, float out_max)
{
  return (x - in_min) * (out_max - out_min) / (in_max - in_min) + out_min;
}

```